Winter 2020

A MULTI-SCALE CRYSTAL PLASTICITY FINITE ELEMENT MODELING FRAMEWORK FOR PREDICTING STRAIN-RATE SENSITIVE DEFORMATION OF HEXAGONAL METALS

William G. Feather
University of New Hampshire, Durham

A MULTI-SCALE CRYSTAL PLASTICITY FINITE ELEMENT MODELING FRAMEWORK FOR PREDICTING STRAIN-RATE SENSITIVE DEFORMATION OF HEXAGONAL METALS

BY

William George Feather

B.S. Mechanical Engineering, Daniel Webster College, 2017

THESIS

Submitted to the University of New Hampshire

in Partial Fulfillment of

the Requirements for the Degree of

Master of Science

in

Mechanical Engineering

December 2020

THESIS COMMITTEE PAGE

This thesis has been examined and approved in partial fulfillment of the requirements for the degree of Master of Science in Mechanical Engineering by:

Marko Knezevic, Associate Professor of Mechanical Engineering

Igor Tsukrov, Professor of Mechanical Engineering

Jinjin Ha, Assistant Professor of Mechanical Engineering

On November 13, 2020

Original approval signatures are on file with the University of New Hampshire Graduate School.

Table of Contents

Dedication

I would like to dedicate this work to my late advisor Professor Timothy Kostar. As well as being a loving father and husband, he was an excellent and inspiring teacher. While Professor Kostar had the reputation of being one of the most difficult professors at Daniel Webster, it was clear he truly cared about the success of his students. His love for teaching shined through his sarcasm and crass comedy, and he would always make time to answer any student's questions regardless of magnitude, even if he pretended to be reluctant about it. He taught many of my favorite classes, and much of my proudest work was for his assignments. Thank you Timmy, without your encouragement, I would not have done as well as I did at Daniel Webster and may not have decided to continue my education and pursue a Master’s Degree.

Acknowledgments

I'd like to thank my advisor, Marko Knezevic, for the opportunity and continued support. The research experience I gained under his guidance will be an invaluable asset to me in my future career.

I'd also like to thank my fellow graduate students, Dan Savage, Milan Alderjan, Tim Barret, Adnan Eghtesad, Miroslav Zecevic and Milovan Zecevic, for their guidance, support and help along the way. Specifically, I'd like to acknowledge Milan's work developing the CPFE code that was used to perform much of the research presented in this thesis, and Dan's help with essentially re-writing and modernizing the CPFE code.

And of course I'd like to thank my family and friends, specifically my mother Jackie, my girlfriend Carolyn and my friend and mentor Professor Chris Carlstrom, for their support.

Abstract

This work presents improvements to the methods used in crystal plasticity simulations. It shows how these improvements can be used to accurately predict the deformation behavior of two magnesium alloys, WE43, and AZ31. The first improvement to the methodology is guidance on the type of finite elements to use in explicit grain crystal plasticity simulations. This study found that quadratic tetrahedral and linear hexahedral elements are the most accurate element types included in the study. The study also concluded that tetrahedral elements are more desirable due to fast mesh generation and flexibility to describe geometries of grain structures. The second improvement made was the addition of a numerical scheme to enable the use of any rate sensitivity exponent in the fundamental power-law representation of the flow rule in crystal visco-plasticity. While allowing the use of even very large exponents that many materials exhibit, this numerical scheme adds little to no increase in computational time. This crystal plasticity model was used to accurately predict the deformation behavior of both WE43 and AZ31 under quasi-static and high rate deformation, predicting the stress-stain response and the evolution of texture, twinning and the relative activities of the various deformation modes.

Introduction

The work in this thesis revolves around a recently developed multi-level constitutive model for polycrystalline metals that deform by a combination of elasticity, crystallographic slip, and deformation twinning. The model utilizes a two-level homogenization scheme, first, within the integration points of the finite elements, a Tylor-type model is used to homogenize the response of the virtual polycrystal. This Taylor type model uses an iso-strain method across the polycrystal resulting in a stress imbalance between the crystals. The second homogenization level, an implicit finite element method, relaxes this stress imbalance and relates the response of the polycrystals to the macro-level response of the finite elements.

The first Chapter presents a mesh type and density study for explicit grain crystal plasticity finite element simulations. In this study four element types, four mesh densities and two load cases were used to investigate their effects on accuracy of predicted mechanical fields over explicit grain structures. A voxlized grain structure was created by a phase field simulation and was smoothed using an overly grid method and was re-meshed with both tetrahedral and hexahedral elements. This study found that quadratic tetrahedral and linear hexahedral elements are more accurate than linear tetrahedral and quadratic hexahedral elements for these explicit grain CPFE simulations.

The second chapter of this thesis presents an investigation into the mechanical response of the magnesium alloy, WE43, as a function of strain rate. The model was calibrated to accurately predict the mechanical response and twin and texture evolution. The calibration was informed using experimentally obtained results of WE43 under simple compression and tension at a quasi-static strain rate and in compression at high rates and room temperature. The results of this study

were the accurate prediction of rate sensitivity effects of WE43. These rate effects were attributed to the activation contraction and double twins during high rate deformation.

In the third and final chapter the power-law relation that is at the core of the CPFE model is improved with a numerical method to facilitate the uses of true material rate sensitivity exponents. Traditional implementations of the power law relation are bound to use low values for rate sensitivity exponents due to computational limits. These artificially low exponents induce inaccuracies in the form a high strain-rate sensitivity in crystal plasticity simulations. To showcase the improvement the improved code was used to accurately predict the complex strain-rate sensitive response and microstructural evolution of AZ31 Mg alloy using measured values for the rate sensitivity exponents.

Chapter 1: A numerical study into element type and mesh resolution for crystal plasticity finite element modeling of explicit grain structures

This chapter is published as: Feather, William G., Hojun Lim, and Marko Knezevic. "A numerical study into element type and mesh resolution for crystal plasticity finite element modeling of explicit grain structures." *Computational Mechanics* (2020): 1-23.

My contribution to this work was to develop a full set of finite element meshes of an explicit grain structure using several different element types and mesh densities. Using this explicit grain mesh, I set up and ran 32 simulations totaling four months of simulation time. Upon completion, I created scripts to automate the post-processing and figure creation of the 32 simulations. From these results, I assisted Professor Knezevic in drawing conclusions on the pros and cons of different element types for these explicit grain CPFE simulations. The text was written in a standard student-mentor relationship.

A numerical study into element type and mesh resolution for crystal plasticity finite element modeling of explicit grain structures

William G. Feather [a], Hojun Lim [b], Marko Knezevic [a,1]

[a] Department of Mechanical Engineering, University of New Hampshire, Durham, NH 03824, USA.

[b] Department of Computational Materials & Data Science, Sandia National Laboratories, Albuquerque, NM, 87185, USA.

Abstract

A large number of massive crystal-plasticity-finite-element (CPFE) simulations are performed and post-processed to reveal the effects of element type and mesh resolution on accuracy of predicted mechanical fields over explicit grain structures. A CPFE model coupled with Abaqus/Standard is used to simulate simple-tension and simple-shear deformations to facilitate such quantitative mesh sensitivity studies. A grid-based polycrystalline grain structure is created synthetically by a phase-field simulation and converted to interface-conformal hexahedral and tetrahedral meshes of variable resolution. Procedures for such interface-conformal mesh generation over complex shapes are developed. FE meshes consisting of either hexahedral or tetrahedral, fully integrated as linear or quadratic elements are used for the CPFE simulations. It

[1] Corresponding author at:
marko.knezevic@unh.edu (M. Knezevic).

is shown that quadratic tetrahedral and linear hexahedral elements are more accurate for CPFE modeling than linear tetrahedral and quadratic hexahedral elements. Furthermore, tetrahedral elements are more desirable due to fast mesh generation and flexibility to describe geometries of grain structures.

Keywords: Solids; Finite element methods; Plasticity; Micromechanics; Mesh sensitivity

1. Introduction

Modeling of polycrystalline metals often employs spatio-temporal domains of constituent grains interacting explicitly with each other, while achieving the state of stress equilibrium and strain compatibility [1-4]. Such modeling is referred to as full-field. The full-field microstructural modeling, especially in three-dimensions (3D), accounts for topological effects of microstructural evolution on micromechanical fields defined in term of stress and strain and facilitates better understanding of complex phenomena pertaining to material behavior. The stress equilibrium governing equations of mechanics in conjunction with a constitutive law describing the material behavior under deformation can be solved numerically using the finite element method (FEM) in terms of a work-conjugated stress-strain measures [2]. For the FEM, the microstructural domain must be discretized into finite elements. If a crystal plasticity-based constitutive law is embedded at every FE integration point, the mechanical fields are governed by crystallography including deformation mechanisms and crystal lattice orientation as well as the evolution of inter- and intra-granular misorientation, grain shape, and grain-boundary-character-distribution (GBCD).

Beginning from the research reported in [5], the crystal plasticity FE (CPFE) models have been extensively used to predict mechanical fields, typically with a sub-grain mesh resolution [6-11]. In early CPFE modeling, the morphology of grains has not been considered [12-18]. Subsequent studies have considered simplified geometries representing grains such as rhombic dodecahedrons, cuboids, and truncated octahedrons [19-21]. As these geometries were gross approximations of real grain structures and unable to represent grain boundaries, the intra-granular and inter-granular fields were also gross approximations [22]. Recent developments in the field have facilitated accurate representation of individual grains to elucidate the role of grain

structure in determining heterogeneous deformation [9, 10, 23-30]. Such heterogeneous deformation as a function of microstructural evolution and inherent anisotropy even under uniform macroscopic deformation conditions can be predicted by CPFE models. The plasticity modeling at grain scale is essential for understanding and attempting to predict mechanical extremes such as void nucleation driven by local strain concentrations. While full-field models can be used to obtain homogenized material response, more often mean-field models are used for such purpose. However, the mean field models do not account for explicit grain-to-grain interactions [31-44].

An essential building block pertaining to the CPFE modeling of explicit grain structure is generation of polycrystalline domain. To this end, voxel-based microstructures are converted into finite element meshes. One methodology to generate a synthetic voxel-based microstructure is the Voronoi tessellation [24, 25, 45-48]. A software, DREAM.3D (the digital microstructure analysis environment in 3D) has been developed by U.S. Air Force Research Laboratory and Blue Quartz as a more sophisticated tool to generate voxel-based microstructures [49]. Grain size and shape statistics, orientation and misorientation distributions can be used as inputs to generate voxel-based models of microstructure. A convenient output of the software for subsequent mesh generation is surface mesh over individual grains. Synthetic microstructures represented by voxels can further be obtained by microstructural evolution models such as phase-field grain growth [50], Potts (Monte-Carlo) grain growth [51, 52], and cellular automata [53, 54]. In addition to synthetic generation of voxel-based microstructures, several experimental techniques have been advanced/developed to acquire real 3D grain structure data. These techniques include, robotic serial sectioning complemented with electron backscattering diffraction (EBSD) [55, 56], focused ion beam (FIB) EBSD serial sectioning [57-62], and non-destructive near field high

energy X-ray diffraction microscopy (nf HEDM) [63-67]. DREAM.3D offers various features to post-process such experimental data producing triangular surface mesh for grains for subsequent volume mesh generation.

In polycrystalline CPFE simulations, microstructural data is converted into a finite element mesh. A voxel grid-based description of the microstructure requires a significant number of voxels to capture the complex geometry of the grains accurately. If every voxel is converted to a hexahedral (brick) finite element [68], the mesh may contain a very large number of finite elements, increasing the computational cost of such simulations beyond practical levels. In addition, it is shown that voxelated meshes could develop artificial stress/strain localizations at interfaces or triple junctions due to stair-case instead of smooth/flat grain boundaries present in such meshes [28, 69]. In summary, while a microstructure obtained directly from experimental images in voxel format may be the easiest way to initialize simulations with hexahedral elements, large number of voxels equivalent to the number of hexahedral elements may make such simulations computationally inefficient and the intrinsic stair-stepped grain boundaries may make the simulations inaccurate.

In recent works [70, 71], we have developed procedures relying on the surface mesh of individual grain to create tetrahedral volume mesh, which is conformal between grains. The conformal mesh implies that neighboring grains share nodes at grain boundaries. Several subsequent works have utilized the developed tools to study shear band formation [72] and explicit twins [8, 73]. These procedures have also been advanced to create polycrystalline meshes for various specimen geometries other than cubes suitable for microforming [74, 75] and micromechanical testing [46] simulations. Also, mesh generation software package Cubit,

developed at Sandia National Laboratories [76], can generate 3D interface conformal meshes using not only tetrahedral but also hexahedral elements.

In this work, we investigate effects of element types and mesh resolution for CPFE modeling of explicit grain structures. The study complements the recent work of mesh sensitivity of single crystal with grains represented by simple cubic shapes and polycrystalline representative volume elements while varying factors such as initial textures, hardening models and boundary conditions [27]. In addition to accounting for the effect from complex grain features in realistic microstructures, the present study considers four element types including linear tetrahedral (*tet*), quadratic tet, linear hexahedral (*hex or brick*), and quadratic hex of various resolutions in predicting the mechanical fields. A large number of massive CPFE simulations are performed and post-processed to reveal the effects of element type and mesh resolution on accuracy of predicted mechanical fields. An initial voxel-based polycrystalline grain structure (microstructural cell) is created synthetically by a phase field grain growth simulation and converted to interface-conformal hex and tet meshes at various levels of discretization. Considering that boundary conditions may affect the mesh sensitivity in addition to grain structure, two types of boundary conditions involving simple tension (ST) and simple shear (SS) are imposed over the microstructural domain for the given number of elements i.e. their degrees-of-freedom. Since these simulations require significant memory size and computational time, a parallel computing infrastructure is utilized. Comparisons of CPFE results in terms accuracy and computational efficiency are presented and discussed in the paper. It is anticipated that the main conclusion from this study will serve as useful guidance in polycrystalline CPFE modeling.

2. Modeling framework

2.1 Summary of CPFE and a hardening model

A standard single crystal elasto-visco-plastic constitutive law is used to relate a pair of work conjugated stress and strain measures at each integration point, in every finite element [13]. This formulation is briefly summarized below. The total deformation gradient tensor, $\mathbf{F}$, at every integration point obtained from the finite element solver is multiplicatively decomposed into an elastic stretching and lattice rotation part, $\mathbf{F}^*$, and the plastic part, $\mathbf{F}^p$, embedding the plastic deformation carried out by crystallographic slip

$$\mathbf{F} = \mathbf{F}^*\mathbf{F}^p. \tag{1}$$

The stress-strain relations are

$$\mathbf{T}^* = \mathbf{C}\mathbf{E}^*, \quad \mathbf{T}^* = \mathbf{F}^{*-1}\{(\det\mathbf{F}^*)\boldsymbol{\sigma}\}\mathbf{F}^{*-T}, \mathbf{E}^* = \frac{1}{2}\{\mathbf{F}^{*T}\mathbf{F}^* - \mathbf{I}\}, \tag{2}$$

where $\mathbf{C}$ is the elastic stiffness tensor, $\mathbf{T}^*$ is the second Piola–Kirchhoff stress, $\mathbf{E}^*$ is the Green-Lagrangian strain tensors, and $\boldsymbol{\sigma}$ is the Cauchy stress. The flow rule for $\mathbf{F}^p$ is

$$\dot{\mathbf{F}}^p = \mathbf{L}^p\mathbf{F}^p, \mathbf{L}^p = \sum_\alpha \dot{\gamma^\alpha}\mathbf{b}_o^\alpha \otimes \mathbf{n}_o^\alpha, \tag{3}$$

where $\dot{\gamma^\alpha}$ is the shearing rate per slip system α, while $\mathbf{b}_o^\alpha$, and $\mathbf{n}_o^\alpha$ denote the slip system geometry i.e. the slip direction and the plane normal, respectively, in the total Lagrangian manner denoted by the subscript 'o'. The power-law relation is used for the shearing rate [77-79].

$$\dot{\gamma}^\alpha = \dot{\gamma}_0^\alpha \left(\frac{|\tau^\alpha|}{\tau_c^\alpha}\right)^{1/m} \mathrm{sign}(\tau^\alpha), \tag{4}$$

where, τ^α is on the driving force ($\tau^\alpha = \mathbf{T}^* \cdot \mathbf{b}_o^\alpha \otimes \mathbf{n}_o^\alpha$) on the slip system α, τ_c^α is the resistance to slip, $\dot{\gamma}_0^\alpha$ is a reference slip rate of 0.001 s^{-1}, and m is the strain rate sensitivity constant of 0.01. To complete the theory, the crystal lattice spin, $\mathbf{W}^*$, is

$$\mathbf{W}^{*} = \mathbf{W}^{app} - \mathbf{W}^{p}, \mathbf{W}^{p} = \frac{1}{2}(\mathbf{L}^{p} - \mathbf{L}^{pT}), \quad (5)$$

where $\mathbf{W}^{app}$ is the applied spin over the polycrystal and $\mathbf{W}^{p}$ is the plastic spin. The numerical implementation of the above theory is described in detail in [13].

The constitutive model summarized above has been coupled with a hardening model for the evolution of slip resistance. The model has been presented and applied to polycrystalline Cu in [7]. The model considers statistically stored dislocations (SSDs) governing the threshold stresses for the activation of each slip system. The densities of dislocations evolve based on a thermally activated rate law with shearing on slip systems [80]. The slip resistance, τ_c^{α} , for all $\{111\}\langle 110\rangle$ slip systems α, is the isotropic over all slip systems, i.e., $\tau_c^{\alpha} = \tau_c \, , \forall \alpha$. However, it varies from grain to grain. The τ_c is the sum of three contributions as follows [81-85]

$$\tau_c = \tau_0 + \tau_{for} + \tau_{sub}, \quad (6)$$

with τ_0 being a friction stress that embeds the Peierls stress, barrier effect due to grain size, and any content of initial dislocation density. This term does not evolve with plastic strain but decays exponentially with temperature as is the case for many metals [38, 86].

$$\tau_0 = A\exp\left(-\frac{T-298}{B}\right). \quad (7)$$

Here, *A* and *B* are fitting constants and *T* is the temperature in K. The remaining two contributions to slip resistance are the forest and substructure/debris interaction stresses, τ_{for} and τ_{sub}, respectively. These two terms evolve with dislocation densities, i.e. the forest and substructure dislocation densities ρ_{for} and ρ_{sub} according to the Taylor-type relations [87-89].

$$\tau_{for} = \chi b\mu\sqrt{\rho_{for}}, \quad (8)$$

$$\tau_{sub} = 0.086\mu b\sqrt{\rho_{sub}}\log\left(\frac{1}{b\sqrt{\rho_{sub}}}\right), \quad (9)$$

where b is the Burgers vector (2.5563×10^{-10} m for Cu), μ is the shear modulus ($4.8\text{x}10^{4}$ MPa for Cu) and χ is a dislocation interaction factor [90] that varies with temperature as follows.

$$\chi = \chi_0 - K_1\ln\left(\frac{T}{K_2}\right). \quad (10)$$

At room temperature, $\chi(T = 298\text{K})$ is 0.9541. The initial density of statistically stored forest dislocation density is set to 10^{12} m^{-2}, which is an annealed state of the material and ρ_{for} is determined by the balance between the rate of generation and the rate of removal i.e. dynamic recovery [87, 91, 92],

$$\frac{\partial\rho_{for}}{\partial\gamma} = \frac{\partial\rho_{gen,for}}{\partial\gamma} - \frac{\partial\rho_{rem,for}}{\partial\gamma} = k_1\sqrt{\rho_{for}} - k_2(\dot{\varepsilon},T)\rho_{for},\ \Delta\rho_{for} = \frac{\partial\rho_{for}}{\partial\gamma}\sum_\alpha|\Delta\gamma^\alpha|, \quad (11)$$

with k_1^s as a coefficient for statistical trapping and k_2^s as a rate-sensitive coefficient defined by

$$\frac{k_2}{k_1} = \frac{\chi b}{g}\left(1 - \frac{kT}{Db^3}\ln\left(\frac{\dot{\varepsilon}}{\dot{\varepsilon}_o}\right)\right). \quad (12)$$

In Eq. (12), k, $\dot{\varepsilon}_o$, g^α, and D^α are a Boltzmann constant, a reference strain-rate of 10^7 s^{-1}, an activation enthalpy, and a drag stress, respectively. The last two are fitting constants.

The rate of debris density of dislocations evolves using

$$\Delta\rho_{sub} = qb\sqrt{\rho_{sub}}k_2\rho_{for}\sum_\alpha|\Delta\gamma^\alpha|, \quad (13)$$

with q as a rate coefficient defined by

$$q = q_0\ln\left(1 + \frac{T}{q_1}\right). \quad (14)$$

The factor q determines a fraction of dislocations that leads to debris formation, while the rest is annihilated. Eq. (13) is based on thermally activated processes, such as cross slip and climb, which are responsible for pattern formation [93-96]. In the model, a smaller fraction of the recovered forest dislocations contributes to debris formation.

The hardening law parameters for polycrystalline Cu have been presented in [7]. The parameters have been calibrated and validated to mechanical tests on Cu over a range of strain-rates and temperatures. However, only quasi-static deformation at room temperature is considered in the present work.

2.2 Mesh generation procedures

To generate an interface conformal hexahedral mesh of polycrystals, the Sculpt meshing tool [97, 98], a companion application to the Cubit Meshing and Geometry Toolkit developed at Sandia National Laboratories [76] is used. A phase field data of microstructure is used to define volume fractions of grains and locate the center of the grain interfaces (grain boundaries) at every grid. Cartesian grid nodes near the interfaces are moved to approximated grain interfaces from volume fractions and one or more hexahedra are inserted on both sides of the grain interfaces. A smoothing step is then performed to improve both smoothness of the interface planes and the quality of the hexahedra. More detailed description of interface conformal meshing procedures can be found in [28, 97].

The initial voxelated microstructure generated by a phase-field grain growth simulation is shown in Fig. 1a. The grain growth simulation was performed on a uniform grid of 96 x 96 x 96 until approximately 50 grains were achieved. The simulation relied on a coarse-grained free energy functional of a polycrystalline system, which is solved for structural order parameters that

describe individual grains. The spatio-temporal evolution of the order parameter was based on Allen-Cahn equation [99]. More detailed description of the model can be found in [28, 100, 101]. The snapshot of the microstructure is chosen to resolve interfaces/triple junctions of grains. Edge length of the cube is a unity. The voxels that make up the phase-field model create stair-stepped grain boundaries. If such hexahedral meshes with the stair-case grain boundaries are used in CPFE simulations, mechanical fields at the grain boundary regions are over predicted. Such differences in the local plasticity values between the stair-case and the smooth/flat grain boundaries have been studied in [69]. The work revealed that the grain boundaries represented by the stair-case morphology are sources for extreme plasticity and should be replaced with locally smooth/flat morphology.

This voxel-based geometry was meshed with Cubit/Sculpt to create six initial hexahedral meshes of various mesh densities. The stair-stepped grain boundaries are smoothed by meshing (Fig. 2a). Considering both linear and quadratic element types/formulations, a total of eight meshes were created for simulations as shown in Fig. 2b. Table 1 lists the total number of elements per finite element mesh from Fig. 2b, while Table 2 and 3 shows the average number of integration points per grain and the average element edge length representing averaged element size per mesh. After selecting the microstructural cell consisting of a sufficient number of grains governing heterogeneous deformation in ST and SS, the grades of meshes are selected for the numerical study. These are defined based on the number of integration points and termed as fine, medium, coarse and extra-coarse. The medium grade meshes had element size similar to models used in several of our prior successful studies in which mesh sensitivity studies were performed [70, 102, 103]. The simulations were performed first with these medium grade meshes. Subsequently, coarse and fine mesh grades were created by reducing and increasing the number of integration

points by a factor of approximately two. The fine grade meshes intended to further improve the accuracy of the simulations approached the limit of our computational resources, particularly in terms of the memory requirements. Four computer workstations of Intel(R) Xeon(R) Gold 6130 CPU @ 2.10GHz with 32 physical cores and 772 GB RAM per node were recently acquired specifically for CPFE modeling and used in the present study. After performing the simulations using fine and coarse meshes, we observed that the mesh refinement slightly improved accuracy for <1%, while the mesh coarsening decreased accuracy for <5%. To decrease the accuracy more appreciably, the extra-coarse mesh grade was introduced by substantially reducing the number of integration points.

Pole figures showing the distribution of crystal orientations assigned to the model are shown in Fig. 1b, while appendix A lists Bunge-Euler angles and corresponding weights. There are 52 grains treated as separate element sets and each grain is randomly assigned with initially identical crystal orientation. Note that a representative volume element must have sufficient number of constituent grains to homogenize the variability arising from local microstructural features such as micro-texture, defects and phases. However, the 52 grains model used in this work is not intended to be a representative volume element but a microstructural cell facilitating the numerical study of local fields.

To create the tetrahedral meshes, a procedure described in [70] and later refined in [71] is followed. First, the surface meshes of the grains were extracted as STLs from the initial hexahedral meshes. As STLs are inherently triangular, Abaqus splits each rectangular element of the surface mesh on its diagonal to make the triangles. These STLs were then meshed in MSC Patran [104] with the internal element size coarsening enabled. Internal coarsening increases the size of the elements inside the grains, reducing the total number of elements. The total of six

tetrahedral meshes with different resolutions were selected for either linear or quadratic element types. These meshes are also shown in Fig. 2b. The corresponding element counts for each mesh are shown in Table 1 along with the average number of integration points per grain and average element edge per mesh in tables 2 and 3, respectively.

The meshes are categorized by an approximate number of IPs for each mesh density (Fine, Medium, Coarse, and Extra-Coarse). Diagonal of table 1 (italic, bold numbers) has mesh density of approximately 200,000. Furthermore, two instances of linear and quadratic elements whether hex or tet in table 1 have the same number of elements (italic numbers). In summary, the selected meshes of variable resolution and four element types can facilitates a variety of comparisons, which will be presented in subsequent sections of the paper. In particular, local and global mechanical fields upon deformation are compared as functions of element type and resolution of meshes i.e. degrees of freedom. Moreover, the fields are compared for a given number of integration points or a given number of elements. Finally, the simulations are compared in terms of computational time.

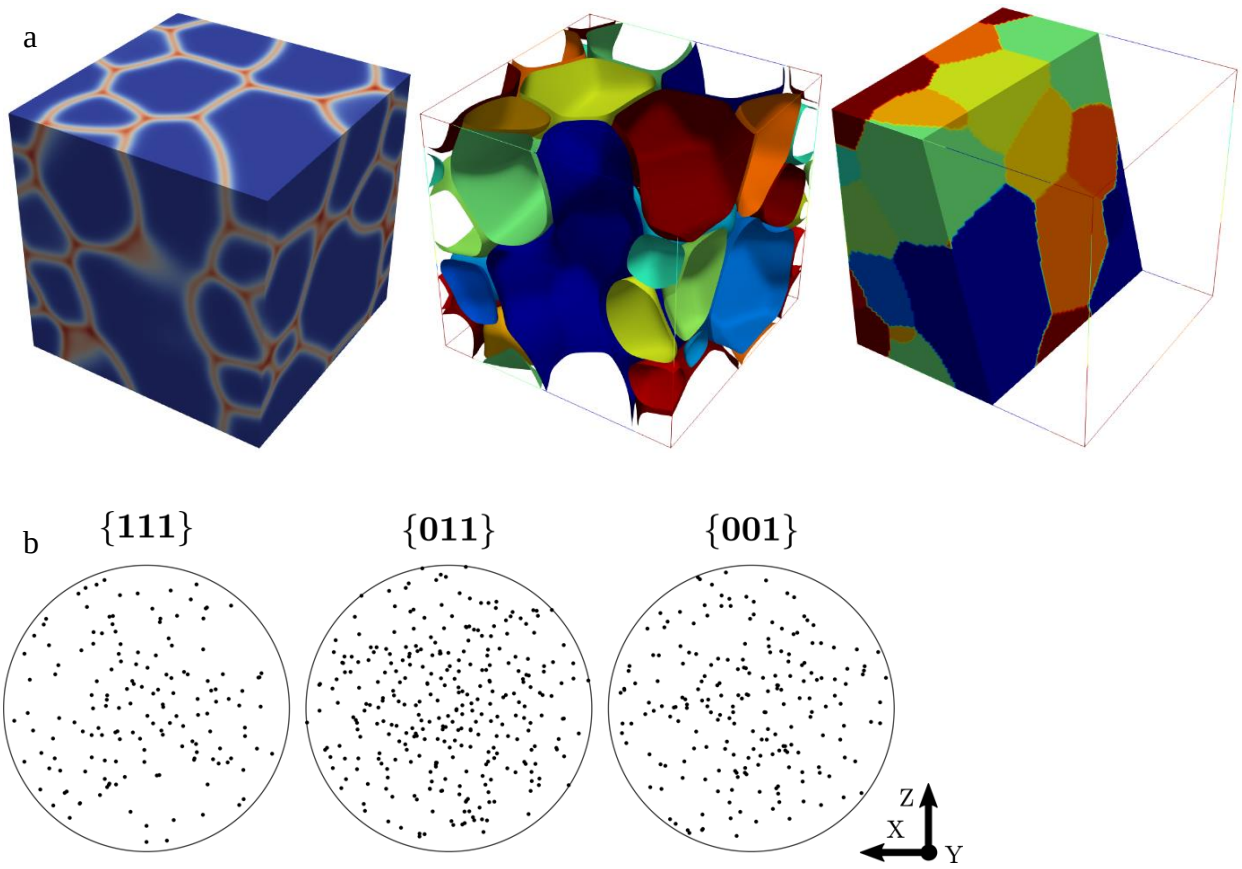

Figure 1. (a) A microstructure produced using a phase field grain growth code. The original phase field data is shown on the left with red regions (grain boundary regions) representing locations where multiple phase fields exist. The middle image shows grain boundaries. The image on the right is a section through the microstructure showing the internal structure. (b) Pole figures showing the distribution of crystal orientations, which will be assigned to the model in (a).

a

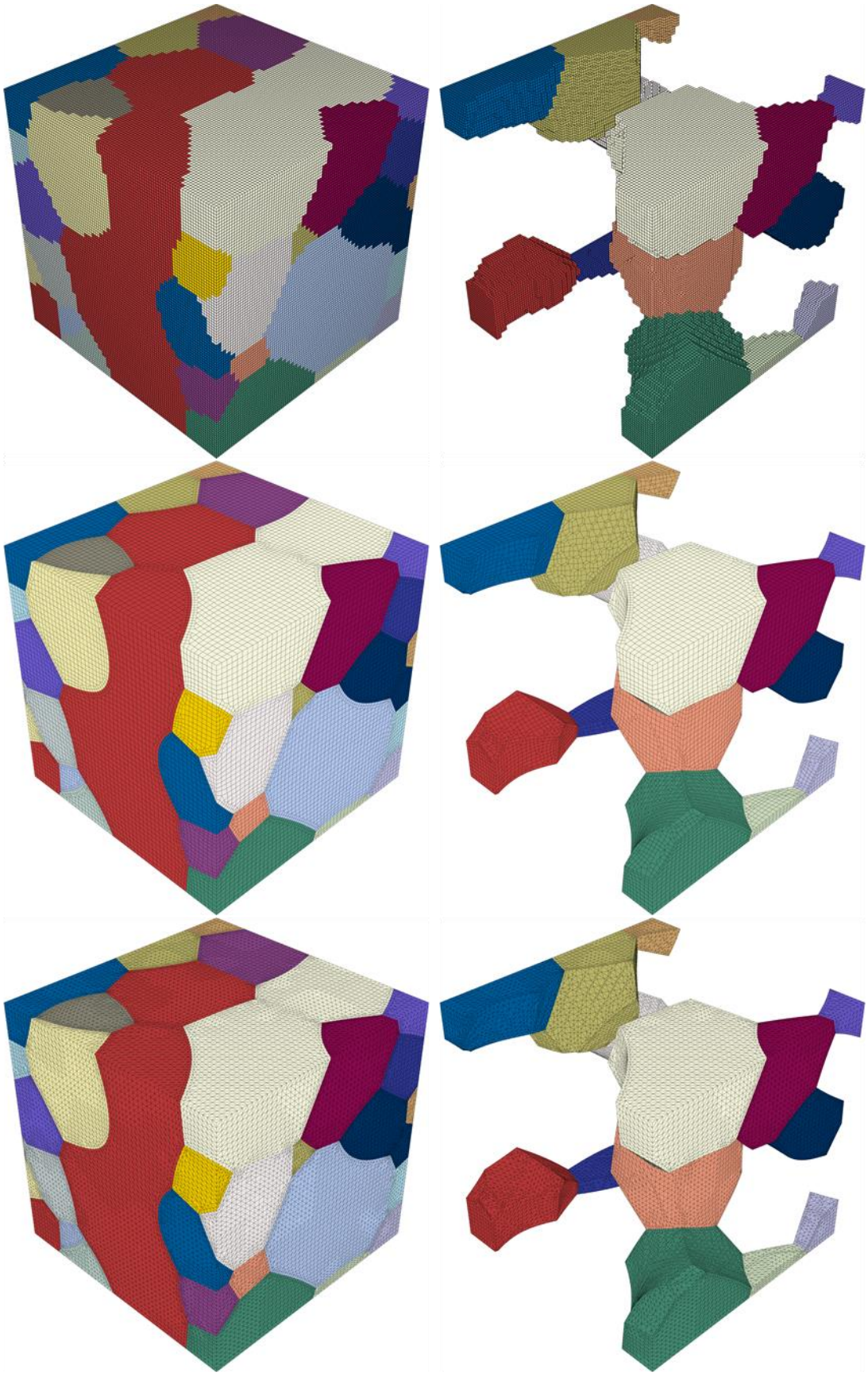

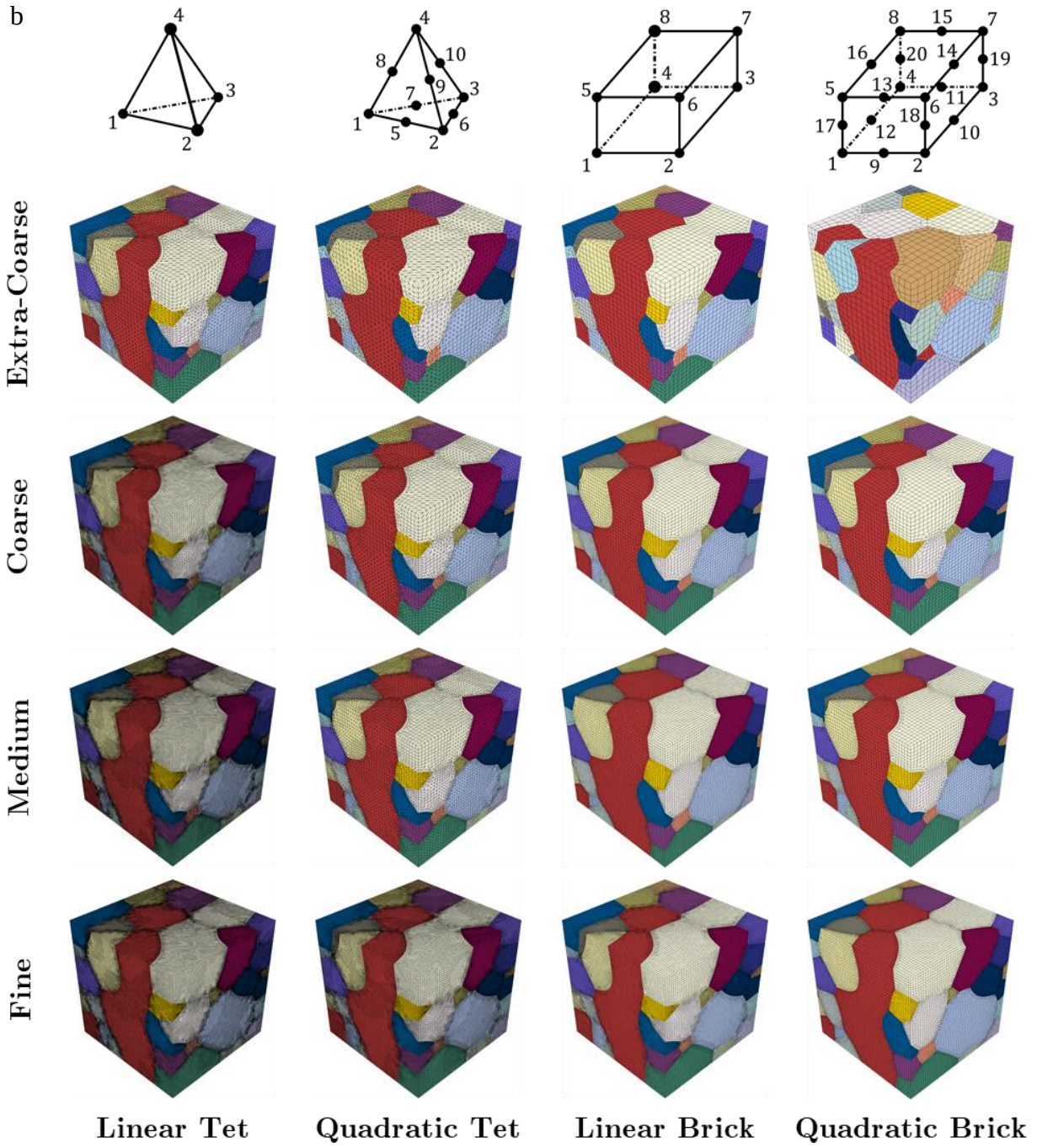

Figure 2. (a) Polycrystalline microstructure consisting of 52 grains discretized into voxels, hexahedral elements, and tetrahedral elements. The images on the right show internal boundaries revealing the stair-stepped morphology of the grain boundary voxels in the voxel-based microstructure, which are smoothed to squares (hexahedral elements) and triangles (tetrahedral elements) representing grain boundary planes/curvatures shared between volume elements of neighboring grains. (b) Finite element meshes of variable resolution for the explicit grain structure from (a) along with C3D4, C3D10, C3D8, and C3D20 element schematics. The edge length of the cubes is taken as a unity. The total number of elements is given in Table 1.

Table 1. Number of elements per finite element mesh from Fig. 2 categorized by an approximate number of integration points (IPs) for each mesh density (Fine, Medium, Coarse, and Extra-Coarse). The number of IPs per element type C3D4, C3D10, C3D8, and C3D20 is 1, 4, 8, and 27, respectively.

Mesh	Linear Tet (C3D4)	Quadratic Tet (C3D10)	Linear Hex (C3D8)	Quadratic Hex (C3D20)
Fine ~ 4,300,000 IPs	4,477,664	964,865	480,464	215,714
Medium ~ 2,140,000 IPs	2,651,248	559,708	215,714	107,356
Coarse ~ 900,000 IPs	964,865	206,049	107,356	60,058
Ex-Coarse ~ 200,000 IPs	206,049	57,142	24,856	10,193

Table 2. Average number of integration points (IPs) per grain in the explicit grain structure models.

Mesh	Linear Tet	Quadratic Tet	Linear Hex	Quadratic Hex
Fine ~ 4,300,000 IPs	86,109	74,220	73,918	112,005
Medium ~ 2,140,000 IPs	50,986	43,054	33,187	55,743
Coarse ~ 900,000 IPs	18,555	15,850	16,516	31,184
Ex-Coarse ~ 200,000 IPs	3,962	4,396	3,824	5,293

Table 3. Average element edge length per mesh. Abaqus provides this distance as in between elemental nodes. Considering that the quadratic elements have a node in the middle of every edge, their average edge length is split in half.

Mesh	Linear Tet	Quadratic Tet	Linear Hex	Quadratic Hex
Fine	0.013413	0.009182	0.012629	0.008264
Medium	0.014774	0.012966	0.016528	0.010431
Coarse	0.018365	0.016961	0.020863	0.023644
Ex-Coarse	0.033921	0.026474	0.034753	0.032699

2.3 Boundary conditions

A simple tension boundary conditions were defined by prescribing a displacement on the top surface in the normal direction (positive Y), while ensuring the lateral surfaces to be stress-free. The simple shear case was defined similar to the simple tension case, but the prescribed displacement was along the Y-direction on the positive Z face, and the negative Z face was

constrained in the Y direction.. Prescribed displacement was $U = 0.22$ for both tension and shear at approximate strain rate of 0.001 /s and at room temperature. (Note that the polycrystalline domain has a size of 1). In all simulations, direct sparse solver in Abaqus was used and the initial time step was 0.0001 s, the maximum and the minimum time steps of 4 s and 0.00002 s were assigned, respectively.

3. Simulation results

A CPFE model coupled with the implicit finite element software Abaqus/Standard is used to solve the boundary value problem corresponding to simple tension (ST) and simple shear (SS) of the microstructural cell. A total of 32 simulations have been performed and post-processed for this paper. The simulations performed were demanding in both RAM size requirement as well as computational time. Computational time required to complete the jobs is presented in table 4, given the number of elements and their degrees-of-freedom and the boundary conditions. As is indicated in the table, the MPI parallel computing infrastructure available in Abaqus was utilized. Given the CPFE model storing variables pertaining to the crystallography such as crystal orientations, Schmid tensors etc. in addition to stress-strain measures and underlying state variables pertaining to the hardening law such as slip resistance and dislocation densities, table 5 shows the memory requirement per simulation. Note that the memory usage is a function of the number of used CPUs per simulation (table 4).

Figs. 3 and 4 show von Mises stress, while appendix B presents equivalent strain and pressure contours after ST and SS to a displacement of $U = 0.22$. Minor sensitivity of models to the boundary conditions ST vs SS can be observed. Qualitative comparison reveals that the models predict strong/hot versus weak/cold spots in the microstructure independent on the level of

discretization. Nevertheless, the predicted contours are different for most of the models with the extra-coarse models exhibiting the obvious deviations.

Further consideration of the fields as a function of element type shows that the discontinuities in the fields and the largest heterogeneities are present in the quadratic hexahedral extra-coarse model. Large deviations are also present across the linear tet models. Interestingly the largest range of values in pressure as well as heterogeneity in pressure fields exhibits the extra coarse quadratic hexahedra mesh. The fields become smoother with mesh resolution but still hot/cold spots are present. Linear tetrahedral element also exhibits a large range of values in pressure. Fields predicted by quadratic tetrahedral and linear hexahedral appear to be similar, especially for medium and fine mesh resolutions.

To further investigate internal fields, Fig. 5 shows contours over the surface for a central grain. Figure 6 compares models quantitatively, in terms of stress versus strain components for the central grain using stress-strain curves and a suitably defined error measure at the middle and at the end of deformation for both ST and SS. While the overall trends in the stress-strain curves are similar, the linear tet elements deviate from the predictions using the other element types. The error is defined as

$$\%Error(mesh_i) = \frac{|\int_V \sigma_{ij}(mesh_i) - \int_V \sigma_{ij}(QTet_{964865})|}{\int_V \sigma_{ij}(QTet_{964865})}, \quad (15)$$

where, V is the volume of central grain, while $\sigma_{ij} = \sigma_{22}$ is for ST and $\sigma_{ij} = \sigma_{23}$ is for SS. The error is relative to the fine Qtet-964,865 model (Fig. 2b). As is evident, the quantitative comparisons reveal that linear tet elements introduce a large error in CPFE calculations, even with substantially increased mesh resolution. Interestingly the linear brick elements develop the smallest rate of deviation in the fields with mesh coarsening amongst the studied element types.

In contrast, the quadratic brick elements develop the greatest amount of deviation with mesh coarsening. The use of extra-coarse meshes leads to inaccuracy, as expected independent on the element type. While the figure quantifies errors as a function of the simulation method for the central grain only, similar trends are predicted for any other individual grain or a group of grains or the overall model. Importantly, predictions of grain averaged stresses as calculated here can be validated using high energy synchrotron x-rays. The methodology is being used to measure such grain averaged quantities.

Table 4a. Nodes x CPUs per node/total CPUs/total CPU time [h]/time per CPU [h] for the simple tension simulations. Simulations were carried out on a workstation or multiple workstations: Intel(R) Xeon(R) Gold 6130 CPU @ 2.10GHz with 32 physical cores and 772 GB RAM per node using various numbers of CPUs.

Mesh	Linear Tet	Quadratic Tet	Linear Hex	Quadratic Hex
Fine ~ 4,300,000	1x30/30/101.5/	3x30/90/129.2/	1x16/16/73.9/	3x24/72/239.7/3
Medium ~	1x16/16/32/2	1x30/30/119.8/	1x30/30/17.6/	1x30/30/76.1/2.
Coarse ~ 900,000	1x16/16/5.8/0.	1x30/30/12/0.4	1x30/30/4.5/0.	1x16/16/29.8/1.
Ex-Coarse ~	1x16/16/0.8/0.	1x30/30/2.0/0.	1x30/30/0.7/0.	1x30/30/1.4/0.0

Table 4a. Nodes x CPUs per node/total CPUs/total CPU time [h]/time per CPU [h] for the simple shear simulations. Simulations were carried out on a workstation or multiple workstations: Intel(R) Xeon(R) Gold 6130 CPU @ 2.10GHz with 32 physical cores and 772 GB RAM per node using various numbers of CPUs.

Mesh	Linear Tet	Quadratic Tet	Linear Hex	Quadratic Hex
Fine ~ 4,300,000 IPs	2x30/60/57.3/1.	2x16/32/78.6/2.	1x30/30/50.0/	2x16/32/256.6/4
Medium ~ 2,140,000	1x30/30/16.7/0.	1x30/30/109.0/	1x30/30/15.2/	2x30/60/58.7/0.
Coarse ~ 900,000 IPs	1x30/30/3.6/0.1	1x30/30/11.2/0.	1x30/30/3.8/0	1x30/30/22.0/0.
Ex-Coarse ~ 200,000	1x30/30/0.7/0.0	1x30/30/2.9/0.1	1x30/30/0.7/0	1x30/30/1.4/0.0

Table 5a. Approximate memory usage in GB per simple tension simulation.

Mesh	Linear Tet	Quadratic Tet	Linear Hex	Quadratic Hex
Fine ~ 4,300,000	552.9	2,508.9	266.2	1,684.9
Medium ~	185.3	613.7	212.4	385.6
Coarse ~ 900,000	93.4	221.3	173.8	133.4

Ex-Coarse ~	32.2	185.8	61.2	185.3

Table 5b. Approximate memory usage in GB per simple shear simulation.

Mesh	Linear Tet	Quadratic Tet	Linear Hex	Quadratic Hex
Fine ~ 4,300,000	993.6	968.9	432.2	870.1
Medium ~	305.4	613.7	212.4	687.4
Coarse ~ 900,000	175.1	221.4	173.7	216.4
Ex-Coarse ~	173.7	185.3	61.2	185.3

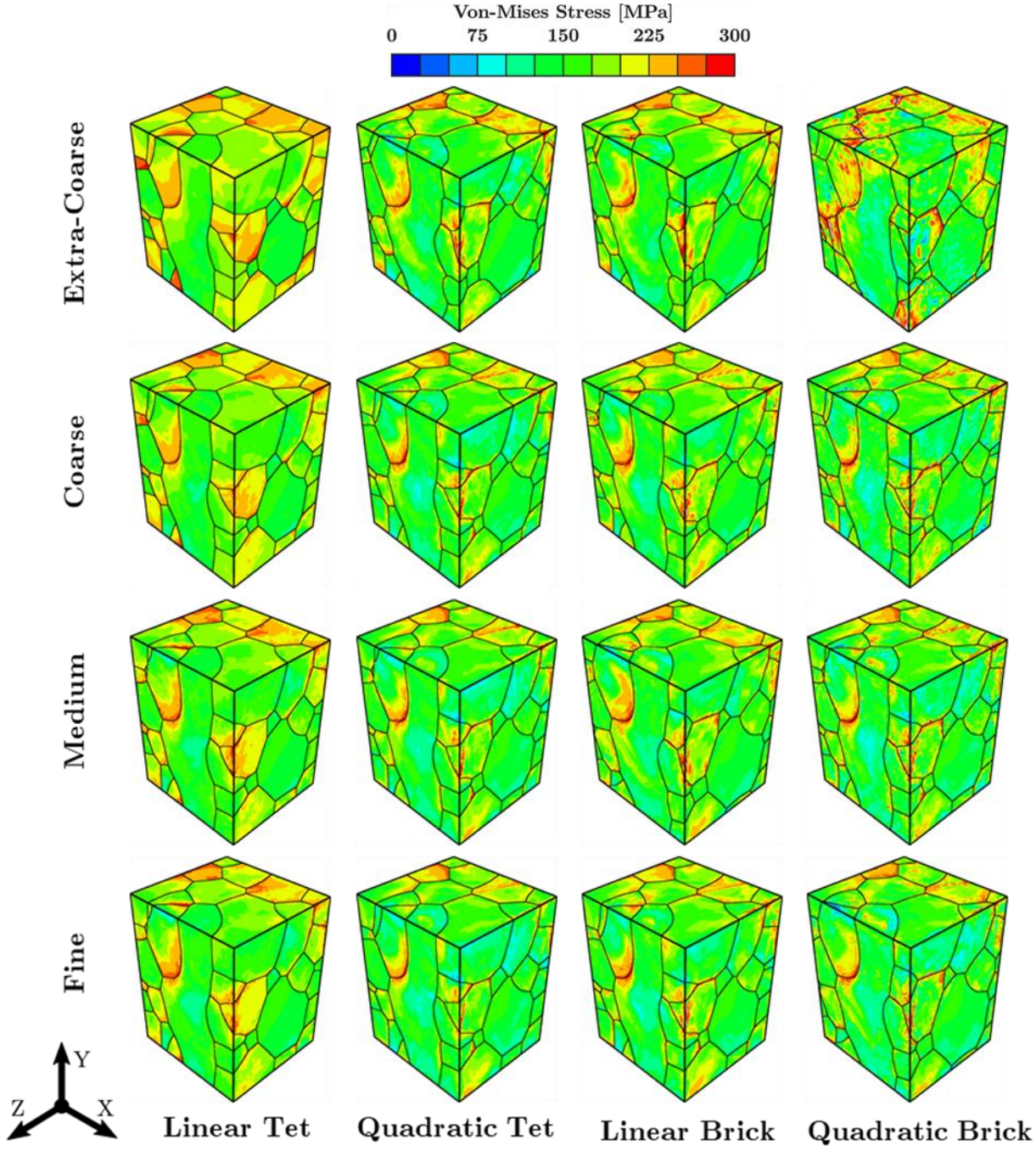

Figure 3. Von Mises stress contours after simple tension to a displacement of U = 0.22.

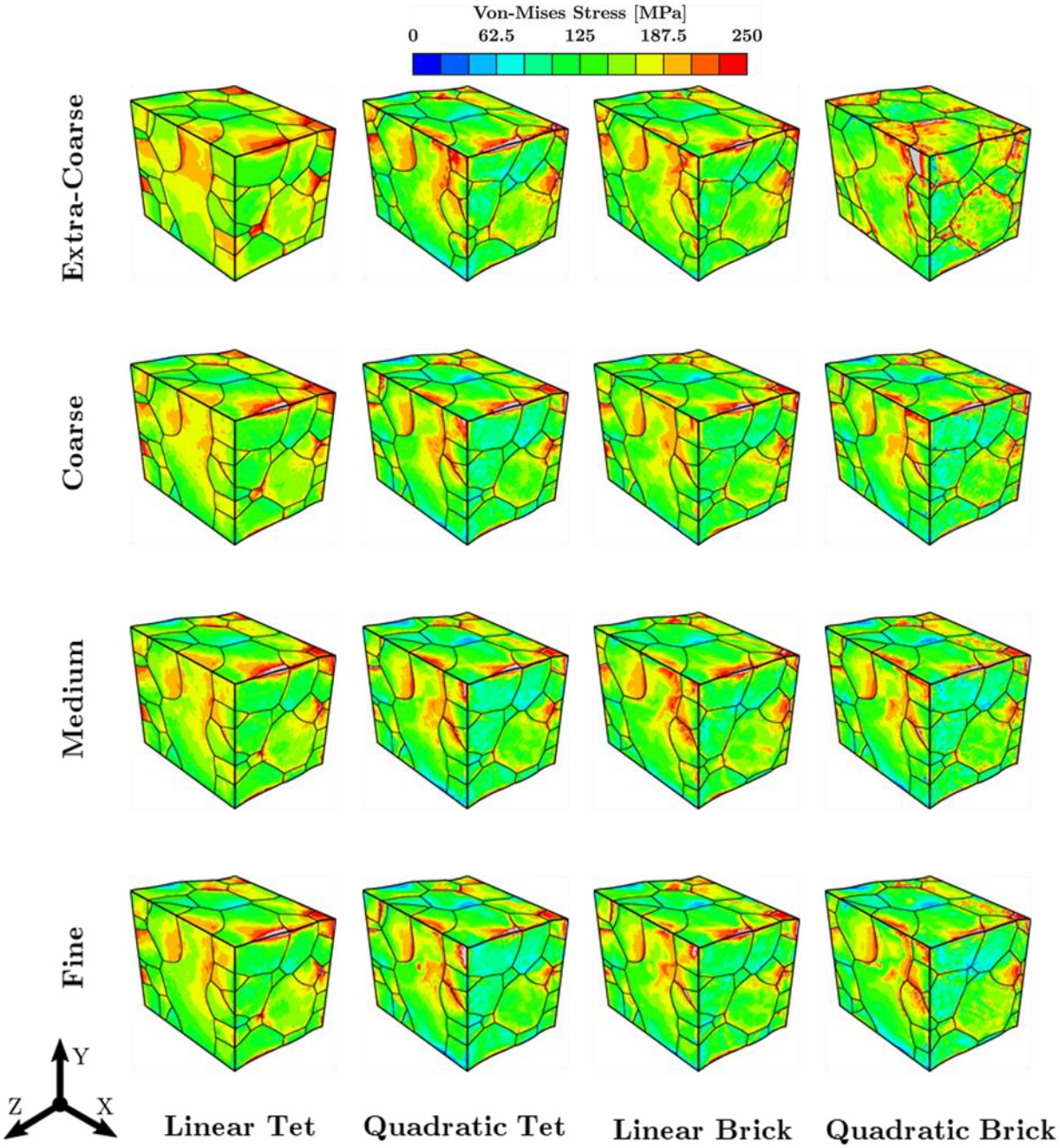

Figure 4. Von Mises stress contours after simple shear to a displacement of 0.22.

a

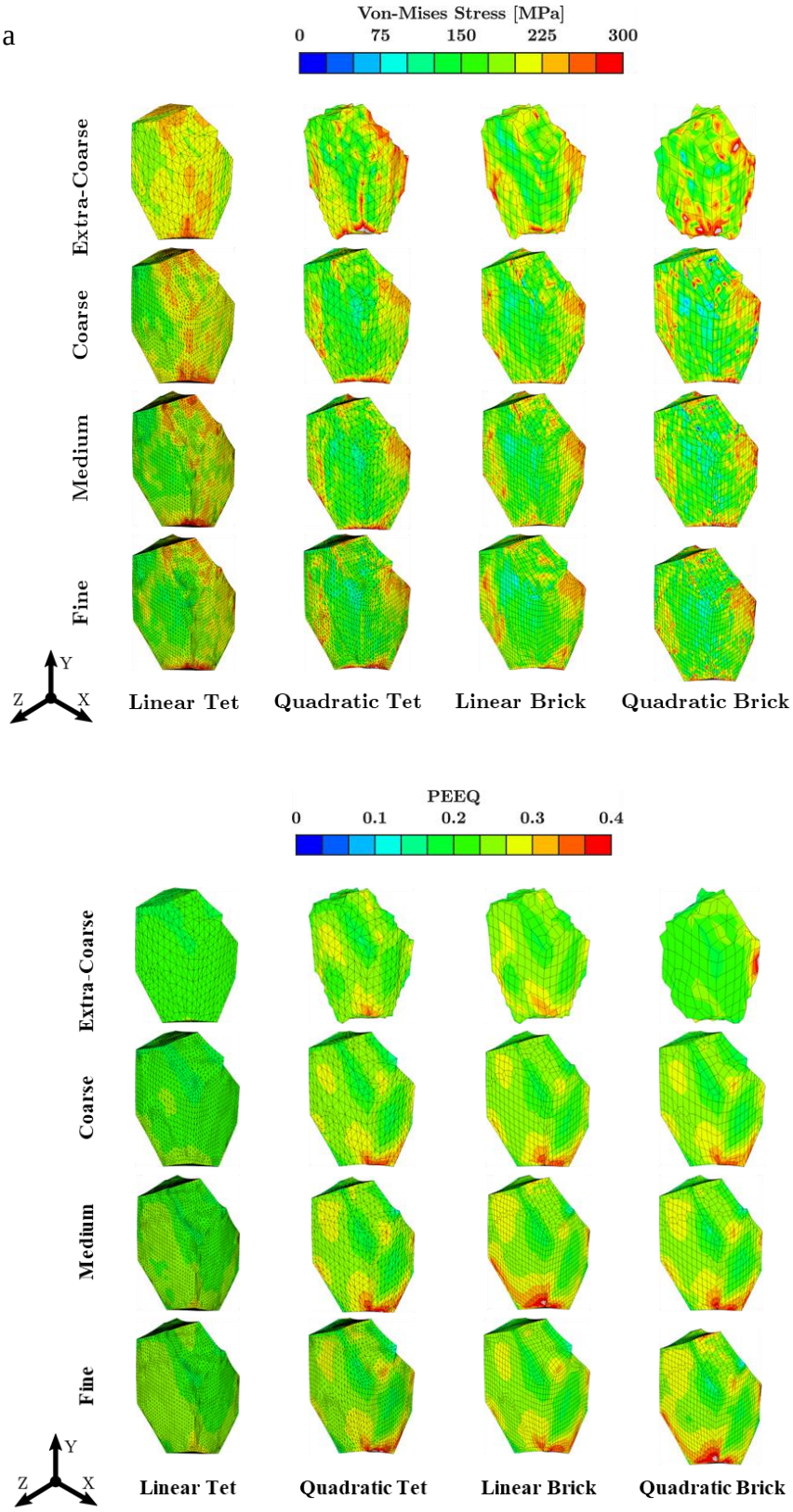
Von-Mises Stress [MPa]
0
75
150
225
300
Extra-Coarse
Coarse
Medium
Fine
Y
Z
X
Linear Tet
Quadratic Tet
Linear Brick
Quadratic Brick
PEEQ
0
0.1
0.2
0.3
0.4
Extra-Coarse
Coarse
Medium
Fine
Y
Z
X
Linear Tet
Quadratic Tet
Linear Brick
Quadratic Brick

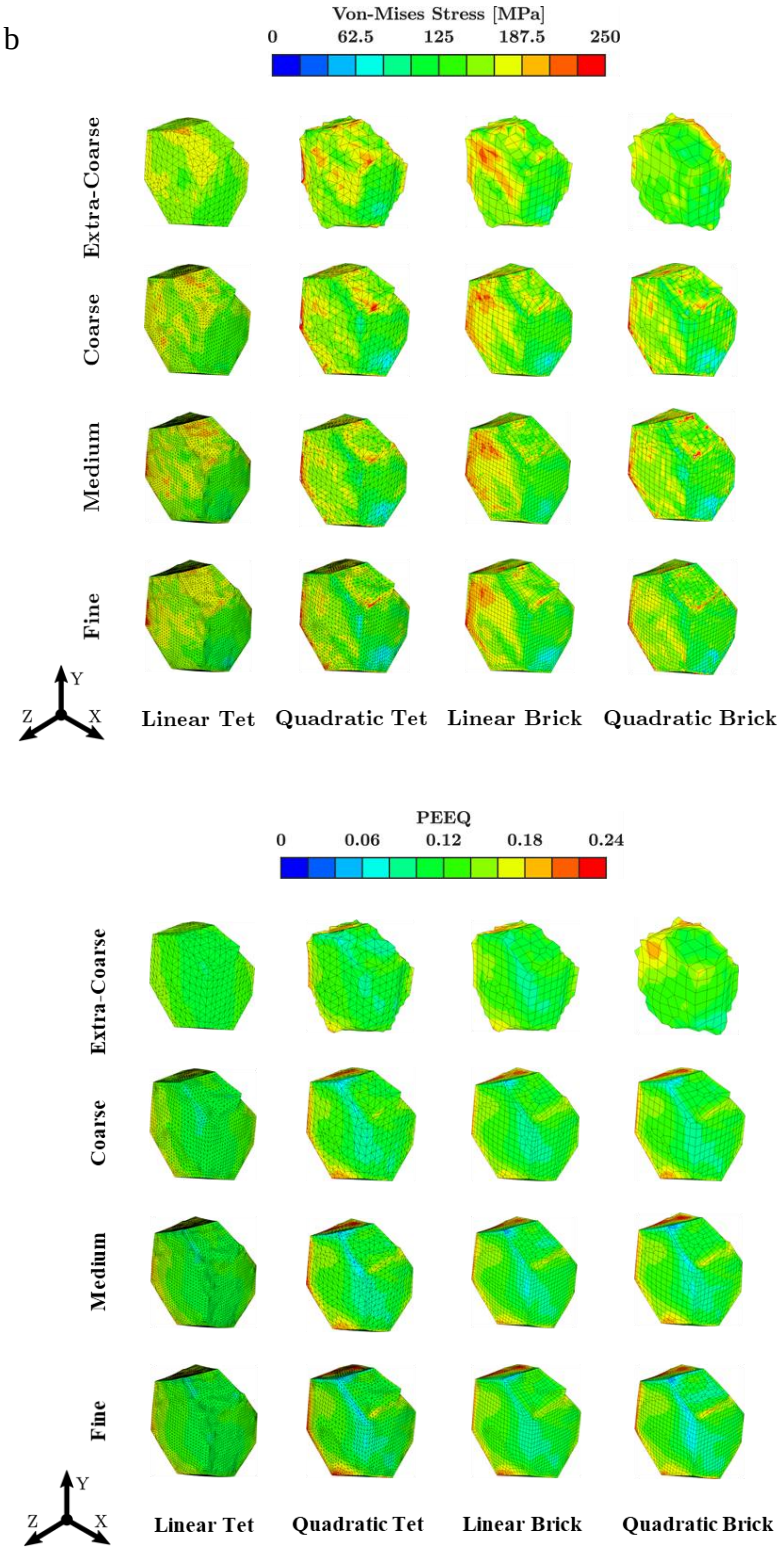

Figure 5. Contours of selected mechanical fields for the central grain deformed in (a) ST and (b) SS.

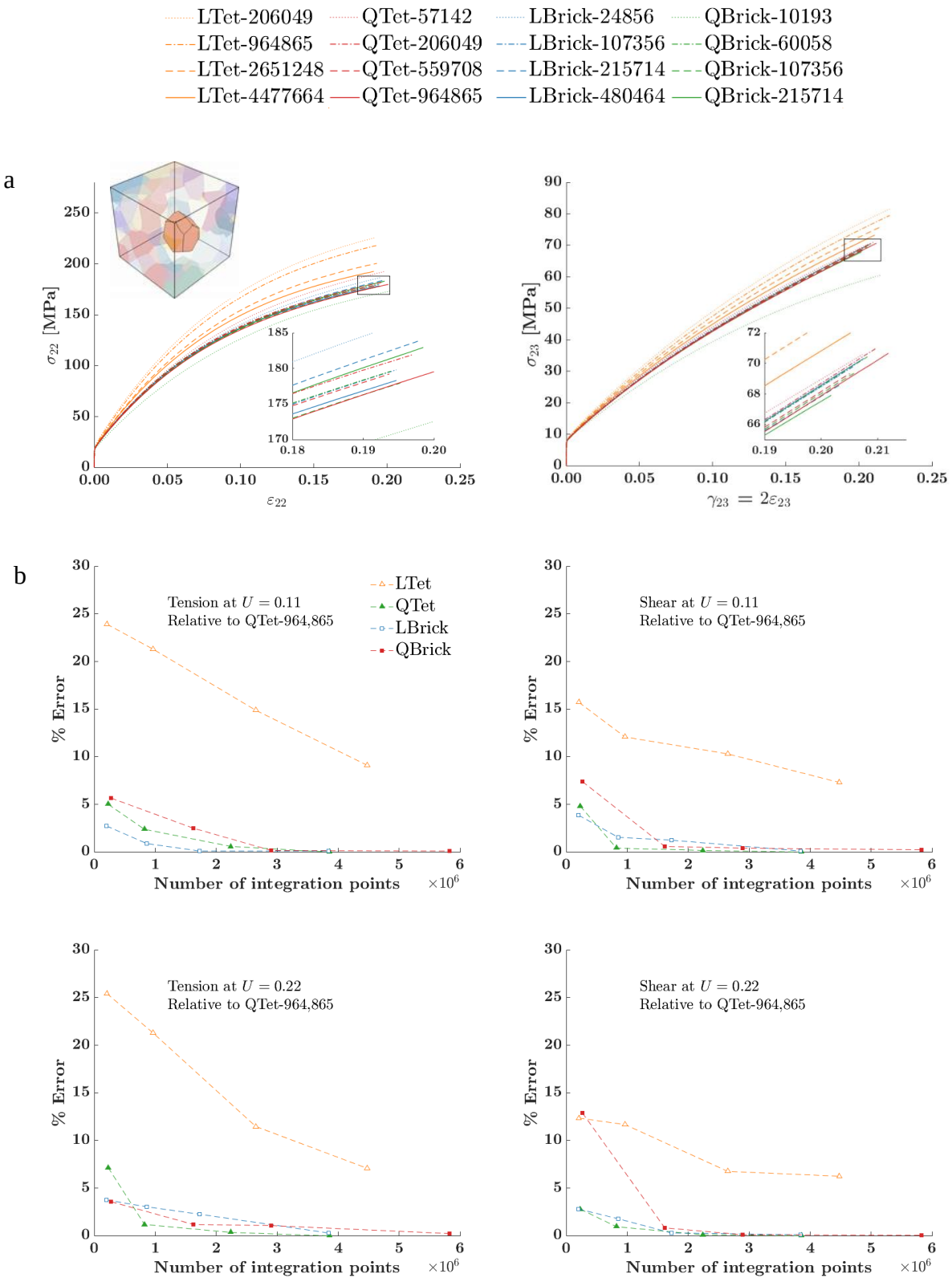

Figure 6. (a) Stress component - strain component curves for the central grain. The insert shows the location of the central grain. (b) Error plots defined using Eq. (15) after the displacement of U = 0.11 and U = 0.22.

4. Discussion

This work presents results from 32 large-scale simulations with four element types at various mesh resolutions to understand discretization errors in polycrystalline CPFE models. To authors knowledge, this is the first study comparing quantitatively the solution accuracy and computational time as a function of element type and mesh resolution in CPFE simulations of polycrystalline grain structures. The starting model is a voxel-based polycrystalline grain structure (microstructural cell) created synthetically by a phase field grain growth simulation, which is then converted to interface conformal hexahedral and tetrahedral meshes. In doing so, procedures for interface-conformal mesh generation over complex shapes for tetrahedral and hexahedral elements are advanced. The procedures rely on software packages Patran and Cubit/Sculpt, respectively. Note that while interface conformal FE meshes are preferred, especially for predicting localized behavior such as damage formation and failure, it is very challenging to rapidly generate 3D conformal meshes of polycrystalline microstructures. The inherent difficulties in describing complex shapes with hexahedral elements as opposed to relatively flexible tetrahedral elements make the latest version of Cubit/Sculpt very successful mesh generation tool to obtain interface-conformal hexahedral meshes of polycrystalline microstructures. Also note that the time to generate hexahedral mesh is significantly longer and is semi-automatic, mainly due to additional operations (inclusion of elements and smoothing) to maintain good mesh quality, relative to automatic and rapid mesh generation of tetrahedral mesh starting from the surface mesh of constituent grains.

Given the element type and the number of elements i.e. their degrees-of-freedom, the computational time involved in simulations varied. A parallel computing infrastructure is utilized to run the jobs on a single or multiple workstations working concurrently. CPFE simulations

with various finite element meshes show the trend that the computational time per CPU scales with the degrees of freedom for every element type. As expected, models with more elements require more time per CPU than smaller sized models. As the time per CPU scales with the number of degrees of freedom, linear elements are faster per CPU than the corresponding quadratic elements. Since brick elements show faster convergence rate than tetrahedral elements, even the linear brick elements approach at an equivalent solution accuracy at cheaper computational cost relative to the quadratic tetrahedral elements.

The study of element type and mesh resolution is essential for attempting to predict the evolutions of local fields during plastic deformation, i.e. local stress-strain developments, especially while predicting phenomena such as void formations and propagation. Such studies are challenging in crystal plasticity modeling as these models are not only computationally intensive but also rely on explicit meshing of grain structure using a large number of elements of an appropriate type. Resolving every grain within a grain structure domain complicates mesh convergence study as the convergence is strongly influenced by the initial shape and size of grains, crystallography, global and local loadings as a consequence of applied boundary conditions and also the hardening law to a smaller extent. Fig. 7 shows locations of the peak stress localizations upon ST and SS simulations performed in the present work. As is evident, the 'hot spot' is at a triple junction for the model deformed in ST and at a grain boundary for the model deformed in SS. The actual location is therefore dependent on the imposed boundary condition and also varies with the element type and mesh refinement. Specifically, while linear/quadratic hex and quadratic tet consistently predict the same locations of the hot spots in stress, the liner tet elements deviate and vary with mesh resolution. Additionally, quadratic hex

elements over predict the level of pressure and resulting stress triaxiality. As a result, these elements are not recommended for studying voiding in polycrystals.

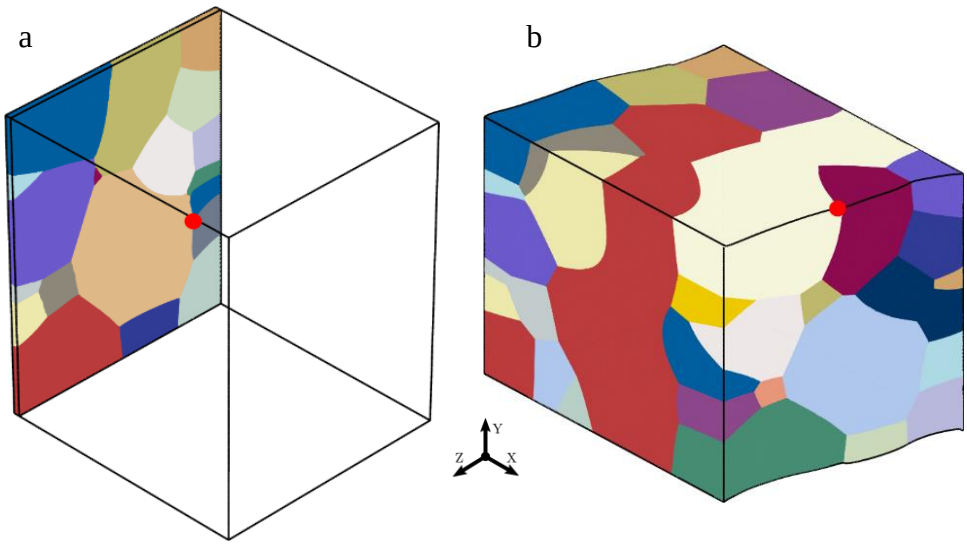

Figure 7. Locations of the mechanical extremes per model indicated by red dots after (a) ST and (b) SS.

Simulation results in this work suggest that linear tetrahedral element is not appropriate for CPFE modeling of grain structures, although a number of studies utilized it in grain structure modeling, including the works of present authors [70, 72]. These elements are overly stiff requiring extremely fine meshes to arrive at accurate solutions [105]. Moreover, these elements are susceptible to volumetric locking in modeling of incompressible solids (pressure plots in Figs. 3 and 4). Mesh refinement to about 4.5 x 10^6 linear tetrahedral elements requires large RAM memory. Such refinement only reduced the error to about 10% (Fig. 6). Further refinement becomes impractical because of enormous CPU memory and # of cores requirements. Key advantages of tetrahedral elements are their geometric adaptability and suitability for rapid and automatic meshing algorithms. These elements are very convenient to discretize complex shapes.

However, it is possible to take these advantages only for quadratic tetrahedral elements, as will be discussed shortly.

The discussion above has focused primarily on the performances of linear tetrahedral elements for modeling of grain structures. We now focus on the performances of the hexahedral elements. Quadratic hexahedral elements are not recommended for severe element distortions as a consequence of large plastic strains or very high strain gradients [105]. According to the Abaqus User Manual [105], second-order reduced-integration elements in Abaqus/Standard are likely to be more accurate than the corresponding fully-integrated elements. Considering that C3D20 has 27 IPs, while the corresponding C3D20R reduced integration element has only 8 IPs, the simulations are faster by approximately a factor of three. However, these simulations are not performed in the present work because the linear brick elements and C3D20R yield similar results. For the first-order reduced integration (C3D8R) hexahedral element is not recommended primarily due to its propensity to the hourglass effect [105]. In contrast, while the fully integrated elements do not show the hourglass effect, they are susceptible to volumetric locking. As stated above, the volumetric locking can appear for fully integrated elements while modeling incompressible solids. Spurious pressure fields can arise at IPs, causing the element to behave as very stiffly while enforcing the volume conservation. Quadratic fully integrated elements are the most susceptible to lock at larger plastic strains. However, the reduced-integration of quadratic elements eliminates volumetric locking. In contrast to quadratic elements, linear hexahedral elements selectively use reduced integration and do not lock. Mesh refinement helps to reduce volumetric locking of quadratic elements. Pressure fields in Figs. 3 and 4 show a checkerboard pattern, especially for quadratic hexahedral elements. The checkerboard pattern is a sign of volumetric locking. As is evident, mesh refinement helps in reducing the pattern. Moreover,

quadratic hexahedral elements are the element type first to introduce error greater than 5% relative to the fine Qtet-964,865 mesh with coarsening the resolution for a given number of integration points. The error comes at the expense of losing some geometry features with coarsening hexahedral elements.

Our results suggest that quadratic tetrahedral and linear hexahedral elements are recommended for CPFE modeling of grain structures. According to the pressure maps, linear hexahedral elements are least prone to volumetric locking. Also, hexahedral elements usually converged to a solution of equivalent accuracy at less computational cost compared to quadratic tetrahedral elements. Considering that shape of the grains is very complex and far from being rectangular for hexahedral elements, tetrahedral elements are far more flexible and desirable. Therefore, although structured hexahedral elements in 3D analyses are desirable, since they give the best results with the minimum computational cost, tetrahedral elements are recommended. Extra coarse tetrahedral elements still describe the geometry reasonably well while hexahedral elements fail to capture the geometry (Fig. 2b).

Excluding linear tetrahedral elements, CPFE simulations show that the deviation between model predictions with about 200,000 elements performed using different element types would be within 5%. Further mesh refinements improve the accuracy at the expense of increasing the computational time and memory requirements. This strongly suggests that quadratic tetrahedral elements are the best compromise between accuracy and computational speed in CPFE simulation of polycrystals.

5. Conclusions

Suitability of the four most commonly used element types along with varying mesh resolution in CPFE modeling of grain structures are investigated using large-scale simulations. A voxel-based polycrystalline grain structure is generated by a phase field grain growth simulation and converted to interface conformal hexahedral and tetrahedral element meshes of variable resolution. Procedures for such interface-conformal mesh generation over complex shapes relying on Patran for tetrahedral and Cubit/Sculpt for hexahedral elements are described. CPFE simulations of simple tension and simple shear deformation conditions are performed. Minor sensitivity of models to these boundary conditions is observed. The computational time per CPU was measured to scale with the degrees of freedom for every element type. As the time per CPU scales with the number of degrees of freedom, linear elements are faster per CPU than the corresponding quadratic elements. However, hexahedral elements exhibit a better convergence rate than quadratic tetrahedral elements and arrive at a solution of equivalent accuracy to quadratic tetrahedral elements at less computational cost. Simulation results suggest that linear tetrahedral element is not appropriate for CPFE modeling of grain structures as these elements are overly stiff. Mesh refinement only moderately improve such simulation results. Results also show that quadratic brick elements are not suitable for large plastic straining of complex geometries due to their propensity to volumetric locking. Similarly, mesh refinement only reduces the checkerboard pattern in pressure fields. The mesh resolution studies in capturing mechanical fields shows that brick elements are more sensitive than tetrahedral elements, which can be associated to geometric adaptability of tetrahedral elements. Geometry features can be lost with brick element coarsening. Moreover, tetrahedral elements are suitability for rapid and automatic meshing algorithms. In summary, quadratic tetrahedral and linear hexahedral elements

are more accurate for crystal plasticity finite element modeling than linear tetrahedral and quadratic hexahedral elements. Furthermore, tetrahedral elements are more desirable due to fast mesh generation and flexibility to describe complex grain structure geometries. It is anticipated that the results from this study provide useful guidance for future CPFE modeling of grain structures. These guidance should be applicable to other crystal plasticity models as constitutive models and hardening formulations have minor effects on mesh sensitivity.

Acknowledgements

This work is based upon a project supported by the U.S. National Science Foundation under grant no. CMMI-1650641. The authors gratefully acknowledge this support. This paper describes objective technical results and analysis. Any subjective views or opinions that might be expressed in the paper do not necessarily represent the views of the U.S. Department of Energy or the United States Government. Sandia National Laboratories is a multi-mission laboratory managed and operated by National Technology and Engineering Solutions of Sandia, LLC., a wholly owned subsidiary of Honeywell International, Inc., for the U.S. Department of Energy's National Nuclear Security Administration under contract DE-NA0003525.

Appendix A

Table 6. Bunge-Euler angles (ϕ_1, Φ, ϕ_2) in degrees and corresponding volume fraction (VF) of crystals used to initialize the model.

#	ϕ_1	Φ	ϕ_2	VF	#	ϕ_1	Φ	ϕ_2	VF
1	285.4	78.7	30.5	0.005631	27	285.4	78.2	21.5	0.024535
2	39.5	60.7	12.8	0.070512	28	351.2	62.8	30.5	0.003533
3	338	86.1	21.5	0.155554	29	188.8	50.7	12.8	0.000113
4	250.2	50.7	12.8	0.012342	30	127.3	86.1	21.5	0.038058
5	144.9	86.1	21.5	0.001854	31	4.4	77.7	4.3	0.012009
6	153.7	61.5	21.5	0.087928	32	22	64.8	40.1	0.00757
7	180	78.7	30.5	0.061393	33	57.1	78.2	21.5	0.063121
8	285.4	53.3	30.5	0.012954	34	22	51.7	21.5	0.024633
9	188.8	86.1	21.5	0.000647	35	232.7	60.7	12.8	0.011798
10	180	86	12.8	0.031774	36	285.4	50.3	4.3	0.003005
11	294.1	60.7	12.8	0.000082	37	223.9	51.7	21.5	0.001046
12	232.7	64.8	40.1	0.009366	38	118.5	72.3	40.1	0.041698
13	65.9	86.2	30.5	0.004408	39	259	70.1	21.5	0.004197
14	136.1	77.7	4.3	0.001502	40	48.3	86.5	40.1	0.001065
15	162.4	53.3	30.5	0.000314	41	250.2	86.1	21.5	0.001816
16	338	50.7	12.8	0.021943	42	101	77.9	12.8	0.000527
17	294.1	50.3	4.3	0.036506	43	223.9	86.2	30.5	0.003741
18	144.9	77.9	12.8	0.025753	44	30.7	62.8	30.5	0.002037
19	92.2	79.5	40.1	0.000605	45	22	86	12.8	0.001655
20	351.2	64.8	40.1	0.002333	46	109.8	50.7	12.8	0.001142
21	144.9	78.2	21.5	0.000108	47	320.5	85.9	4.3	0.025865
22	13.2	78.2	21.5	0.026761	48	30.7	86	12.8	0.010391
23	48.3	62.8	30.5	0.006717	49	22	69.3	4.3	0.03423
24	171.2	72.3	40.1	0.010872	50	329.3	78.2	21.5	0.04146
25	241.5	60.7	12.8	0.000311	51	57.1	86.2	30.5	0.01531
26	153.7	60.7	12.8	0.027493	52	136.1	86.5	40.1	0.009783

Appendix B

a

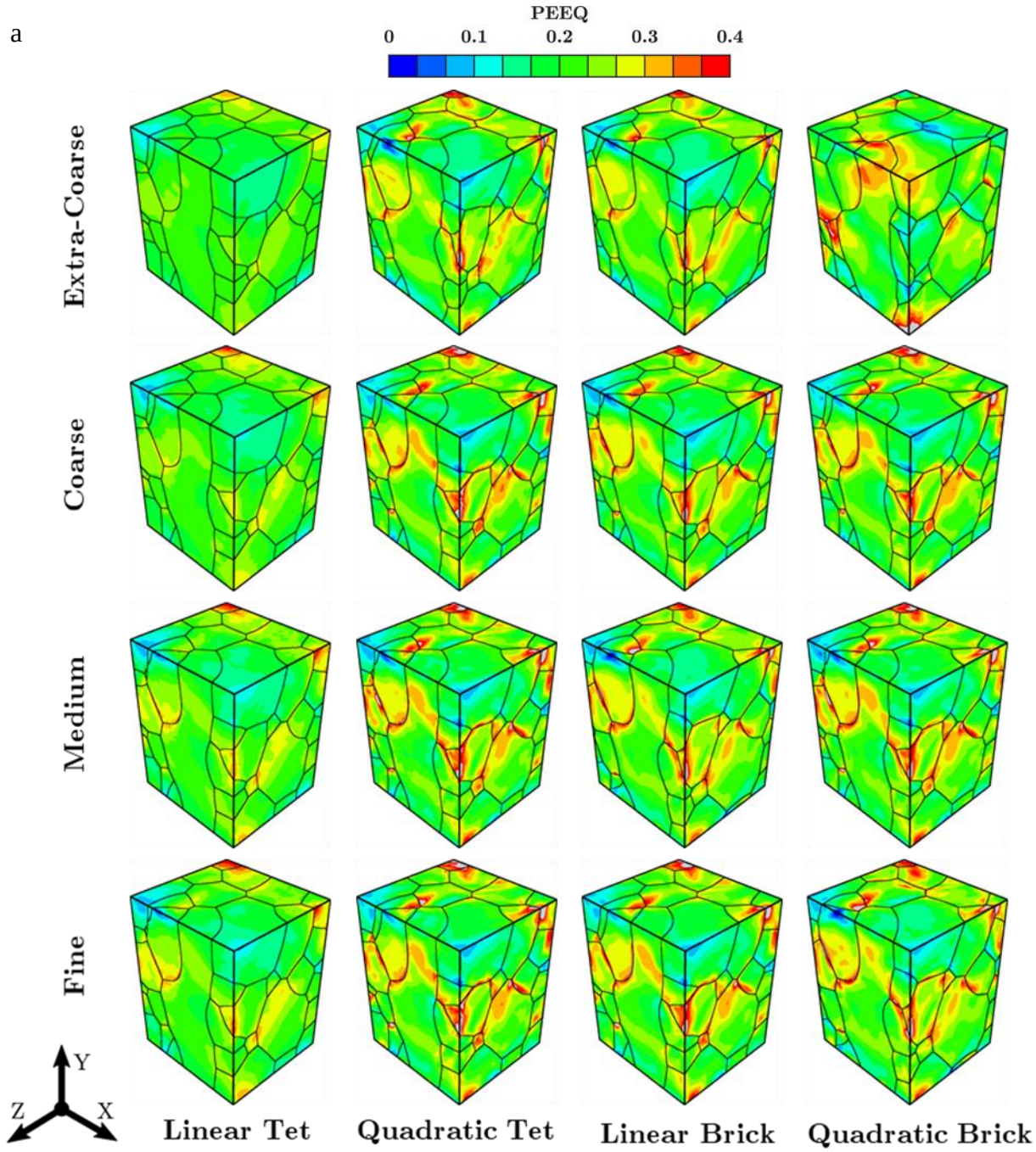
PEEQ
0
0.1
0.2
0.3
0.4
Extra-Coarse
Coarse
Medium
Fine
Y
Z
X
Linear Tet
Quadratic Tet
Linear Brick
Quadratic Brick

b

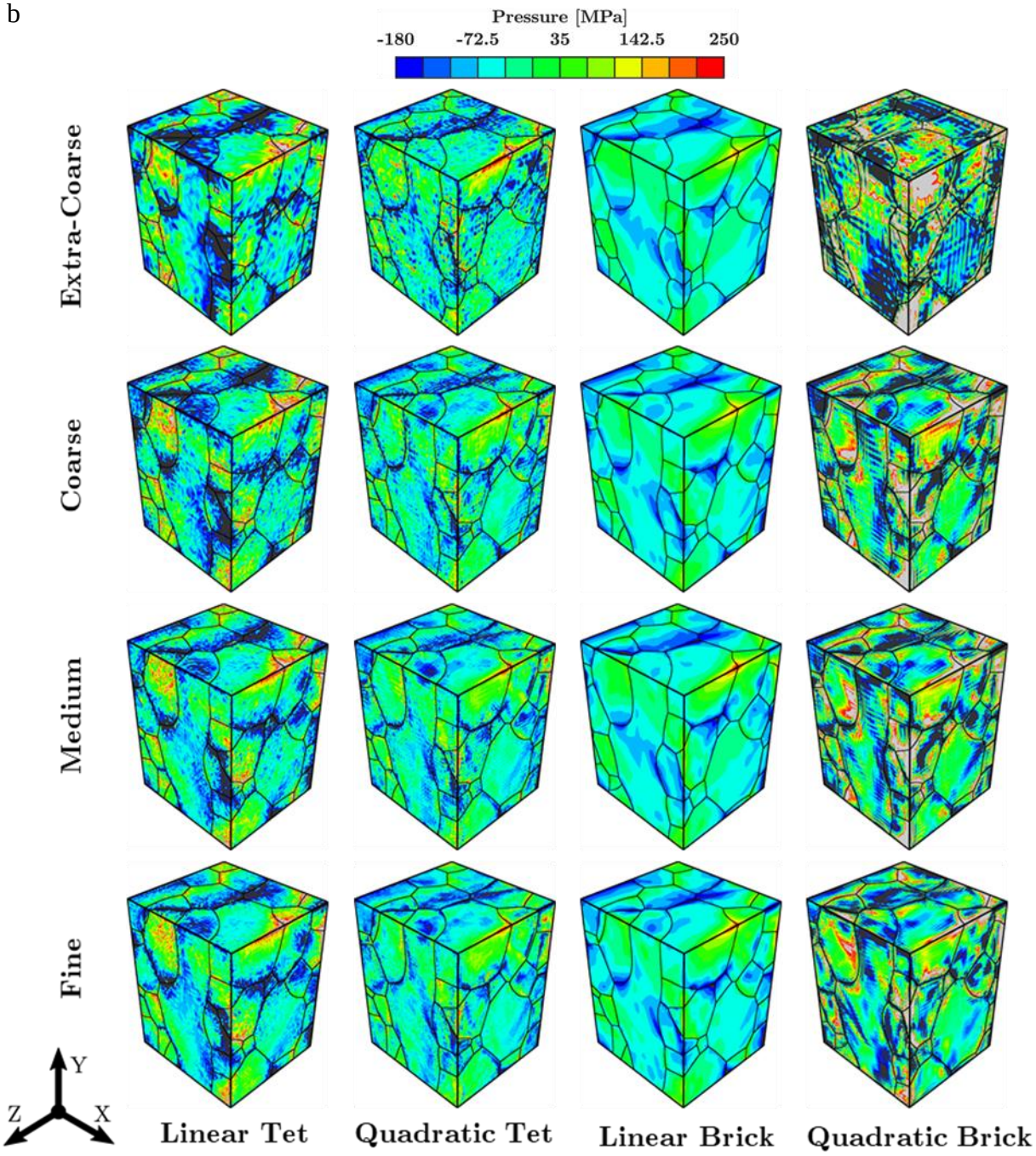

Figure 8. (a) Equivalent strain and (b) pressure contours after simple tension to a displacement of U = 0.22.

a

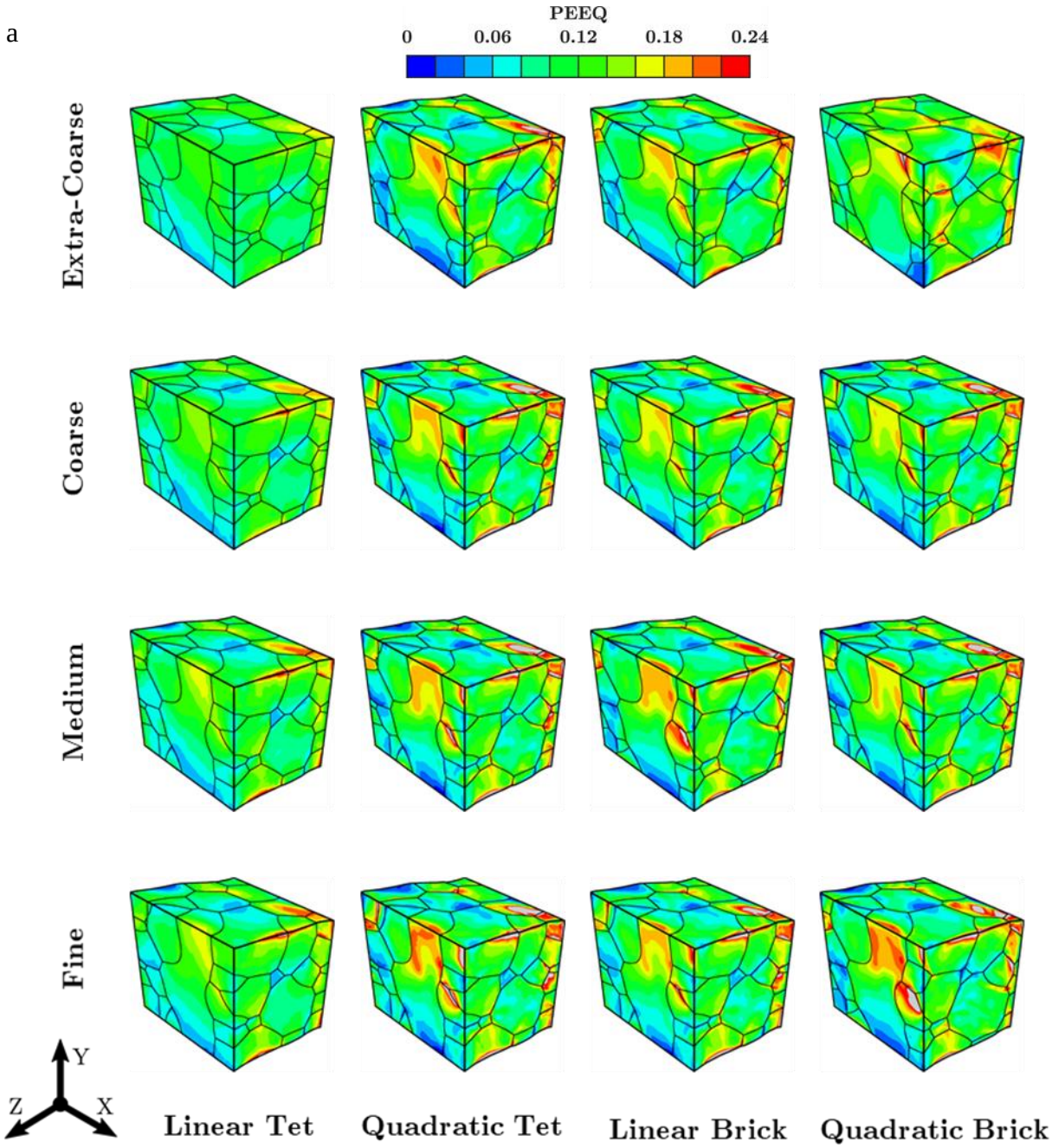
PEEQ
0
0.06
0.12
0.18
0.24
Extra-Coarse
Coarse
Medium
Fine
Y
Z
X
Linear Tet
Quadratic Tet
Linear Brick
Quadratic Brick

b

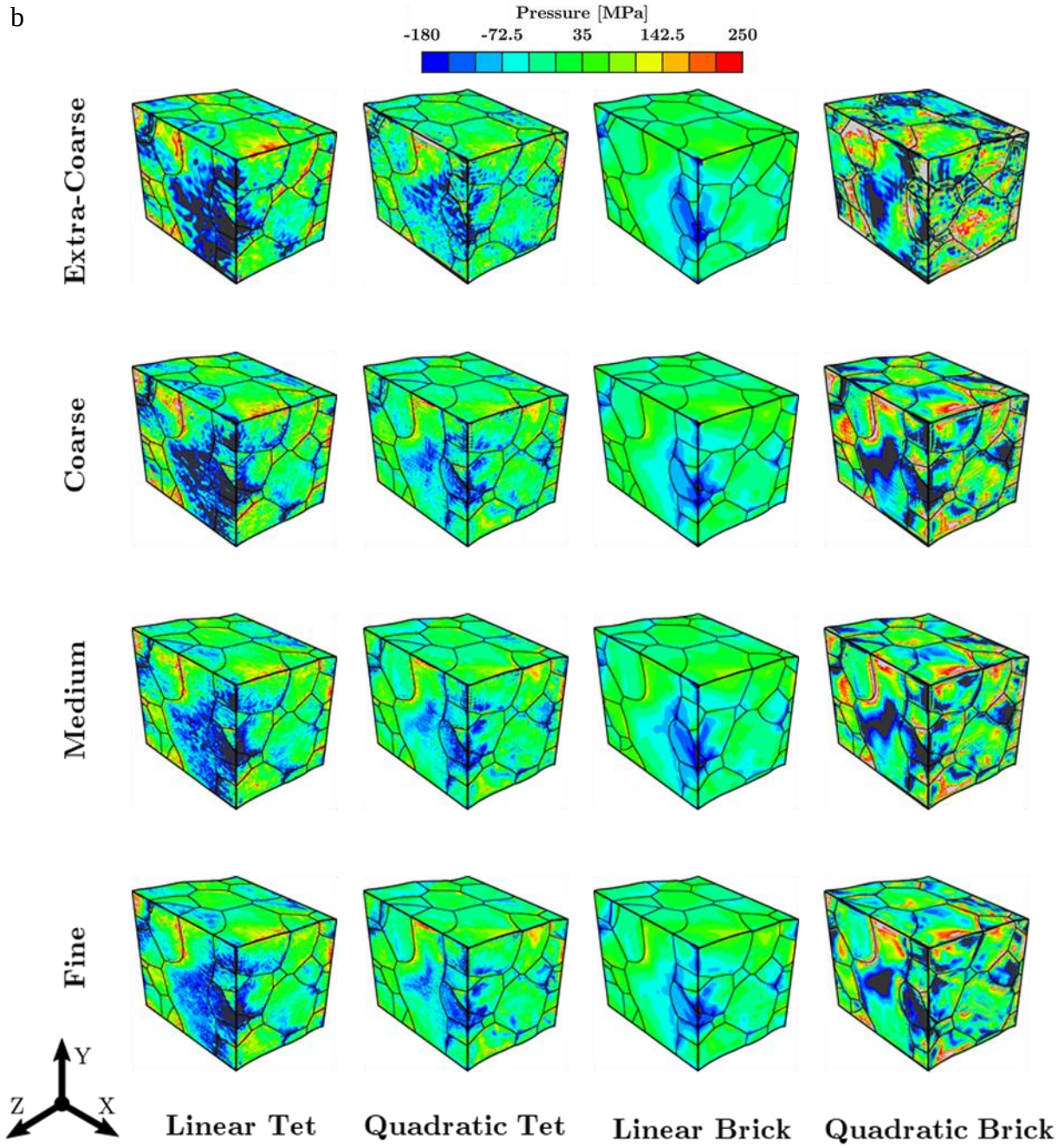

Figure 9. (a) Equivalent strain and (b) pressure contours after simple shear to a displacement of 0.22.

References

1. Eghtesad A, Zecevic M, Lebensohn RA, McCabe RJ and Knezevic M (2018) Spectral database constitutive representation within a spectral micromechanical solver for computationally efficient polycrystal plasticity modelling. Comput Mech 61: 89-104

2. Bathe K-J (1996) Finite element procedures Englewood Cliffs, N.J.: Prentice Hall

3. Eghtesad A, Barrett TJ, Germaschewski K, Lebensohn RA, McCabe RJ and Knezevic M (2018) OpenMP and MPI implementations of an elasto-viscoplastic fast Fourier transform-based micromechanical solver for fast crystal plasticity modeling. Advances in Engineering Software 126: 46-60

4. Eghtesad A, Germaschewski K, Lebensohn RA and Knezevic M (2020) A multi-GPU implementation of a full-field crystal plasticity solver for efficient modeling of high-resolution microstructures. Computer Physics Communications: 107231

5. Peirce D, Asaro RJ and Needleman A (1982) An analysis of nonuniform and localized deformation in ductile single crystals. Acta Metall 30: 1087-1119

6. Diard O, Leclercq S, Rousselier G and Cailletaud G (2002) Distribution of normal stress at grain boundaries in multicrystals: application to an intergranular damage modeling. Comput Mater Sci 25: 73-84

7. Jahedi M, Ardeljan M, Beyerlein IJ, Paydar MH and Knezevic M (2015) Enhancement of orientation gradients during simple shear deformation by application of simple compression. J Appl Phys 117: 214309

8. Ardeljan M, McCabe RJ, Beyerlein IJ and Knezevic M (2015) Explicit incorporation of deformation twins into crystal plasticity finite element models. Computer Methods in Applied Mechanics and Engineering 295: 396-413

9. Zhao Z, Ramesh M, Raabe D, Cuitiño AM and Radovitzky R (2008) Investigation of three-dimensional aspects of grain-scale plastic surface deformation of an aluminum oligocrystal. Int J Plast 24: 2278-2297

10. Lim H, Carroll JD, Battaile CC, Buchheit TE, Boyce BL and Weinberger CR (2014) Grain-scale experimental validation of crystal plasticity finite element simulations of tantalum oligocrystals. Int J Plast 60: 1-18

11. Savage DJ, Beyerlein IJ and Knezevic M (2017) Coupled texture and non-Schmid effects on yield surfaces of body-centered cubic polycrystals predicted by a crystal plasticity finite element approach. International Journal of Solids and Structures 109: 22-32

12. Knezevic M, Levinson A, Harris R, Mishra RK, Doherty RD and Kalidindi SR (2010) Deformation twinning in AZ31: Influence on strain hardening and texture evolution. Acta Mater 58: 6230-6242

13. Kalidindi SR, Bronkhorst CA and Anand L (1992) Crystallographic texture evolution in bulk deformation processing of FCC metals. J Mech Phys Solids 40: 537-569

14. Kalidindi SR, Duvvuru HK and Knezevic M (2006) Spectral calibration of crystal plasticity models. Acta Mater 54: 1795-1804

15. Miehe C, Schröder J and Schotte J (1999) Computational homogenization analysis in finite plasticity Simulation of texture development in polycrystalline materials. Computer Methods in Applied Mechanics and Engineering 171: 387-418

16. Beaudoin AJ, Dawson PR, Mathur KK, Kocks UF and Korzekwa DA (1994) Application of polycrystal plasticity to sheet forming. Computer Methods in Applied Mechanics and Engineering 117: 49-70

17. Sarma GB and Dawson PR (1996) Texture predictions using a polycrystal plasticity model incorporating neighbor interactions. Int J Plast 12: 1023-1054

18. Ardeljan M, Beyerlein IJ and Knezevic M (2014) A dislocation density based crystal plasticity finite element model: Application to a two-phase polycrystalline HCP/BCC composites. J Mech Phys Solids 66: 16-31

19. Sarma GB and Dawson PR (1996) Effects of interactions among crystals on the inhomogeneous deformations of polycrystals. Acta Mater 44: 1937-1953

20. Mika DP and Dawson PR (1998) Effects of grain interaction on deformation in polycrystals. Mater Sci Eng A 257: 62-76

21. Delannay L, Jacques PJ and Kalidindi SR (2006) Finite element modeling of crystal plasticity with grains shaped as truncated octahedrons. Int J Plast 22: 1879-1898

22. Ritz H and Dawson P (2008) Sensitivity to grain discretization of the simulated crystal stress distributions in FCC polycrystals. Modelling and Simulation in Materials Science and Engineering 17: 015001

23. Kalidindi SR, Bhattacharya A and Doherty R (2004) Detailed Analysis of Plastic Deformation in Columnar Polycrystalline Aluminum Using Orientation Image Mapping and Crystal Plasticity Models. Proceedings of the Royal Society of London: Mathematical, Physical and Engineering Sciences 460: 1935 - 1956

24. Diard O, Leclercq S, Rousselier G and Cailletaud G (2005) Evaluation of finite element based analysis of 3D multicrystalline aggregates plasticity: Application to crystal plasticity model identification and the study of stress and strain fields near grain boundaries. Int J Plast 21: 691-722

25. Shenoy M, Tjiptowidjojo Y and McDowell D (2008) Microstructure-sensitive modeling of polycrystalline IN 100. Int J Plast 24: 1694-1730

26. Ardeljan M, Savage DJ, Kumar A, Beyerlein IJ and Knezevic M (2016) The plasticity of highly oriented nano-layered Zr/Nb composites. Acta Mater 115: 189-203

27. Lim H, Battaile CC, Bishop JE and Foulk JW (2019) Investigating mesh sensitivity and polycrystalline RVEs in crystal plasticity finite element simulations. Int J Plast 121: 101-115

28. Lim H, Abdeljawad F, Owen SJ, Hanks BW, Foulk JW and Battaile CC (2016) Incorporating physically-based microstructures in materials modeling: Bridging phase field and

crystal plasticity frameworks. Modelling and Simulation in Materials Science and Engineering 24: 045016

29. Lim H, Carroll JD, Battaile CC, Boyce BL and Weinberger CR (2015) Quantitative comparison between experimental measurements and CP-FEM predictions of plastic deformation in a tantalum oligocrystal. International Journal of Mechanical Sciences 92: 98-108

30. Knezevic M and Kalidindi SR (2007) Fast computation of first-order elastic-plastic closures for polycrystalline cubic-orthorhombic microstructures. Comput Mater Sci 39: 643-648

31. Taylor GI (1938) Plastic strain in metals. Journal of the Institute of Metals 62: 307-324

32. Lebensohn RA and Tomé CN (1993) A self-consistent anisotropic approach for the simulation of plastic deformation and texture development of polycrystals: Application to zirconium alloys. Acta Metall Mater 41: 2611-2624

33. Lebensohn RA, Zecevic M, Knezevic M and McCabe RJ (2016) Average intragranular misorientation trends in polycrystalline materials predicted by a viscoplastic self-consistent approach. Acta Mater 104: 228-236

34. Zecevic M, Pantleon W, Lebensohn RA, McCabe RJ and Knezevic M (2017) Predicting intragranular misorientation distributions in polycrystalline metals using the viscoplastic self-consistent formulation. Acta Mater 140: 398-410

35. Knezevic M, Kalidindi SR and Fullwood D (2008) Computationally efficient database and spectral interpolation for fully plastic Taylor-type crystal plasticity calculations of face-centered cubic polycrystals. Int J Plast 24: 1264-1276

36. Knezevic M, Al-Harbi HF and Kalidindi SR (2009) Crystal plasticity simulations using discrete Fourier transforms. Acta Mater 57: 1777-1784

37. Zecevic M, Knezevic M, Beyerlein IJ and McCabe RJ (2016) Origin of texture development in orthorhombic uranium. Mater Sci Eng A 665: 108-124

38. Knezevic M, Beyerlein IJ, Lovato ML, Tomé CN, Richards AW and McCabe RJ (2014) A strain-rate and temperature dependent constitutive model for BCC metals incorporating non-Schmid effects: Application to tantalum–tungsten alloys. Int J Plast 62: 93-104

39. Knezevic M, Capolungo L, Tomé CN, Lebensohn RA, Alexander DJ, Mihaila B and McCabe RJ (2012) Anisotropic stress-strain response and microstructure evolution of textured α-uranium. Acta Mater 60: 702-715

40. Knezevic M, Nizolek T, Ardeljan M, Beyerlein IJ, Mara NA and Pollock TM (2014) Texture evolution in two-phase Zr/Nb lamellar composites during accumulative roll bonding. Int J Plast 57: 16-28

41. Knezevic M and Savage DJ (2014) A high-performance computational framework for fast crystal plasticity simulations. Comput Mater Sci 83: 101-106

42. Knezevic M, Zecevic M, Beyerlein IJ and Lebensohn RA (2016) A numerical procedure enabling accurate descriptions of strain rate-sensitive flow of polycrystals within crystal visco-plasticity theory. Computer Methods in Applied Mechanics and Engineering 308: 468-482

43. Savage DJ and Knezevic M (2015) Computer implementations of iterative and non-iterative crystal plasticity solvers on high performance graphics hardware. Comput Mech 56: 677–690

44. Barrett TJ and Knezevic M (2019) Deep drawing simulations using the finite element method embedding a multi-level crystal plasticity constitutive law: Experimental verification and sensitivity analysis. Computer Methods in Applied Mechanics and Engineering 354: 245-270

45. De Berg M, Van Kreveld M, Overmars M and Schwarzkopf OC (2000) Computational geometry Springer

46. Zhang P, Karimpour M, Balint D and Lin J (2012) Three-dimensional virtual grain structure generation with grain size control. Mechanics of Materials 55: 89-101

47. Boots B (1982) The arrangement of cells in "random" networks. Metallography 15: 53-62

48. Aboav D (1970) The arrangement of grains in a polycrystal. Metallography 3: 383-390

49. Groeber MA and Jackson MA (2014) DREAM. 3D: A digital representation environment for the analysis of microstructure in 3D. Integrating Materials and Manufacturing Innovation 3: 5

50. Chen L-Q (2002) Phase-field models for microstructure evolution. Annual review of materials research 32: 113-140

51. Rollett A and Raabe D (2001) A hybrid model for mesoscopic simulation of recrystallization. Comput Mater Sci 21: 69-78

52. Rollett AD (1997) Overview of modeling and simulation of recrystallization. Prog Mater Sci 42: 79-99

53. Raabe D (1999) Introduction of a scalable three-dimensional cellular automaton with a probabilistic switching rule for the discrete mesoscale simulation of recrystallization phenomena. Philosophical Magazine A 79: 2339-2358

54. Marx V, Reher FR and Gottstein G (1999) Simulation of primary recrystallization using a modified three-dimensional cellular automaton. Acta Mater 47: 1219-1230

55. Spowart JE, Mullens HE and Puchala BT (2003) Collecting and analyzing microstructures in three dimensions: A fully automated approach. JOM 55: 35-37

56. Spowart JE (2006) Automated serial sectioning for 3-D analysis of microstructures. Scr Mater 55: 5-10

57. Zaafarani N, Raabe D, Singh R, Roters F and Zaefferer S (2006) Three-dimensional investigation of the texture and microstructure below a nanoindent in a Cu single crystal using 3D EBSD and crystal plasticity finite element simulations. Acta Mater 54: 1863-1876

58. Calcagnotto M, Ponge D, Demir E and Raabe D (2010) Orientation gradients and geometrically necessary dislocations in ultrafine grained dual-phase steels studied by 2D and 3D EBSD. Mater Sci Eng A 527: 2738-2746

59. Khorashadizadeh A, Raabe D, Zaefferer S, Rohrer G, Rollett A and Winning M (2011) Five-Parameter Grain Boundary Analysis by 3D EBSD of an Ultra Fine Grained CuZr Alloy Processed by Equal Channel Angular Pressing. Advanced Engineering Materials 13: 237-244

60. Zaefferer S, Wright S and Raabe D (2008) Three-dimensional orientation microscopy in a focused ion beam–scanning electron microscope: A new dimension of microstructure characterization. Metall Mater Trans A 39: 374-389

61. Yi S, Schestakow I and Zaefferer S (2009) Twinning-related microstructural evolution during hot rolling and subsequent annealing of pure magnesium. Mater Sci Eng A 516: 58-64

62. Uchic MD, Groeber MA, Dimiduk DM and Simmons JP (2006) 3D microstructural characterization of nickel superalloys via serial-sectioning using a dual beam FIB-SEM. Scr Mater 55: 23-28

63. Li SF, Lind J, Hefferan CM, Pokharel R, Lienert U, Rollett AD and Suter RM (2012) Three-dimensional plastic response in polycrystalline copper via near-field high-energy X-ray diffraction microscopy. Journal of Applied Crystallography 45: 1098-1108

64. Lind J, Li SF, Pokharel R, Lienert U, Rollett AD and Suter RM (2014) Tensile twin nucleation events coupled to neighboring slip observed in three dimensions. Acta Mater 76: 213-220

65. Stein CA, Cerrone A, Ozturk T, Lee S, Kenesei P, Tucker H, Pokharel R, Lind J, Hefferan C, Suter RM, Ingraffea AR and Rollett AD (2014) Fatigue crack initiation, slip localization and twin boundaries in a nickel-based superalloy. Current Opinion in Solid State and Materials Science 18: 244-252

66. Ludwig W, Schmidt S, Lauridsen EM and Poulsen HF (2008) X-ray diffraction contrast tomography: a novel technique for three-dimensional grain mapping of polycrystals. I. Direct beam case. Journal of Applied Crystallography 41: 302-309

67. Johnson G, King A, Honnicke MG, Marrow J and Ludwig W (2008) X-ray diffraction contrast tomography: a novel technique for three-dimensional grain mapping of polycrystals. II. The combined case. Journal of Applied Crystallography 41: 310-318

68. Qidwai SM, Turner DM, Niezgoda SR, Lewis AC, Geltmacher AB, Rowenhorst DJ and Kalidindi SR (2012) Estimating the response of polycrystalline materials using sets of weighted statistical volume elements. Acta Mater 60: 5284-5299

69. Choi YS, Groeber MA, Turner TJ, Dimiduk DM, Woodward C, Uchic MD and Parthasarathy TA (2012) A crystal-plasticity FEM study on effects of simplified grain representation and mesh types on mesoscopic plasticity heterogeneities. Mater Sci Eng A 553: 37-44

70. Knezevic M, Drach B, Ardeljan M and Beyerlein IJ (2014) Three dimensional predictions of grain scale plasticity and grain boundaries using crystal plasticity finite element models. Computer Methods in Applied Mechanics and Engineering 277: 239-259

71. Barrett TJ, Savage DJ, Ardeljan M and Knezevic M (2018) An automated procedure for geometry creation and finite element mesh generation: Application to explicit grain structure models and machining distortion. Comput Mater Sci 141: 269-281

72. Ardeljan M, Knezevic M, Nizolek T, Beyerlein IJ, Mara NA and Pollock TM (2015) A study of microstructure-driven strain localizations in two-phase polycrystalline HCP/BCC composites using a multi-scale model. Int J Plast 74: 35-57

73. Knezevic M, Daymond MR and Beyerlein IJ (2016) Modeling discrete twin lamellae in a microstructural framework. Scr Mater 121: 84-88

74. Wang S, Zhuang W, Cao J and Lin J (2010) An investigation of springback scatter in forming ultra-thin metal-sheet channel parts using crystal plasticity FE analysis. The International Journal of Advanced Manufacturing Technology 47: 845-852

75. Zhuang W, Wang S, Cao J, Lin J and Hartl C (2010) Modelling of localised thinning features in the hydroforming of micro-tubes using the crystal-plasticity FE method. The International Journal of Advanced Manufacturing Technology 47: 859-865

76. Cubit https://cubit.sandia.gov/

77. Asaro RJ and Needleman A (1985) Texture development and strain hardening in rate dependent polycrystals. Acta Metall Mater 33: 923-953

78. Hutchinson JW (1976) Bounds and self-consistent estimates for creep of polycrystalline materials. Proceedings of the Royal Society of London Series A, Mathematical and Physical Sciences 348: 101-126

79. Zecevic M, Beyerlein IJ, McCabe RJ, McWilliams BA and Knezevic M (2016) Transitioning rate sensitivities across multiple length scales: Microstructure-property relationships in the Taylor cylinder impact test on zirconium. Int J Plast 84: 138-159

80. Kocks U, Argon A and Ashby M (1975) Progress in materials science. Thermodynamics and Kinetics of Slip 19: 110-170

81. Beyerlein IJ and Tomé CN (2008) A dislocation-based constitutive law for pure Zr including temperature effects. Int J Plast 24: 867-895

82. Madec R, Devincre B, Kubin L, Hoc T and Rodney D (2003) The role of collinear interaction in dislocation-induced hardening. Science 301: 1879-1882

83. Knezevic M, Carpenter JS, Lovato ML and McCabe RJ (2014) Deformation behavior of the cobalt-based superalloy Haynes 25: Experimental characterization and crystal plasticity modeling. Acta Mater 63: 162-168

84. Knezevic M, McCabe RJ, Tomé CN, Lebensohn RA, Chen SR, Cady CM, Gray Iii GT and Mihaila B (2013) Modeling mechanical response and texture evolution of α-uranium as a function of strain rate and temperature using polycrystal plasticity. Int J Plast 43: 70-84

85. Zecevic M, Knezevic M, Beyerlein IJ and McCabe RJ (2016) Texture formation in orthorhombic alpha-uranium under simple compression and rolling to high strains. Journal of Nuclear Materials 473: 143-156

86. Knezevic M, Zecevic M, Beyerlein IJ, Bingert JF and McCabe RJ (2015) Strain rate and temperature effects on the selection of primary and secondary slip and twinning systems in HCP Zr. Acta Mater 88: 55-73

87. Mecking H and Kocks UF (1981) Kinetics of flow and strain-hardening. Acta Metall Mater 29: 1865-1875

88. Madec R, Devincre B and Kubin LP (2002) From Dislocation Junctions to Forest Hardening. Physical Review Letters 89: 255508

89. Eghtesad A and Knezevic M (2020) High-performance full-field crystal plasticity with dislocation-based hardening and slip system back-stress laws: Application to modeling deformation of dual-phase steels. J Mech Phys Solids 134: 103750

90. Lavrentev FF (1980) The type of dislocation interaction as the factor determining work hardening. Materials Science and Engineering 46: 191-208

91. Essmann U and Mughrabi H (1979) Annihilation of dislocations during tensile and cyclic deformation and limits of dislocation densities. Philosophical Magazine A 40: 731-756

92. Mughrabi H (1987) A two-parameter description of heterogeneous dislocation distributions in deformed metal crystals. Materials science and engineering 85: 15-31

93. Jackson PJ (1985) Dislocation modelling of shear in f.c.c. crystals. Prog Mater Sci 29: 139-175

94. Wang Z, Beyerlein I and LeSar R (2007) The importance of cross-slip in high-rate deformation. Modelling and Simulation in Materials Science and Engineering 15: 675

95. Peeters B, Bacroix B, Teodosiu C, Van Houtte P and Aernoudt E (2001) Work-hardening/softening behaviour of b.c.c. polycrystals during changing strain paths: II. TEM observations of dislocation sheets in an IF steel during two-stage strain paths and their representation in terms of dislocation densities. Acta Mater 49: 1621-1632

96. Kocks UF and Mecking H (2003) Physics and phenomenology of strain hardening: the FCC case. Prog Mater Sci 48: 171-273

97. Owen SJ, Brown JA, Ernst CD, Lim H and Long KN (2017) Hexahedral mesh generation for computational materials modeling. Procedia engineering 203: 167-179

98. Owen SJ, Staten ML and Sorensen MC (2011) Parallel hex meshing from volume fractions Proceedings of the 20th International Meshing Roundtable Springer, pp 161-178

99. Allen SM and Cahn JW (1979) A microscopic theory for antiphase boundary motion and its application to antiphase domain coarsening. Acta Metall 27: 1085-1095

100. Abdeljawad F and Foiles SM (2015) Stabilization of nanocrystalline alloys via grain boundary segregation: a diffuse interface model. Acta Mater 101: 159-171

101. Abdeljawad F, Völker B, Davis R, McMeeking RM and Haataja M (2014) Connecting microstructural coarsening processes to electrochemical performance in solid oxide fuel cells: An integrated modeling approach. Journal of Power Sources 250: 319-331

102. Ardeljan M, Beyerlein IJ and Knezevic M (2017) Effect of dislocation density-twin interactions on twin growth in AZ31 as revealed by explicit crystal plasticity finite element modeling. Int J Plast 99: 81-101

103. Ardeljan M and Knezevic M (2018) Explicit modeling of double twinning in AZ31 using crystal plasticity finite elements for predicting the mechanical fields for twin variant selection and fracture analyses. Acta Mater 157: 339-354

104. (2013) Patran Version 2013, MSC Software Corporation, Newport Beach, CA, USA.

105. (2017) ABAQUS Version 6, Dassault Systèmes, Providence, RI, USA.

Chapter 2: Mechanical response, twinning, and texture evolution of WE43 magnesium-rare earth alloy as a function of strain rate: Experiments and multi-level crystal plasticity modeling

This chapter was published as: Feather, William G., Saeede Ghorbanpour, Daniel J. Savage, Milan Ardeljan, Mohammad Jahedi, Brandon A. McWilliams, Nikhil Gupta, Chongchen Xiang, Sven C. Vogel, and Marko Knezevic. "Mechanical response, twinning, and texture evolution of WE43 magnesium-rare earth alloy as a function of strain rate: experiments and multi-level crystal plasticity modeling." *International Journal of Plasticity* 120 (2019): 180-204.

My contribution to this work was in the calibration of the crystal plasticity model for the alloy WE43 and computational analysis. I prepared all the figures associated with computational modeling. As part of this calibration and figure preparation, I created automation scripts to improve the workflow's efficiency. The text was written in a standard student-mentor relationship.

Mechanical response, twinning, and texture evolution of WE43 magnesium-rare earth alloy as a function of strain rate: Experiments and multi-level crystal plasticity modeling

William G. Feather [a], Saeede Ghorbanpour [a], Daniel J. Savage [a], Milan Ardeljan [a], Mohammad Jahedi [a], Brandon A. McWilliams [b], Nikhil Gupta [c], Chongchen Xiang [c], Sven C. Vogel [d], and Marko Knezevic [a,2]

[a] Department of Mechanical Engineering, University of New Hampshire, Durham, NH 03824, USA.

[b] Weapons and Materials Research Directorate, US Army Research Laboratory, Aberdeen Proving Ground, MD 21005, USA.

[c] Mechanical and Aerospace Engineering, New York University, Brooklyn, NY 11201, USA.

[d] Los Alamos Neutron Science Center, Los Alamos National Laboratory, Los Alamos, NM, USA.

Abstract

This work adapts a recently developed multi-level constitutive model for polycrystalline metals that deform by a combination of elasticity, crystallographic slip, and deformation twinning to interpret the deformation behavior of alloy WE43 as a function of strain rate. The model involves a two-level homogenization scheme. First, to relate the grain level to the level of a

[2] Corresponding author at: Department of Mechanical Engineering, University of New Hampshire, 33 Academic Way, Kingsbury Hall, W119, Durham, NH 03824, USA. Tel.: +1 603 862 5179; fax: +1 603 862 1865.
E-mail address: marko.knezevic@unh.edu (M. Knezevic).

polycrystalline aggregate, a Taylor-type model is used. Second, to relate the aggregate level response at each finite element (FE) integration point to the macro-level, an implicit FE approach is employed. The model features a dislocation-based hardening law governing the activation stress at the slip and twin system level, taking into account the effects of temperature and strain rate through thermally-activated recovery, dislocation debris formation, and slip-twin interactions. The twinning model employs a composite grain approach for multiple twin variants and considers double twinning. The alloy is tested in simple compression and tension at a quasi-static deformation rate and in compression under high strain rates at room temperature. Microstructure evolution of the alloy is characterized using electron backscattered diffraction and neutron diffraction. Taking the measured initial texture as inputs, it is shown that the model successfully captures mechanical responses, twinning, and texture evolution using a single set of hardening parameters, which are associated with the thermally activated rate law for dislocation density across strain rates. The model internally adjusts relative amounts of active deformation modes based on evolution of slip and twin resistances during the imposed loadings to predict the deformation characteristics. We observe that WE43 exhibits much higher strain-hardening rates under high strain rate deformation than under quasi-static deformation. The observation is rationalized as primarily originating from the pronounced activation of twins and especially contraction and double twins during high strain rate deformation. These twins are effective in strain hardening of the alloy through the texture and barrier hardening effects.

Keywords: A. Microstructures; A. Twinning; B. Crystal plasticity; B. Anisotropic material; C. Finite elements; T-CPFE UMAT

6. Introduction

Magnesium (Mg) alloys containing rare earth (RE) elements have been developed to increase ductility and strength while reducing the plastic anisotropy and tension vs. compression asymmetry in comparison to common Mg alloys such as AZ31 (Bhattacharyya et al., 2016; Cho et al., 2009; Hidalgo-Manrique et al., 2017; Jahedi et al., 2018a; Jahedi et al., 2018b; Jiang et al., 2016). Asymmetry refers to the difference in the mechanical response between tension vs. compression, while anisotropy is more generic and refers to a property being directionally dependent, which implies different properties in different directions, as opposed to isotropy. The major underlying mechanisms responsible for these improvements are related to precipitates, which influence the ratio between the activation stress for basal, prismatic, and pyramidal slip modes. As a result, slip systems belonging to these slip modes can simultaneously activate. Moreover, reduced twinning activity reduces tension vs. compression asymmetry and propensity to strain localization. Finally, texture in these alloys is moderately strong causing small anisotropy in mechanical behavior (Al-Samman and Li, 2011; Bohlen et al., 2007; Hadorn et al., 2012; Hantzsche et al., 2010; Imandoust et al., 2017; Sandlöbes et al., 2014; Stanford and Barnett, 2008). According to ASTM (2011; King, 2007), in the WE Mg alloy series W stands for Yttrium (Y) and E stands for rare earth (RE) elements such as Neodymium (Nd), which influences age hardening and strength at elevated temperatures (Avedesian and Baker, 1999; Li et al., 2007). The alloy WE43 is based on the Mg-Y-Nd system (Nie, 2012); and amongst the WE series, WE43 alloy shows high static and fatigue strength, creep resistance, corrosion resistance, and flame resistance (Castellani et al., 2011; Gavras et al., 2016; Ghorbanpour et al., 2019a, b; Li et al., 2010; Mengucci et al., 2008; Nie and Muddle, 2000; Nie et al., 2001).

Various crystal plasticity-based models have been developed and used to model the constitutive response of metals and alloys. These models have proven to be successful especially for low symmetry crystal structure metals such as Mg alloys with hexagonal close-packed (HCP) structure which exhibit pronounced anisotropy and asymmetry in their mechanical response. In crystal plasticity models, the homogenization relationships relating the deformation of the constituent crystal to that of the polycrystalline aggregate can be achieved using mean-field and full-field theories. In either case, activation of deformation models (i.e. slip and twinning modes) is governed by a hardening model, which describes their resistance to activation. The former class of models (Kalidindi, 1998; Knezevic et al., 2009; Knezevic et al., 2014a; Knezevic et al., 2008; Knezevic and Landry, 2015; Lebensohn and Tomé, 1993; Taylor, 1938; Van Houtte, 1988; Wu et al., 2007; Zecevic and Knezevic, 2018; Zecevic et al., 2015; Zecevic et al., 2016c; Zecevic et al., 2018b, 2019; Zecevic et al., 2017b) have often been used due to their computational efficiency and ease of implementation. These are commonly referred to as Taylor-type and self-consistent-type models. However, explicit grain-to-grain interactions are not considered by these models. The latter class of models (Abdolvand et al., 2015; Fernández et al., 2013; Jahedi et al., 2015; Keshavarz and Ghosh, 2015; Lebensohn et al., 2012; Staroselsky and Anand, 2003) accounts for grain-to-grain interactions and, as a result, better resolves local mechanical fields arising from the explicit grain structure. These models include the crystal plasticity finite element (CPFE) models and Green's function fast Fourier transform crystal plasticity models (Eghtesad et al., 2018; Lebensohn et al., 2012).

Modeling deformation twinning in the plasticity models for Mg alloys is vital. Modeling discrete twins and the growing domains of reoriented crystal lattice orientation accommodating the plastic strain using spatially resolved models have been attempted only recently (Ardeljan et al.,

2017; Ardeljan and Knezevic, 2018; Ardeljan et al., 2015; Cheng et al., 2018; Kumar et al., 2015). However, these models have yet to be advanced to model the formation, propagation, and growth of twin domains in a practical way. In contrast, several micromechanical approaches have been developed to incorporate the reorientation and shear due to twinning in mean-field models: the predominant twin reorientation approach (Jain and Agnew, 2007; Tomé et al., 1991; Tomé et al., 2001; Van Houtte, 1978; Wang et al., 2010), total Lagrangian approach (Kalidindi, 1998; Wu et al., 2007), and composite-grain (CG) approach (Knezevic et al., 2013a; Proust et al., 2007; Tomé and Kaschner, 2005). Here, deformation twinning is considered as pseudo-slip (Kalidindi, 1998; Van Houtte, 1978) followed by reorientation and volume transfer from a parent grain containing a twin to the independent twin grain.

In the present work, the full-field finite element and Taylor-type crystal plasticity models are combined (T-CPFE), where the first level of meso-scale homogenization is performed using the Taylor model, while the second level of macro-scale homogenization is performed using crystal plasticity finite elements. The second level of the homogenization is relaxing the intrinsic assumption of the Taylor model pertaining to the iso deformation gradient or iso velocity gradient applied over a polycrystal. Thus, every constituent grain experiences the same applied deformation. The applied deformation varies spatially over finite elements but is the same for all grains embedded per FE integration point. A polycrystalline material is split over a number of FE integration points interrogating a subset of grains belonging to the sub-polycrystal. The overall FE homogenization is over many Taylor-type models running at FE integration points. The added advantage of the T-CPFE model over the Taylor-type homogenization is that it can simulate geometrical changes. The T-CPFE model is similar to the FE-VPSC (visco-plastic self-consistent) (Knezevic et al., 2014c; Knezevic et al., 2013b; Knezevic et al., 2013c; Zecevic et al.,

2016b) and FE-EPSC (elasto-plastic self-consistent) (Zecevic et al., 2017a) formulations since both approaches embed a sub-polycrystal at every FE integration point. The latter models rely on the self-consistent (SC) homogenization of individual grains, while the T-CPFE model embeds the Taylor-type homogenization. In general, the SC approach is more accurate and versatile but is slower than T-CPFE because of the SC iterations. Therefore, typically the number of grains embedded at each FE integration point is smaller for FE-VPSC/FE-EPSC than in T-CPFE. The individual grains deform by crystallographic slip and deformation twinning. The CG formulation (Proust et al., 2007) within the total Lagrangian numerical scheme of the T-CPFE model is used for handling twinning, where multiple twin variants per grain are allowed. Every variant is a new grain undergoing the Taylor-type homogenization per FE integration point. A recently developed dislocation density (DD) hardening law is used for evolving the slip/twin resistances (Beyerlein and Tomé, 2008). The T-CPFE modeling approach integrating the sub-crystalline scale and the scale of the sample operating concurrently, has been successfully applied to AZ31 (Ardeljan et al., 2016a) and is adapted here to alloy WE43. An EPSC model for predicting the mechanical behavior of the alloy WE43 has been proposed in (Bhattacharyya et al., 2016); and while the model successfully captured strain hardening evolution of the material as a function of testing direction using a set of material parameters at a given strain rate, it did not consider secondary or double twinning. As a result, the origins of strain hardening across strain rates, which are in the core of the present paper, have not been described.

Mechanical response of the alloy is measured in simple compression and tension under a quasi-static deformation rate and in compression under high strain rates at room temperature. The testing results are presented here along with texture and twinning evolution of the alloy. These are characterized using electron backscattered diffraction (EBSD) and neutron diffraction.

Taking the measured initial texture and average grain size data as inputs, it is shown that the model successfully captures across strain rates the mechanical responses, twinning, and texture evolution of the alloy using a single set of hardening parameters associated with the DD hardening law. The complete set of material hardening parameters for the law for the WE43 alloy is established. The model internally adjusts relative amounts of active deformation modes based on the evolution of slip and twin resistances during the imposed loadings to predict the deformation characteristics. The predictions show that the deformation is accommodated by a combination of multiple slip and twinning modes governing the flow stress and texture evolution. It is seen that WE43 exhibits much higher strain-hardening rates under high strain rate deformation then under quasi-static deformation. The observation is rationalized here to originate from the pronounced activation of twinning and especially contraction and double twinning during high strain rate deformation. These twins are effective in strain hardening of the alloy through the texture and barrier effects.

7. Material and experiments

Alloy WE43 used in the present study has been supplied by Magnesium Elektron North America (Madison, IL) in the form of a plate. The alloy had a nominal composition of 3.7-4.3 wt.% Y, 2.4-4.4 wt.% RE (Nd), at least 0.4 wt.% Zr, and Mg (balance). The material was supplied in the T5 condition.

7.1 Mechanical tests

Cylinders for compression tests were cut employing the wire electric discharge machining (EDM) method to a diameter of 8 mm and a height of 10 mm. The compression tests were performed at room temperature using an Instron Model # 1350 machine having a load cell

capacity of 100 kN equipped with the DAX software and controller (Gribbin et al., 2016; Gribbin et al., 2019). The strain rate for all compression tests was 10^{-3} s^{-1} and the tests continued until a prescribed strain value was achieved or sample failure occurred. Tensile bars were machined per ASTM E8 (2015) as dog-bones having their gauge section of 25 mm in length and a 3×6 mm cross-section. Monotonic tensile tests were performed using an MTS biaxial servo-hydraulic machine with Flextest software and controller. The capacity of the machine is 250 kN. During the tests, an MTS 623.12E-24 extensometer was used to measure sample elongation. The displacement data from the extensometer was used in the analysis. All the tensile tests were performed at room temperature and the nominal strain rate was 10^{-3} s^{-1}. The tests were either interrupted or continued until the specimens broke. All tension and compression tests were repeated at least three times to ensure the accuracy and repeatability of the data. The variation in the data was less than 2%. The orientations of the tension specimens were RD and TD, while the orientations of the compression specimens were RD, TD, and ND with respect to the rolled plate frame. The high strain rate (HSR) compression testing was carried out using an in-house developed split-Hopkinson pressure bar setup. Inconel incident and transmitter bars of 12.7 mm in diameter and 1800 in mm length were used during testing. These Inconel alloy bars have Young's modulus and density of 195 GPa and 8190 kg/m^3, respectively. Specimens of 5 mm in diameter and 5 mm in length were tested to obtain material response in the strain rate range 1000 and 2500 s^{-1}.The strain pulses were recorded from the incident and the transmitter bars using strain gauges. True stresses were calculated at the front surface of the specimen that is in contact with the incident bar and the back surface of the specimen that is in contact with the transmitter bar to determine stress equilibrium in the specimen during testing (Xiang et al., 2018). The average value of strain rate in the HSR region is presented as the nominal strain rate for a given

test. These tests were also performed either to prescribed strain levels or until sample failure. The orientation of the HSR specimens was TD with respect to the rolled plate frame.

7.2 Microstructural characterization

Initial and deformed microstructures of the studied alloy are characterized by EBSD technique in a scanning electron microscope (SEM). Additionally, texture evolution was measured by neutron diffraction. Prior to the EBSD mapping, the samples were prepared using a Buehler EcoMet 3 polishing machine. A series of SiC grinding papers with different grit size ranging from 120 to 1200 were used to grind the specimens. After grinding an etchant comprising of 60 Vol. % ethanol, 20 Vol. % distilled water, 15 Vol.% acetic acid, and 5 Vol. % of nitric acid was applied for 5 seconds to reveal the microstructure. A Tescan Lyra (Ga) field emission SEM with the Pegasus system (Octane Plus SDD detector and Hikari High-Speed Camera) was used for the EBSD data collection at a voltage of 25 kV. Neutron diffraction was performed on the initial materials and pre-deformed samples using the High Pressure Preferred Orientation (HIPPO) neutron time-of-flight diffractometer at the Los Alamos Neutron Science Center at Los Alamos National Laboratory (LANL) (Vogel et al., 2004; Wenk et al., 2003). Unlike EBSD, neutron diffraction provides a bulk measurement of specimen texture.

Deformation twinning was characterized by EBSD. Since many grains appear to be nearly consumed by twins at large strains, boundary length fraction and twin analysis software that assumes the parent to be larger than the twin are not appropriate. Twin area fractions were identified using the methodology described in (Jain and Agnew, 2007), which assumes that reorientation toward the loading direction is accommodated strictly by tensile twinning. In similar fashion to (Bhattacharyya et al., 2016), we have used the average area fraction obtained with a 30-40° misorientation cutoff around the loading direction. To verify the validity of this

methodology, we utilize the sign of the Schmid factor on the twinning plane as discussed in (Marshall et al., 2010) to identify the parent and twin grain fragments for type one tensile twinning. Agreement within a few percent is observed in all cases when the initial area fraction of grains aligned with the loading direction were subtracted from the deformed area fractions. The estimates are accurate to about 3% error tolerance.

8. Summary of the modeling framework

A multi-level T-CPFE model linking grain, polycrystalline aggregate, and macro-scale properties is adapted and utilized here to predict and interpret the deformation behavior of alloy WE43. The FE framework is at the highest length scale and the integration point constitutive response is a Taylor-type polycrystalline model wherein the response of individual grains is driven by slip and twinning. The overall model is a User MATerial (UMAT) subroutine in Abaqus. While the FE level satisfies compatibility and equilibrium, the polycrystalline Taylor model level fulfills only the compatibility between the constituent grains. Upon imposing boundary conditions over an FE mesh, a deformation gradient, $\mathbf{F}$, is available at each FE integration point at previous, t, and current, $t+\Delta t$, time increments. Additionally, the Cauchy stress, $\boldsymbol{\sigma}^t$, is available for each grain along with the set of state variables for each grain, twin volume fraction for each active variant, and dislocation density for slip systems per grain at the previous increment, t. T-CPFE calculates stress in each grain and then the volume average Cauchy stresses, $\overline{\boldsymbol{\sigma}}$, and Jacobian for the FE solver as well as the updated state variables at trial $t+\Delta t$. Upon convergence, the current solution is accepted and the calculation advances.

The average Cauchy stress over K constituent crystal orientations embedded at a given integration point is

$$\bar{\boldsymbol{\sigma}} = \sum_{k=1}^{K} \vartheta_k \boldsymbol{\sigma}_k. \quad (1)$$

The total number of orientations consists of weighted (ϑ) parent grains and active twin variants. These orientations at a given FE integration point undergo a deformation gradient, **F**, available at that integration point.

Like in any other crystal plasticity model, a set of potential slip and twinning systems are input into the model. For WE43, these are basal **a** $\{0001\}\langle\bar{1}\bar{1}20\rangle$, prismatic **a** $\{\bar{1}100\}\langle\bar{1}\bar{1}20\rangle$, pyramidal **a** $\{\bar{1}101\}\langle\bar{1}\bar{1}20\rangle$, and pyramidal **c**+**a** $\{10\bar{1}1\}\langle11\bar{2}\bar{3}\rangle$ or type I and $\{\bar{1}\bar{1}22\}\langle11\bar{2}3\rangle$ or type II slip systems and **c**-axis extension twin 1 $\{10\bar{1}2\}\langle\bar{1}011\rangle$ (TTW 1), **c**-axis extension twin 2 $\{11\bar{2}1\}\langle\bar{1}\bar{1}26\rangle$ (TTW 2), **c**-axis contraction twin $\{10\bar{1}1\}\langle10\bar{1}\bar{2}\rangle$ (CTW), and double twin $\{10\bar{1}1\}-\{10\bar{1}2\}$ (DTW). The TTW 1 produces a shear strain of 0.1289, while reorienting the crystal lattice orientation by approximately 86^o about the $\langle11\bar{2}0\rangle$ direction. The TTW 2 has a much larger shear of 0.6158 and reorients the crystal lattice orientation by approximately 34^o about the $\langle10\bar{1}0\rangle$ direction. The CTW has a shear of 0.1377 with the reorientation of approximately 56^o about the same $\langle11\bar{2}0\rangle$ direction (Yoo, 1981). In pure Mg and Mg alloys like AZ31, the TTW are fast growing and morphologically thick (Al-Samman and Gottstein, 2008; Barnett, 2007a). In contrast, the CTW are morphologically thin and much harder to observe (Al-Samman and Gottstein, 2008; Barnett, 2007b; Knezevic et al., 2010). The morphology of CTW has been rationalized to be due to the formation of an extension twin within the contraction twin lamella shortly upon its formation hindering its growth. The sequence is called DTW. The DTW variants are classified into four types based on the misorientation angles of the common zone axis between the basal planes of the parent grain. Type 1 (e.g. $(0\bar{1}11)[0\bar{1}1\bar{2}]-(0\bar{1}12)[01\bar{1}1]$) has the angle of 37.5° and type 2 (e.g. $(0\bar{1}11)[0\bar{1}1\bar{2}]-(01\bar{1}2)[0\bar{1}11]$) has the angle of 30.1°.

The hardening law evolves slip and twin resistances and as a result, adjusts relative amounts of active deformation modes.

In the description that follows, superscripts *s* and *t* are used to denote slip and twin systems, respectively, while superscripts α and β are used to denote slip and twin modes (families). In the crystal plasticity theory used in present work, an applied velocity gradient tensor, **L**, is first additively decomposed to its elastic and plastic parts, $\mathbf{L}^e$ and $\mathbf{L}^p$, respectively, and then the plastic part is further decomposed to account for both the slip and twinning kinematics

$$\mathbf{L} = \mathbf{L}^e + \mathbf{L}^p = \mathbf{L}^e + \mathbf{L}^{sl} + \mathbf{L}^{tw} = \mathbf{L}^e + \sum_s^{N^{sl}} \dot{\gamma}^s \mathbf{b}_0^s \otimes \mathbf{n}_0^s + \sum_t^{N^{tw}} \dot{f}^t S^t \mathbf{b}_0^t \otimes \mathbf{n}_0^t. \quad (2)$$

In Eq. (2), $\mathbf{b}_0^s$, $\mathbf{b}_0^t$, $\mathbf{n}_0^s$, and $\mathbf{n}_0^t$ are time independent unite vectors for the slip and twin Burgers directions and plane normals at the reference configuration, $\dot{\gamma}^s$ is the shear rate, S^t is the intrinsic twin shear strain, and $\dot{f}^t = \frac{\dot{\gamma}^t}{S^t}$ is the twin volume fraction rate computed based on the pseudo slip model (Kalidindi, 1998; Van Houtte, 1978). The number of available slip and twin systems are denoted by N^{sl} and N^{tw}, respectively.

In contrast to the additive decomposition of applied **L**, the decomposition of the applied deformation gradient, **F**, is multiplicative to its elastic and plastic parts

$$\mathbf{F} = \mathbf{F}^e \mathbf{F}^p. \quad (3)$$

Next, the rate of change of the plastic part is

$$\dot{\mathbf{F}}^p = \mathbf{L}^p \mathbf{F}^p, \quad (4)$$

which after the integration from *t* to *t*+Δt is

$$\mathbf{F}^p(\tau) = exp(\mathbf{L}^p \Delta t)\mathbf{F}^p(t). \quad (5)$$

Completing the theory requires defining a stress-strain relationship, which in the present model is as follows

$$\mathbf{T}^e = \mathbf{C}\mathbf{E}^e,\ \mathbf{T}^e = \mathbf{F}^{e^{-1}}\{(det\mathbf{F}^e)\boldsymbol{\sigma}\}\mathbf{F}^{e^{-T}},\ \mathbf{E}^e = \frac{1}{2}\{\mathbf{F}^{e^T}\mathbf{F}^e - \mathbf{I}\}. \quad (6)$$

In Eq. (6), $\mathbf{C}$ is the elastic stiffness, $\mathbf{T}^e$ is the second Piola-Kirchhoff stress, and $\mathbf{E}^e$ is the Lagrangian strain. To evaluate the stress, $\mathbf{F}^e$ is calculated using $\mathbf{F}^e = \mathbf{F}\mathbf{F}^{p^{-1}} = \mathbf{F}\mathbf{F}^{p^{-1}}(t)\{\mathbf{I} - \Delta t\mathbf{L}^p\}$.

The shear strain rates for slip and twinning, $\dot{\gamma}^s$ and $\dot{\gamma}^t$, are governed by the power-law relationship (Asaro and Needleman, 1985; Hutchinson, 1976; Kalidindi, 1998):

$$\dot{\gamma}^s = \dot{\gamma}_0 \left(\frac{|\tau^s|}{\tau_c^s(\dot{\varepsilon},T)}\right)^{\frac{1}{m}} \mathrm{sign}(\tau^s)\ . \quad (7)$$

In Eq. (7), τ^s is the resolved shear stress for slip calculated using $\tau^s = \mathbf{T}^e \cdot \mathbf{m}_0^s = \mathbf{T}^e \cdot \mathbf{b}_0^s \otimes \mathbf{n}_0^s$, τ_c^s is the slip systems resistance, $\mathbf{m}_0^s$ is the Schmid tensor, $\dot{\gamma}_0$ is the reference slip rate, and m is the rate sensitivity (m = 0.02). The reference shear rate is set equal to the norm of the applied velocity gradient, $\dot{\gamma}_0 = \dot{\varepsilon} = |\mathbf{L}|$ to realize the applied strain rate independence. Thus, the power-law exponent ensures proper selection of slip and twin systems but does not introduce any extraneous strain rate sensitivity, which is recognized as a potential issue when simulating high strain rate deformation using power-law visco-plasticity (Knezevic et al., 2016; Zecevic et al., 2016a). Note that the origin of the strain rate-sensitivity in the present model is solely in the evolution of the activation stresses which are a result of microstructure evolution, as will be described shortly. Similar to slip, expressions exist for twinning like the Schmid tensors for a twin variant is $\mathbf{m}_0^t = \mathbf{b}_0^t \otimes \mathbf{n}_0^t$ and the driving stress is $\tau^t = \mathbf{T}^e \cdot \mathbf{m}_0^t$.

The resistance to slip and twinning evolves with plastic strain, temperature, and strain rate as microstructural features such as dislocation density evolve. Sensitivity to temperature will be studied in future works. To account for these, we utilize the dislocation density-based hardening law originally developed in (Beyerlein and Tomé, 2008) and later advanced in (Ardeljan et al., 2016a; Knezevic et al., 2015). In this law, the overall resistance to slip includes

$$\tau_{\mathrm{c}}^{\mathrm{s}}(\dot{\varepsilon},T)=\tau_{0}^{\alpha}+\tau_{\mathrm{HP}}^{\mathrm{s}}+\tau_{\mathrm{for}}^{\mathrm{s}}(\dot{\varepsilon},T)+\tau_{\mathrm{sub}}^{\alpha}(\dot{\varepsilon},T), \tag{8}$$

where τ_0^s is an initial value of the friction stress for the undeformed material, τ_{HP}^s is the first evolving contribution to the slip resistance which is the barrier term due to twinning since the grain size effects are embedded into τ_0^s, τ_{for}^s is evolving with the forest dislocation density, and τ_{sub}^{α} is evolving with the substructure (debris) dislocation density.

The second term is derived from the Hall-Petch relationship as

$$\tau_{HP}^{s}=\mu^{\alpha}H_{i}^{\alpha}\sqrt{\frac{b^{\alpha}}{d_{mfp}^{s}}}, \tag{9}$$

where b^{α} is the Burgers vector magnitude per slip mode α, μ^{α} is the shear modulus, and H_i^{α} are the Hall-Petch-like coefficients for grains containing lamellas of TTW 1 and 2 (i=1), CTW (i=2), and DTW (i=3). Finally, d_{mfp}^{s} is the mean-free-path between adjacent twins per grain and is calculated using (Beyerlein and Tomé, 2008; Proust et al., 2007)

$$d_{mfp}^{s}=\frac{(1-f^{pts})d_{c}}{\sin(\theta)}. \tag{10}$$

In Eq. (10), f^{pts} is the volume fraction of predominant twin system (PTS), θ is the angle made up of the slip and twin system planes, and d_c is the twin spacing defined as the ratio between the

grain size, d_g, and the number of lamellae. While multiple twin variants can form per grain, we still rely on the PTS concept for estimating d^s_{mfp}.

The terms $\tau^s_{for}(\dot{\varepsilon},T)$ and $\tau^\alpha_{sub}(\dot{\varepsilon},T)$ are governed by the corresponding dislocation densities $\rho^s_{for}(\dot{\varepsilon},T)$ and $\rho_{sub}(\dot{\varepsilon},T)$ (Madec et al., 2002; Mecking and Kocks, 1981)

$$\tau^s_{for} = b^\alpha \mu^\alpha \sqrt{\chi^{ss'}\rho^{s'}_{for}},\ \tau^\alpha_{sub} = k_{sub}\mu^\alpha b^\alpha \sqrt{\rho_{sub}}\, log\left(\frac{1}{b^\alpha\sqrt{\rho_{sub}}}\right). \tag{11}$$

In Eq. (11), $\chi^{ss'}$ is a dislocation interaction matrix with the diagonal terms (*s*=*s'*) set to a typical value of 0.81, the off-diagonal terms set to zero (Mecking and Kocks, 1981), and $k_{sub} = 0.086$ (Madec et al., 2002).

The forest dislocation density is governed by the rate of generation and removal by annihilation (Essmann and Mughrabi, 1979; Mecking and Kocks, 1981):

$$\frac{\partial\rho^s_{for}}{\partial\gamma^{s'}} = \frac{\partial\rho^s_{gen,for}}{\partial\gamma^{s'}} - \frac{\partial\rho^s_{rem,for}}{\partial\gamma^{s'}} = k^\alpha_1\sqrt{\rho^s_{for}} - k^s_2(\dot{\varepsilon},T)\rho^s_{for}, \quad \Delta\rho^s_{for} = \frac{\partial\rho^s_{for}}{\partial\gamma^{s'}}|\Delta\gamma^s|, \tag{12}$$

where k^α_1 and $k^\alpha_2(\dot{\varepsilon},T)$ are coefficients for dislocation storage and dynamic recovery, respectively. The latter is derived following the work in (Beyerlein and Tomé, 2008)

$$\frac{k^\alpha_1}{k^s_2(\dot{\varepsilon},T)} = \frac{1}{\sqrt{\left(\chi^{s's}\right)^{-1}\left(\frac{\tau^\alpha_{sat}}{b^\alpha\mu^\alpha}\right)^2}},\ \tau^\alpha_{sat} = \frac{D^\alpha(b^\alpha)^3 g^\alpha\mu^\alpha}{\left(D^\alpha(b^\alpha)^3 - kTln\left(\frac{\dot{\varepsilon}}{\dot{\varepsilon}_0}\right)\right)}, \tag{13}$$

where k, $\dot{\varepsilon}_0$, g^α, and D^α are Boltzmann's constant, the reference value of strain rate (10^7 s^{-1}), the activation enthalpy, and the drag stress. This strain rate and temperature sensitive Kocks-Mecking type hardening model intrinsically suppresses dynamic recovery at higher strain rates increasing the rate of strain hardening. Finally, debris dislocation density is incremented using

$$\Delta\rho_{sub} = \sum_s q^{\alpha} b^{\alpha} \sqrt{\rho_{sub}} \frac{\partial \rho^s_{rem,for}}{\partial \gamma^{s'}} \left|\Delta\gamma^{s'}\right|, \quad (14)$$

where q^{α} is a coefficient defining the amount of debris from the recovered dislocation population.

The resistance to twin has the following form

$$\tau^t_c(\dot{\varepsilon}, T) = \tau^{\beta}_0 + \tau^{\beta}_{0,HP} + \tau^t_{slip}(\dot{\varepsilon}, T). \quad (15)$$

The first term is the friction term

$$\tau^{\beta}_0 = \tau^{\beta}_{\text{prop}} + \left(\tau^{\beta}_{crit} - \tau^{\beta}_{\text{prop}}\right) exp\left(-\sum \frac{\rho^s_{for}}{\rho^s_{sat}}\right), \quad (16)$$

which incorporates the nucleation and propagation stresses, τ^{β}_{crit} and τ^{β}_{prop}, weighted by the probability term, $\rho^s_{sat} = \left(\frac{k^{\alpha}_1}{k^s_2}\right)^2$, to favor τ^{β}_{crit} initially and τ^{β}_{prop} subsequently during deformation (Beyerlein and Tomé, 2008). The second term is the Hall-Petch-like term

$$\tau^{\beta}_{0,HP} = \frac{H^{\beta}_0}{\sqrt{d_{mfp}}}, \quad (17)$$

and the last term is the hardening due to the slip-twin interactions

$$\tau^t_{slip} = \mu^{\beta} \sum_{\alpha} C^{\alpha\beta}(\dot{\varepsilon}) b^{\beta} b^{\alpha} \rho^{\alpha}_{for}. \quad (18)$$

The interaction matrix $C^{\beta\alpha}(\dot{\varepsilon})$ is sensitive to strain rate meaning that the strength of the slip-twin interactions varies with strain rates. Twins form more profusely and are often morphologically thinner under higher strain rate deformation conditions (Song and Gray, 1995). These morphological features in conjunction with the increased number of dislocation sources under higher strain rate deformation influences the slip-twin interactions. The lattice reorientation due

to twinning is handled using the CG model (Proust et al., 2007). The original model was advanced to consider multiple twin variants per grain and to consider secondary and double twins. The variants nucleate when their fraction f^t achieves a critical value of a distribution centered at 2 % and grow by volume fraction transferring from the parent grain to the variants. Upon nucleation, the variants inherit the slip/twin resistances and dislocation densities from the parent grain. The sum of volume fractions of the parent and variants originating from the same parent remains constant but the number of grains per FE integration points increases for the number of twin variants created at that integration point.

Crystal lattice orientation of the twinned domains is harder than the parent grain relative to the loading direction thereby inducing hardening (Asgari et al., 1997; Knezevic and Beyerlein, 2018; Knezevic et al., 2012). Hardening due to reorientation can be significant if the pyramidal slip model that activates in the twinned domain is much harder than the other deformation modes like in AZ31 (Clausen et al., 2008; Jain and Agnew, 2007; Lentz et al., 2015; Lou et al., 2007; Proust et al., 2009; Risse et al., 2017). Next, twins subdivide a parent grain inducing the Hall-Petch-like hardening (Asgari et al., 1997; Bouvier et al., 2012; Kaschner et al., 2007; Proust et al., 2007). For extension twins, this type of hardening is small because they grow quickly and dislocations can readily be transmitted (Molodov et al., 2017). However, contraction twins are known to induce a significant Hall-Petch-like hardening (Knezevic et al., 2010). Finally, the Basinski-type hardening could arise through the transmutations of dislocations from the parent to the twin (Basinski et al., 1997). For this mechanism of hardening, a certain level of dislocation density in grains is necessary. Because twins develop early in plastic deformation of Mg, the Basinski-type hardening is not significant; especially at lower levels of plastic strain (El Kadiri and Oppedal, 2010).

9. Results

In this section, data sets for WE43 used to calibrate and validate the T-CPFE model are presented first followed by the modeling results. The data and modeling results are then used to elucidate the role of various slip and twinning systems and their interactions in deformation of WE43 as a function of strain rate.

9.1 Experimental

The measured tensile and compressive true stress-true strain response under a quasi-static strain rate and true stress-true strain response under high strain rates of WE43 are shown in Fig. 1. Multiple samples were deformed to fracture to verify repeatability of the results. The flow stress curves measured under high strain rate deformation were similar for the tested range of rates. The level of variation of strain rate per dynamic test is provided in the appendix A. It can be seen that WE43 shows predominantly decreasing strain hardening rates in quasi-static tension and compression, which is unusual for Mg alloys like AZ31. Only a small inflection portion of the work hardening rate is present for the compressive curves, which is a consequence of more twinning activity in compression then in tension. While initial yield stress is seen as approximately insensitive to the strain rate, the hardening rate, after small plastic strain, is greater at higher strain rates. The material exhibits small anisotropy and asymmetry in its response. These are attributed to the deformation modes accommodating the imposed deformation.

The map in Fig. 2 shows the initial (undeformed) microstructure revealing nearly equiaxed grain structure with an approximate mean grain size of $d_g = 25\ \mu m$. Initial texture is moderately strong with the crystallographic **c**-axis aligned with the normal direction (ND) and tilted more

towards the rolling direction (RD) than towards the transverse direction (TD). Maps of deformed material in compression under quasi-static and high strain rates are shown in Figs. 3 and 4, respectively. Appendix A presents maps of the material deformed in simple tension showing that the extension twinning TTW 1 primarily activates during tension but much less than in compression. Additionally, a minor content of CTW and DTW can be seen. Change in the color as a function of strain indicated crystal reorientation during deformation. TTW 1 domains are red in the maps. Twins are highlighted in the maps by the twin vs. matrix boundary relationship within 5 degrees of the reflection about the twinning plane normal. The boundaries are identified in the magnified 'blank' maps by different colors. TTW 1 appears to be the favored twin in WE43, like in many Mg alloys such as AZ31. These twins grow fast with plastic deformation encompassing entire parent grains. However, TTW 2 as another **c**-axis extension twin is also present, which is unusual for alloys of Mg (Jahedi et al., 2017). Nevertheless, it has been observed in some highly alloyed alloys of Mg (Eckelmeyer and Hertzberg, 1970; Stanford, 2008; Stanford et al., 2015). While no substantial activity of CTW and DTW is found under in-plane quasi-static deformation in compression, these twins are active under high strain rate deformation. Appendix A compares image quality maps of samples deformed to fracture (~0.18 strain) under quasi-static compression and 2250 s-1 in TD. A large fraction of the dark bands in the IQ map are believed to be contraction/double twins. As is evident, there is much less of the double twin lamellae in the material deformed under quasi-static compression then high strain rate deformation along the TD axis. The twin analysis suggests that double twinning is much more rate-sensitive than extension twinning. The volume fractions of the contraction and double twins is approximately 1 – 2 % in the samples deformed under the quasi-static deformation and approximately 5% for the samples deformed under high strain deformation, as estimated using

the EBSD analysis. Appendix A also shows maps for the material deformed in compression along ND and tension along TD. These maps also reveal the occurrence of extension twins in a larger amount than contraction and double twins; even though the later twins are expected to activate considering the texture of the material in a larger amount during contraction along ND, whether in ND compression or in-plane tension. Thus, the activity of contraction and double twins is more pronounced under high strain rate deformation than under any quasi-static deformation. The origin of the higher hardening rate in the high strain rate relative to the quasi-static deformation is in the difference in deformation twinning activity, twinning modes, and slip-twin interactions. EBSD maps show that more deformation is accommodated by twinning under high strain rate then quasi-static compression. Quantitative analysis of twinning based on multiple maps is performed here and the results will be presented later. Figure 5 correlates the axis angle disorientation with grain boundary axis-angle textures for all grain boundaries after compression along TD at quasi-static and high strain rates. Figure 5 highlights the important shift in the grain boundaries fractions at high and low strain rates. The microstructure after quasi-static compression in TD contains a large number of extension twin boundaries with a small fraction of contraction and double twins after a high amount of plastic strain. In contrast, the microstructure after high strain rate deformation contains a much larger fraction of contraction and especially double twin boundaries after the same amount of plastic strain. The data is based on evaluating multiple large EBSD scans. Texture of deformed material will be presented later along with the predictions of T-CPFE. The effect of the deformation mechanisms and, in particular, twinning on the mechanical response and texture evolution of WE43 will be interpreted using the model.

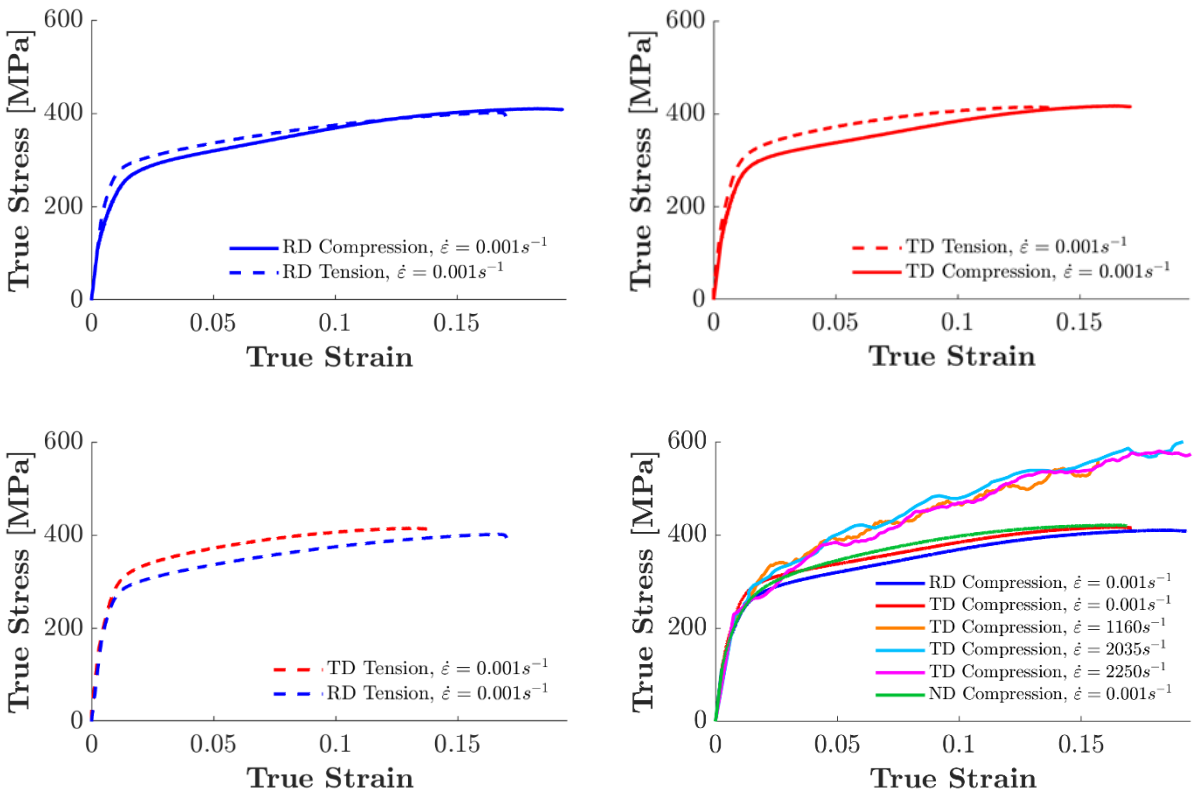

Fig. 1. *Measured true stress-true strain response in simple tension, simple compression, and split-Hopkinson pressure bar (SHPB) compression on samples of WE43 along the directions and strain rates indicated in the plots. The quasi-static curves are repeated two times to facilitate the comparisons.*

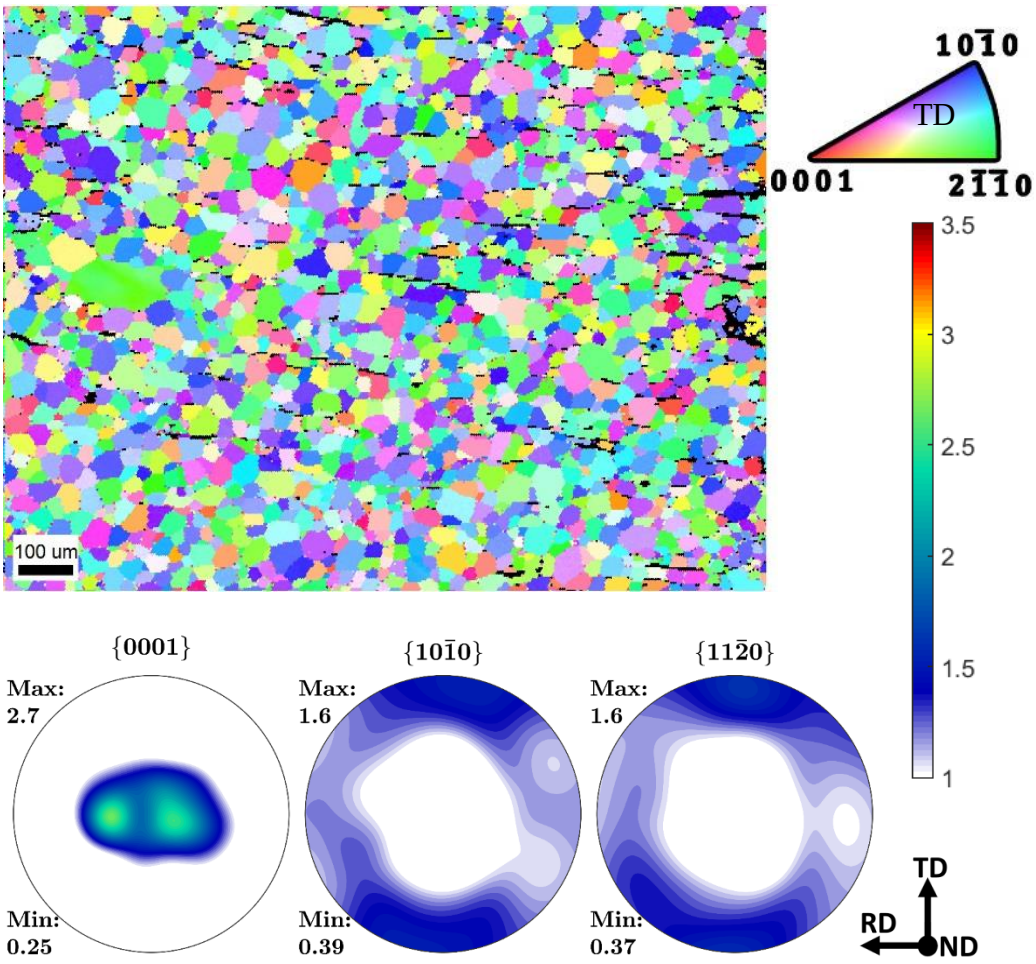

***Fig. 2**. EBSD inverse pole figure map and neutron diffraction stereographic pole figures showing initial microstructure and texture in the as-received sample of WE43. The sample direction perpendicular to the map is TD. The colors in the maps represent the orientation of the TD sample axis with respect to the local crystal lattice frame according to the unit triangle.*

(a)

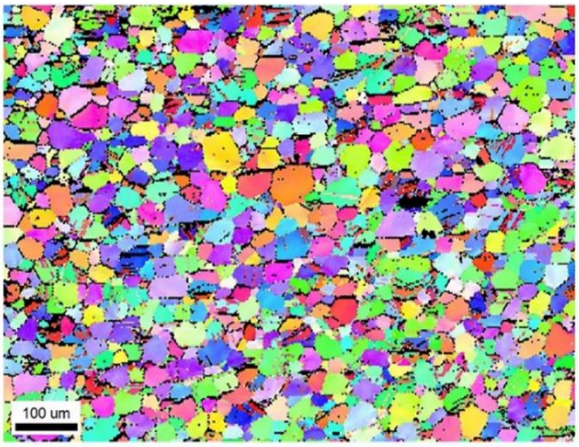

(b)

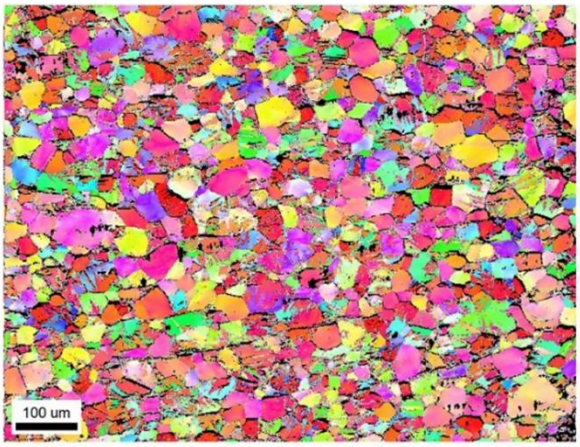

(c)

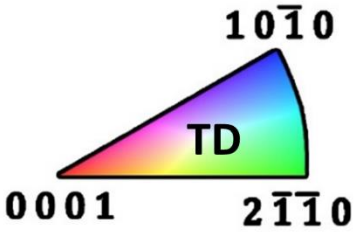

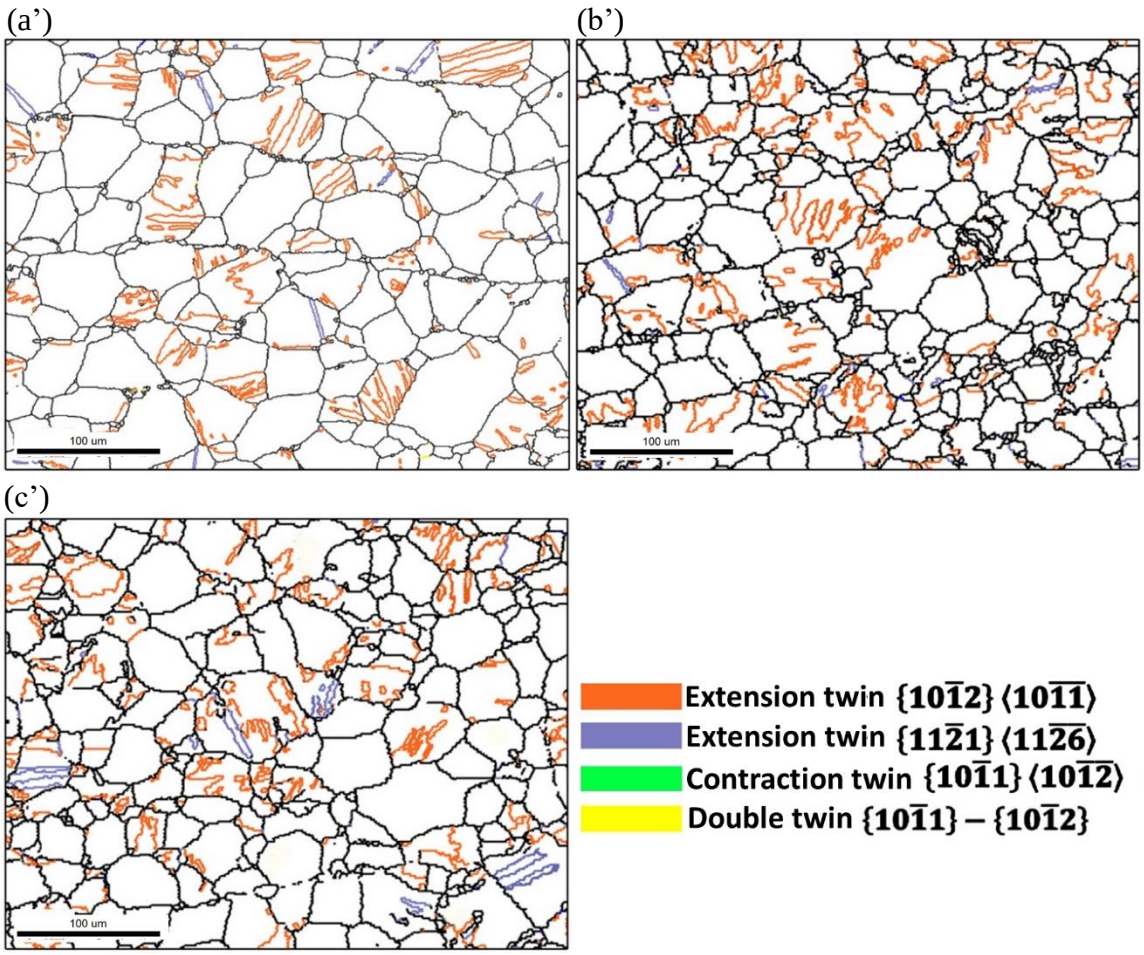

***Fig. 3**. EBSD inverse pole figure maps showing microstructure in the pre-compressed samples along TD under 0.001 s^{-1} strain rate at room temperature to true strain levels of (a) 0.06, (b) 0.1, and (c) fracture. The compression direction is perpendicular to the maps. The colors in the maps (a), (b), and (c) represent the orientation of the compression axis with respect to the local crystal lattice frame according to the IPF triangle. The corresponding blank maps (a'), (b'), and (c') highlight twin boundaries for the four twinning modes identified in the maps with a different color as specified in the legend based on the expected twin-parent relationships (a reflection about the twinning plane normal).*

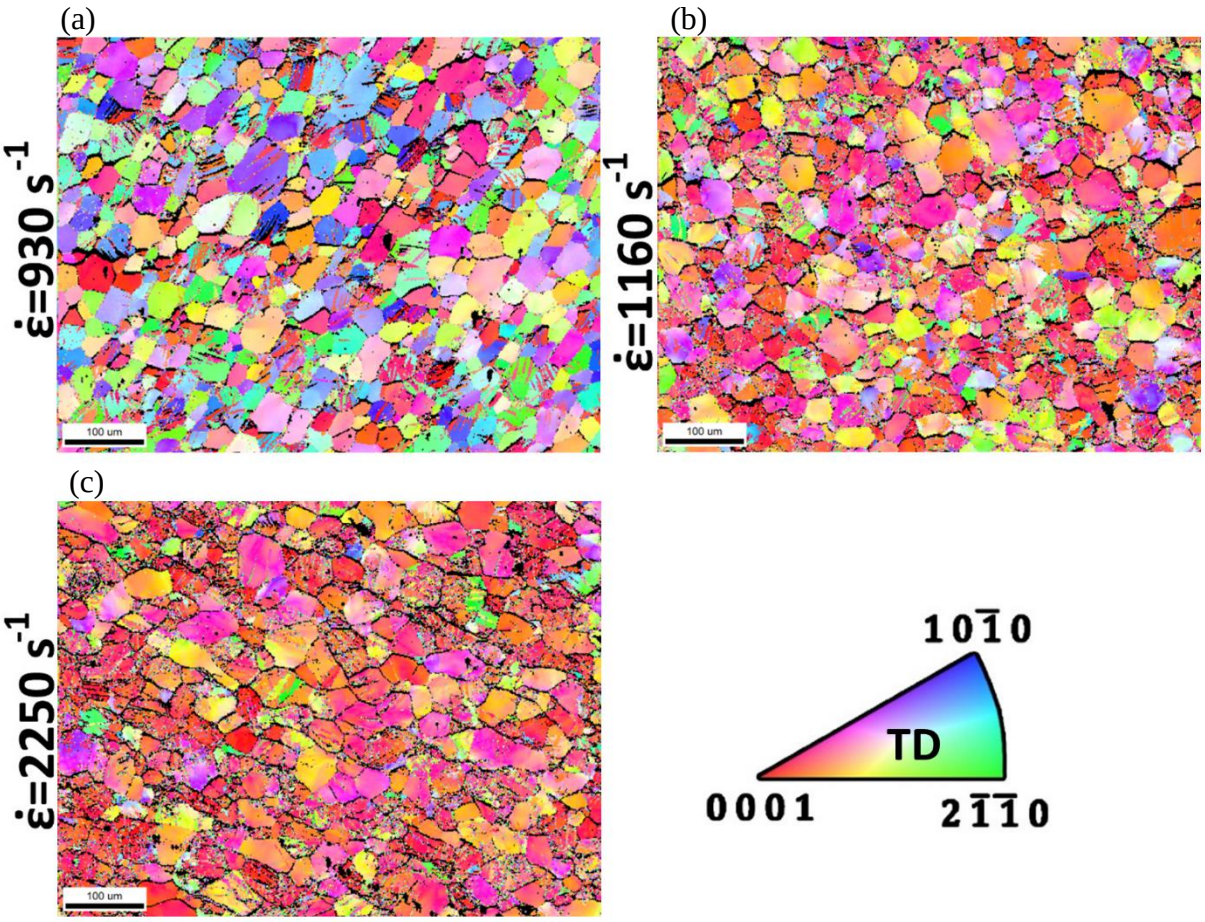
(a)
(b)
(c)
$\dot{\varepsilon}$=930 s^{-1}
$\dot{\varepsilon}$=1160 s^{-1}
$\dot{\varepsilon}$=2250 s^{-1}
100 um
100 um
100 um
$10\bar{1}0$
TD
0001
$2\bar{1}\bar{1}0$

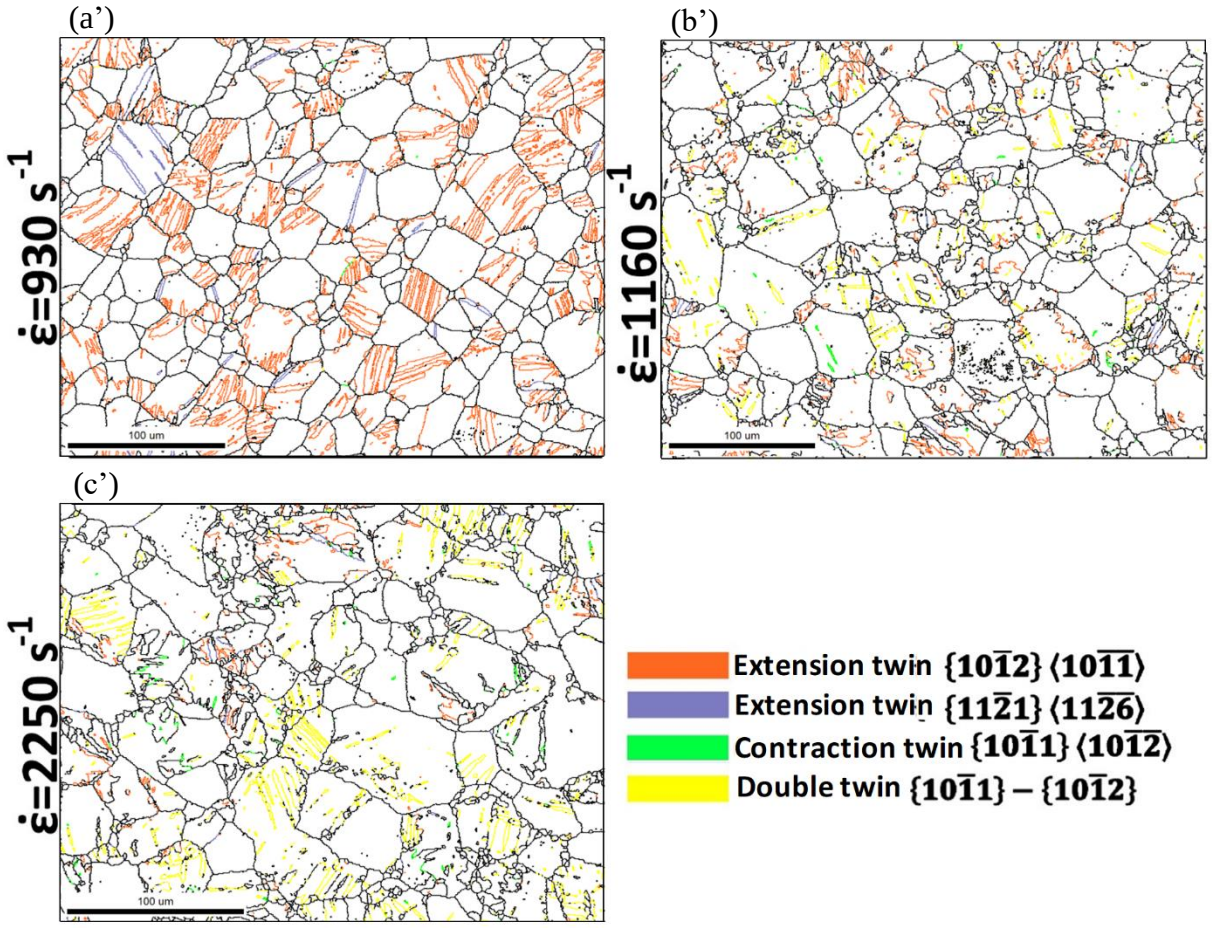

Fig. 4*. EBSD inverse pole figure maps showing microstructure in the pre-compressed samples along TD under high strain rates indicated in the figure at room temperature to true strain levels of (a) 0.06, (b) 0.1, and (c) fracture. The compression direction is perpendicular to the maps. The colors in the maps (a), (b), and (c) represent the orientation of the compression axis with respect to the local crystal lattice frame according to the IPF triangle. The corresponding blank maps (a'), (b'), and (c') highlight twin boundaries for the four twinning modes identified in the maps with a different color as specified in the legend based on the expected twin-parent relationships (a reflection about the twinning plane normal).*

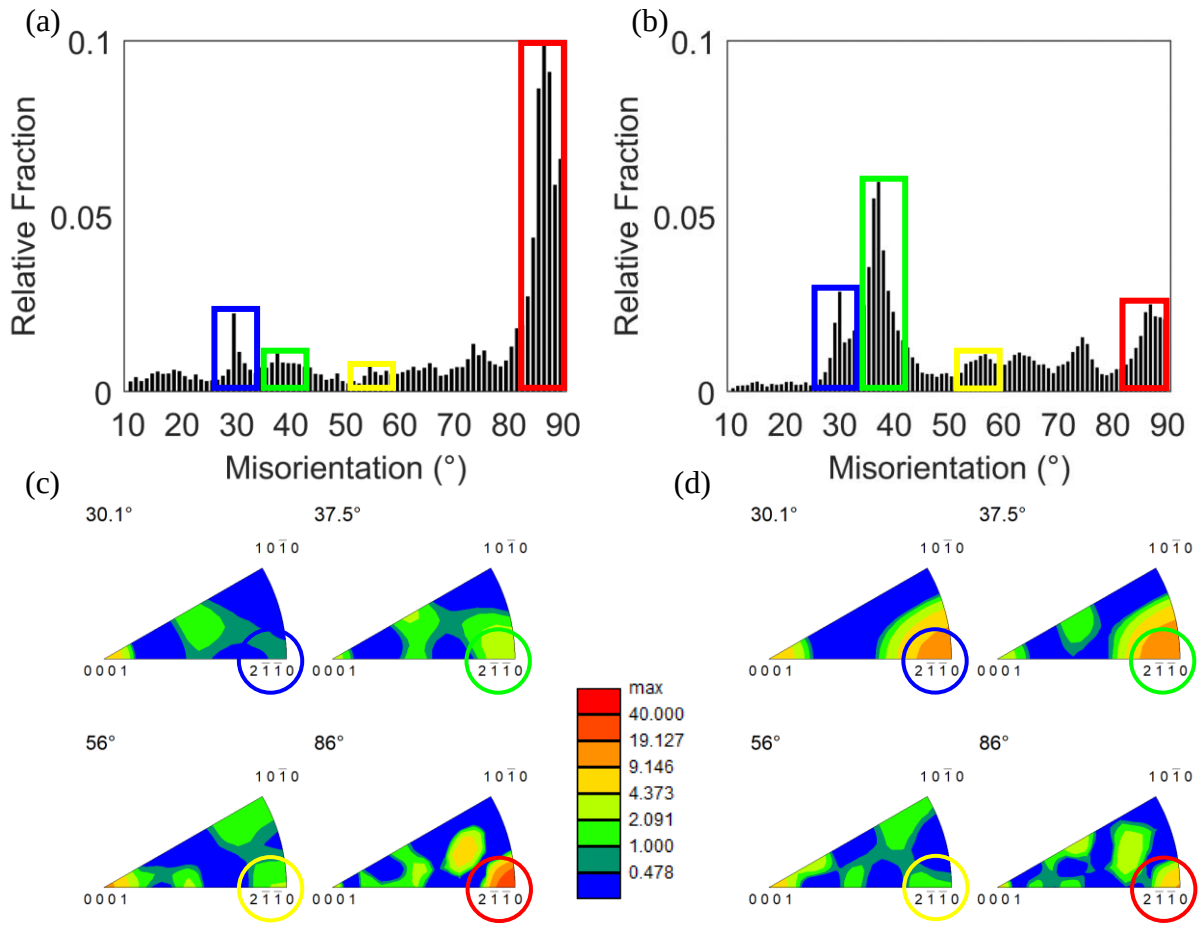

Fig. 5*. Axis-angle disorientation (a, b) and correlated grain boundary axis-angle textures (c, d) between identified grains for compression along TD at strain rates of (a, c) 0.001 s^{-1} and (b, d) 2250 s^{-1} at the same true strain level of approximately 0.18. TTW 1 = red, CTW = yellow, type 1 DTW = green, and type 2 DTW=blue.*

9.2 Modeling

The simple tension and compression of polycrystalline WE43 are simulated as a function of strain rate using the T-CPFE model. In particular, the evolution of texture and twinning along with the underlying predictions of active deformation mechanisms are predicted by the model. The prediction of relative activity of slip and twinning systems contributing to the plasticity of each grain during deformation is a benefit of the model. The latter predictions are governed by the evolution of the slip and twin resistance of the modes. The resistances are determined by the hardening law, which is driven by a reliable set of hardening parameters. The set of parameters pertaining to the hardening law within T-CPFE for WE43 will be presented shortly. These are

established to capture the mechanical data as a function of strain rate, as presented in the previous section. The relative activity of deformation modes governs the evolution of texture and flow stress.

The model is initialized with the texture measured using neutron diffraction (Fig. 2), which is represented using 3,072 weighted crystal orientations. The texture represented using these orientations will be referred to as initial simulated texture. These were assigned to integration points of a finite element model used to simulate simple tension and compression tests (Fig. 1). The FE model is a cubic cell consisting of 64 eight node, full integration, three-dimensional continuum elements (C3D8). The cell is used for establishing the hardening parameters (i.e. the model calibration) and model verification. Every FE integration point contains 6 weighted crystal orientations (8 integration points per element * 64 elements * 6 orientations = 3,072) and every grain is allowed to develop multiple twin variants. Thus, the number of grains rapidly increases at each FE material point with deformation. As already explained, the response at each material point is obtained using the Taylor-type homogenization model. The latter is interrogated using the imposed strain i.e. strain rate based on FE model boundary conditions, which are consistent with the experimental tests. These were imposed as displacements along the loading axis with the stress free conditions on the sides (Jahedi et al., 2015). The FE model relaxes the Taylor-model iso-strain rate constraint and provides the overall response. The multi-level model is used to interpret the deformation behavior of WE43 by identifying the underlying slip/twin mechanisms responsible for its hardening behavior over a range of strain rates. The experimental data in terms of flow stress, texture, and twin volume fractions is also presented in this paper. Three experimental flow curves are used for model calibration. These are the tensile and compressive RD curves under the quasi-static deformation and the compressive TD curve at a

strain rate of 2250 s^{-1}. The tensile and compressive TD curves under quasi-static deformation and the compressive TD curve at a strain rate of 1160 s^{-1} are used for model verification and modeling results for these curves can be regarded as predictions. The goal is to reproduce the experimental data in terms of flow curves, texture evolution, and twin volume fractions with a single set of hardening material constants.

Figure 6 compares the measured and calculated flow stress responses of WE43 for seven tests and presents one prediction test (ND under 1160 s^{-1}). The only change to the FE model from test to test is the prescribed loading direction and strain rate. As is evident, the model successfully reproduces the effect of strain rate on the hardening behavior of WE43 using the single set of hardening parameters. The established hardening parameters are given in Tables 1 and 2 for slip and twinning, respectively. On the basis of density functional theory (DFT) calculations (Kumar et al., 2017) and our earlier work (Zecevic et al., 2018a), we assume that the initial slip resistance values for pyramidal II and I has a ratio of 1.07. The parameters are demonstrated to be reliable by reproducing a number of flow curves constraining the model. Thus, the same initial texture and material parameters are used in every simulation. In particular, the high hardening rate under the high strain rate deformation is well captured, which is a consequence of slip/twin activity. The activities of underlying deformation mechanisms associated with each test are predicted by the model and are also shown in the figure. The decrease in hardening rates with plastic strain exhibited by the flow curves suggests the slip dominated deformation. However, deformation twins activate and the comparison between measured and predicted activity is shown in the figure. Some anisotropy and tension vs. compression asymmetry in the mechanical response develop, which is attributed to twinning and texture evolution. More twinning activates during

high strain rate deformation and, in particular, much more CTW and DTW activate during high strain rate deformation.

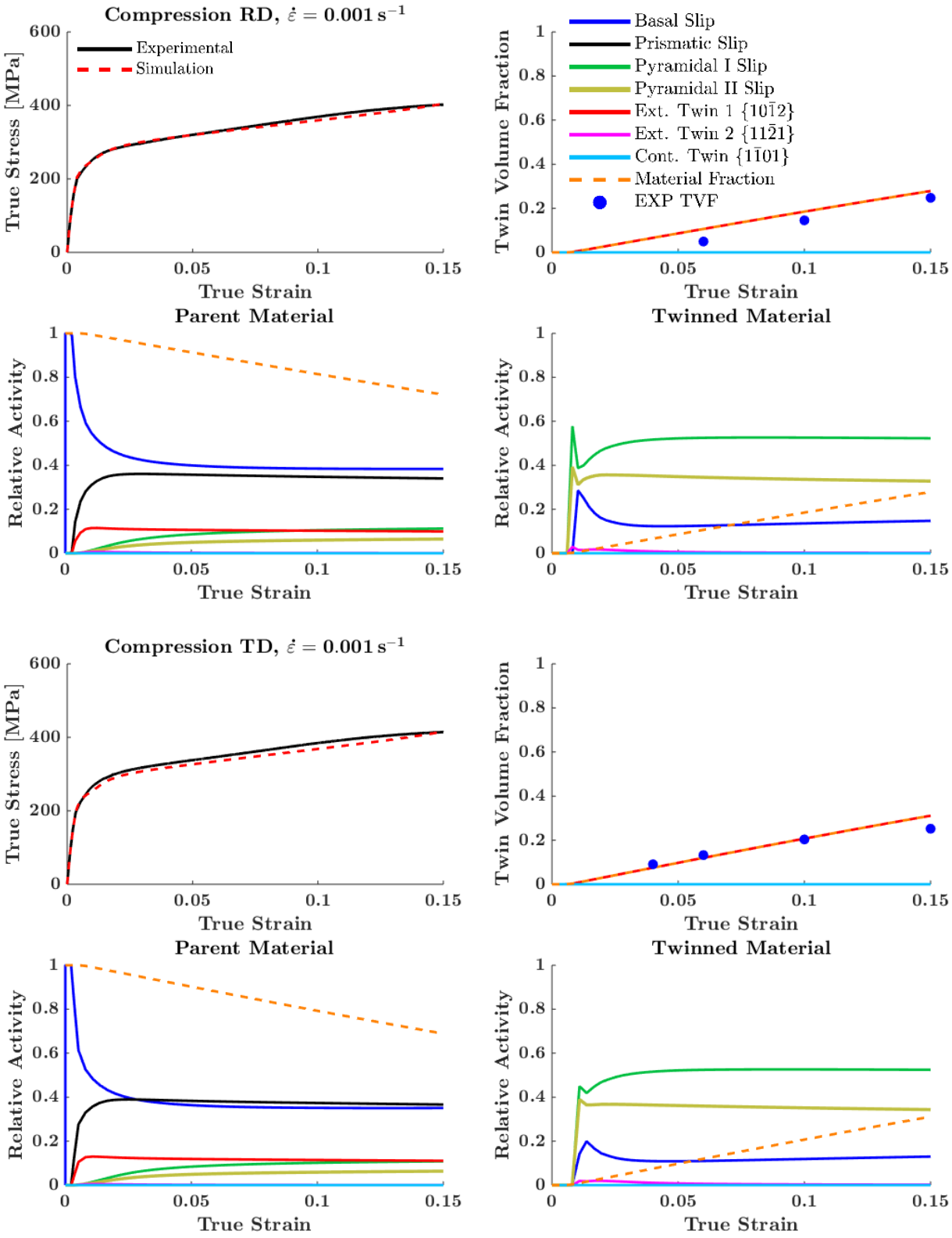
Compression RD, $\dot{\varepsilon} = 0.001\,\mathrm{s}^{-1}$
Experimental
Simulation
True Stress [MPa]
True Strain
Basal Slip
Prismatic Slip
Pyramidal I Slip
Pyramidal II Slip
Ext. Twin 1 $\{10\bar{1}2\}$
Ext. Twin 2 $\{11\bar{2}1\}$
Cont. Twin $\{1\bar{1}01\}$
Material Fraction
EXP TVF
Twin Volume Fraction
Parent Material
Twinned Material
Relative Activity
Compression TD, $\dot{\varepsilon} = 0.001\,\mathrm{s}^{-1}$

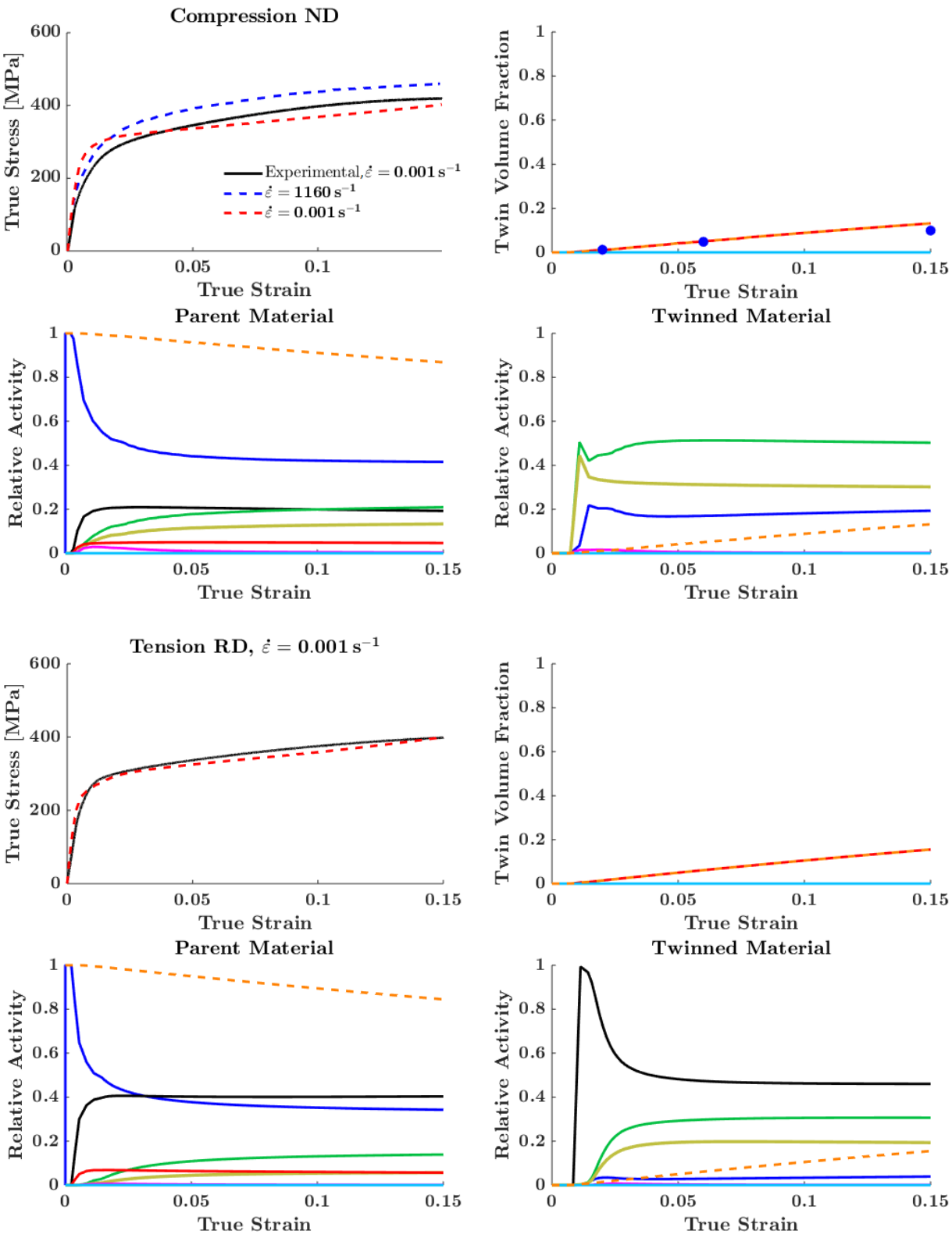
Compression ND
True Stress [MPa]
True Strain
Experimental, $\dot{\varepsilon} = 0.001\,s^{-1}$
$\dot{\varepsilon} = 1160\,s^{-1}$
$\dot{\varepsilon} = 0.001\,s^{-1}$
Twin Volume Fraction
Parent Material
Twinned Material
Relative Activity
Tension RD, $\dot{\varepsilon} = 0.001\,s^{-1}$

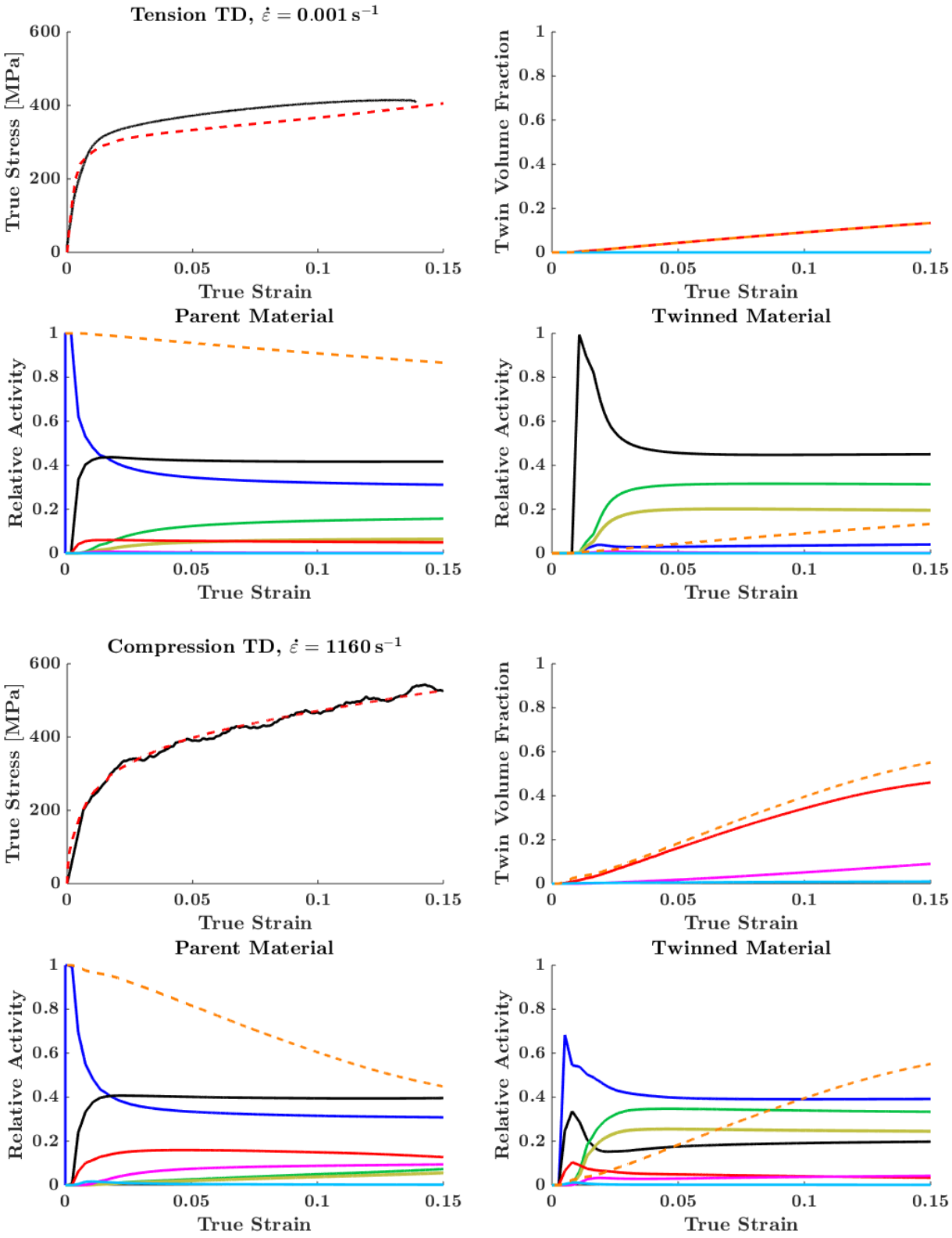
Tension TD, $\dot{\varepsilon} = 0.001\,\mathrm{s}^{-1}$
True Stress [MPa]
True Strain
Twin Volume Fraction
Parent Material
Twinned Material
Relative Activity
Compression TD, $\dot{\varepsilon} = 1160\,\mathrm{s}^{-1}$

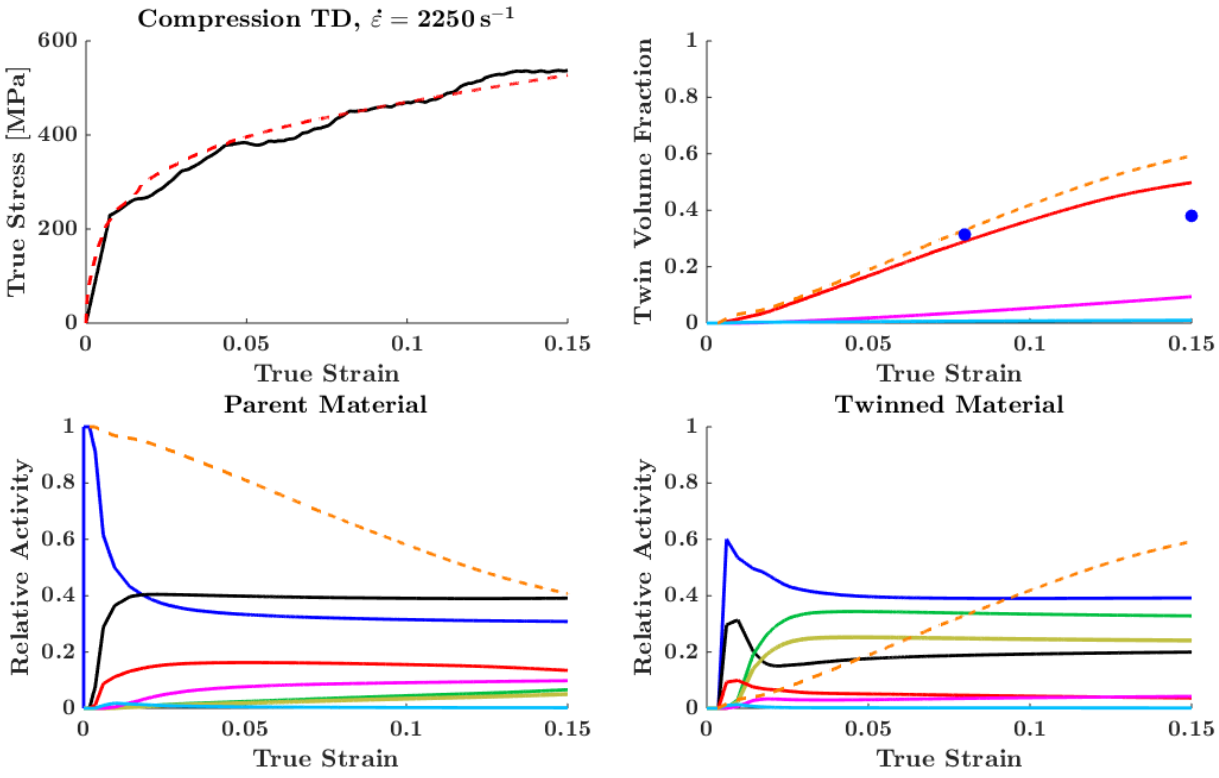

Fig. 6*. Comparison of measured and calculated true stress-true strain responses in simple tension and compression for samples of WE43 alloy as a function of strain rate along the directions as indicated in the figure along with predicted relative activities of each deformation mode contributing to plasticity in both the parent grains and the twinned domains. Plotted is also the parent and twinned material volume fraction. The activity plots for compression along ND are given for the simulation under quasi-static strain rate.*

Figures 7 - 9 show side by side comparison between measured and predicted texture evolution in RD, TD, and ND respectively. These predictions further validate the model. As is evident, the model calculations of texture during tension and compression are in good agreement with the neutron and EBSD measurements of texture for the studied range of strain rates. These predictions also confirm that the twinning activity is predicted well because texture evolution and twinning are intrinsically coupled. The prefered texture components are qualitatively captured in both tension and compression. The change in texture during compression is more prominently observed in basal poles where the re-alignment can be seen. Grains before compression oriented with their **c**-axis parallel with ND and tilted towards RD reorient such that their **c**-axis aligns with the compression direction with a pronounced tilt in TD for the RD

compression. Interestingly, the pole figures depict gradual reorientation of texture, which is a consequence of the cooperative action of slip and twinning, as opposed to a sudden change in texture due to profuse twinning like in AZ31. The activity of basal slip and extension twinning are known to be bringing the **c**-axis parallel to the compression direction (Ardeljan et al., 2016b; Carpenter et al., 2015). The comparison between texture evolution in compression under quasi-static and high strain rate deformation indicated faster evolution of the latter then the former. Texture during the ND compression is not evolving substantially since most of the grains were initially oriented with their **c**-axis parallel or slightly tilted with respect to the compression direction. Pyramidal slip is here more active than in compression along RD and TD. Activity of pyramidal slip in combination with basal and prismatic slip involved more at the early stage of deformation is concentrating crystallographic **c**-axis around the ND direction. Twinning is also active during quasi-static compression along ND but not as much as during the compression along in-plane directions. As a result, the basal fiber texture strengthens, which is evident from the pole figures in Fig. 9.

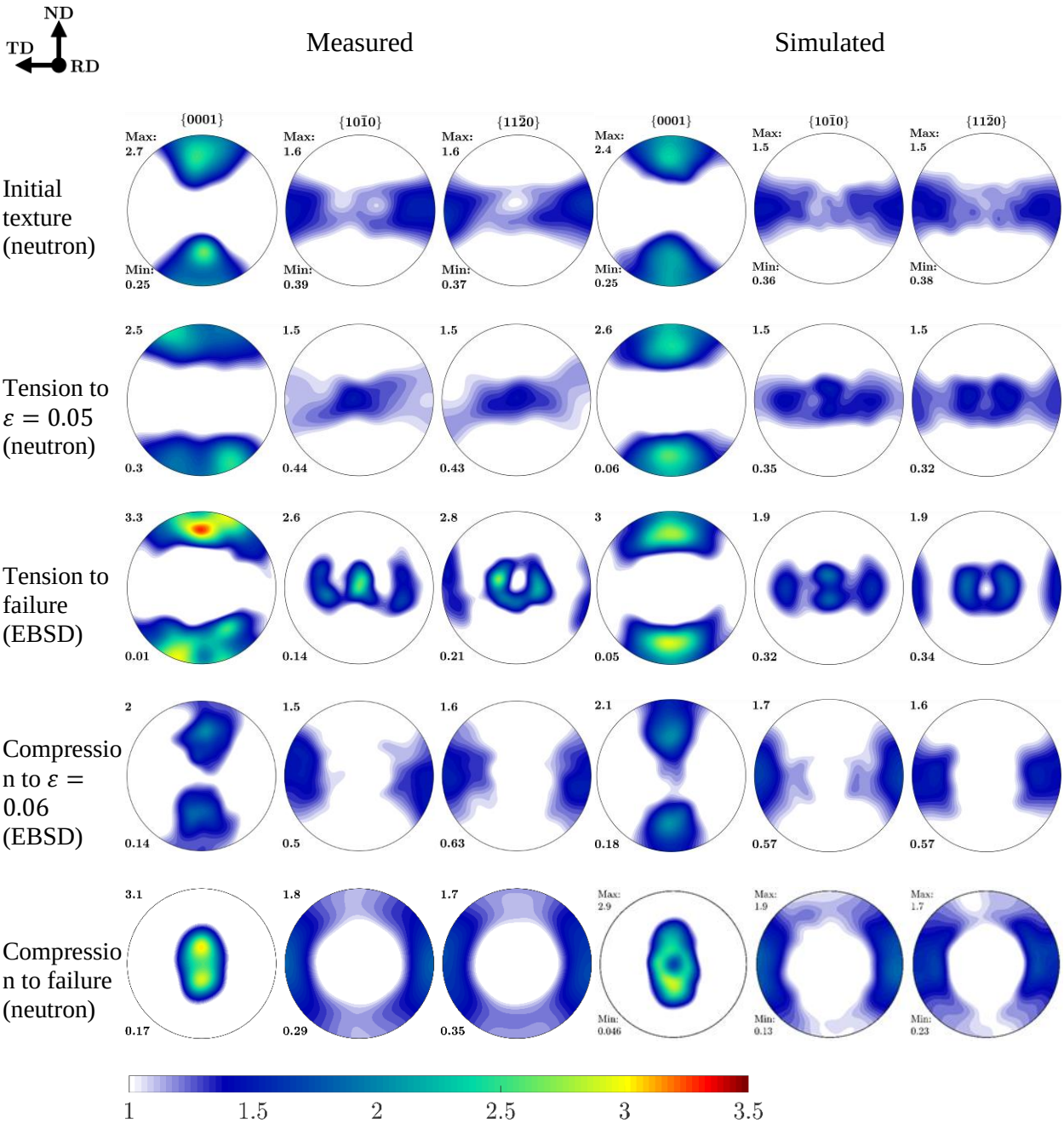

Fig. 7*. Stereographic pole figures showing a comparison of the measured and predicted texture evolution of WE43 deformed in simple tension and compression at room temperature along RD to strain levels indicated in the figure under* $\dot{\varepsilon} = 10^{-3}s^{-1}$ *strain rate.*

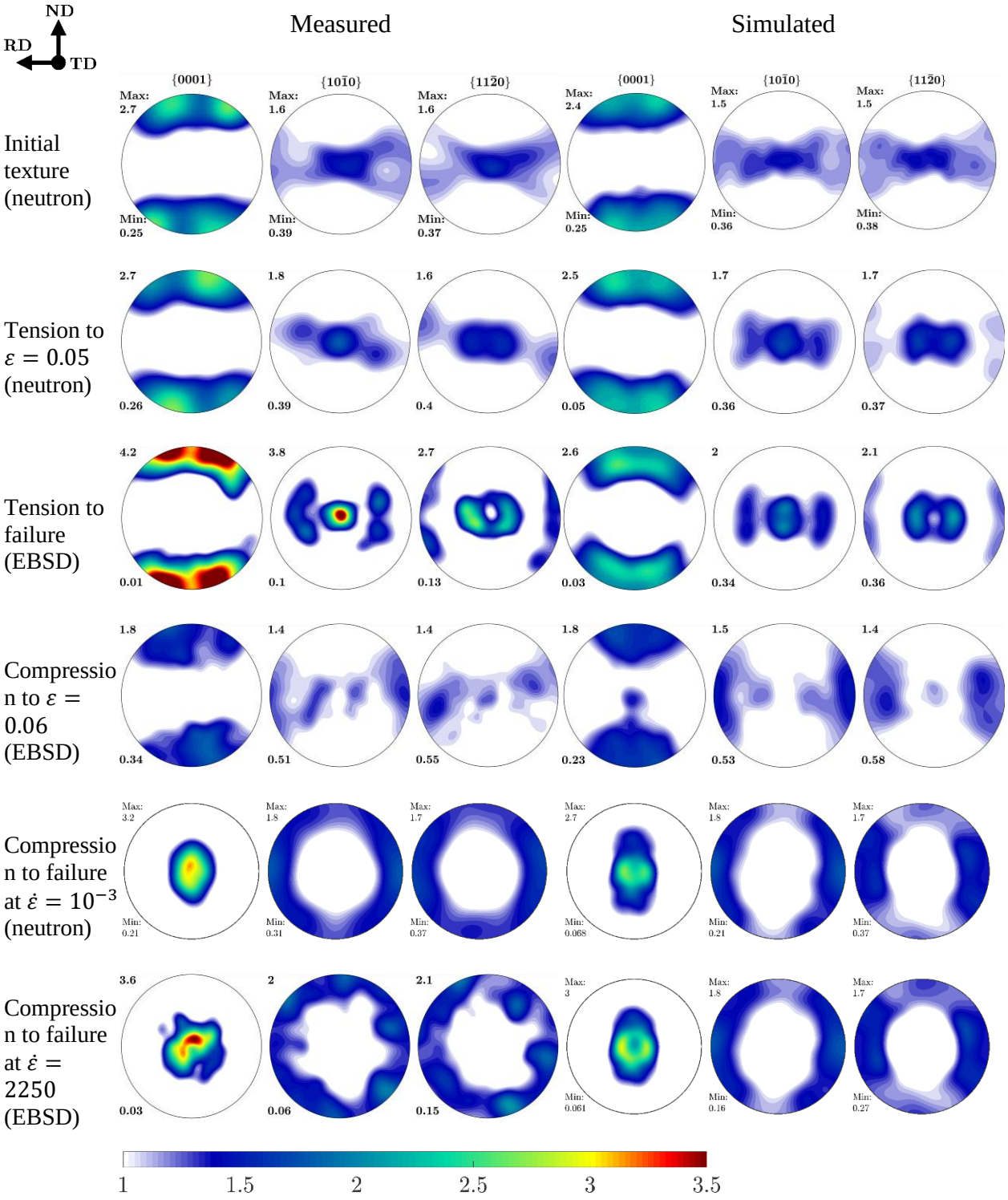

Fig. 8*. Stereographic pole figures showing comparison of the measured and predicted texture evolution of WE43 deformed in simple tension and compression at room temperature along TD to strain levels and strain rates indicated in the figure. If strain rate is not indicated, it is* $\dot{\varepsilon} = 10^{-3}s^{-1}$.

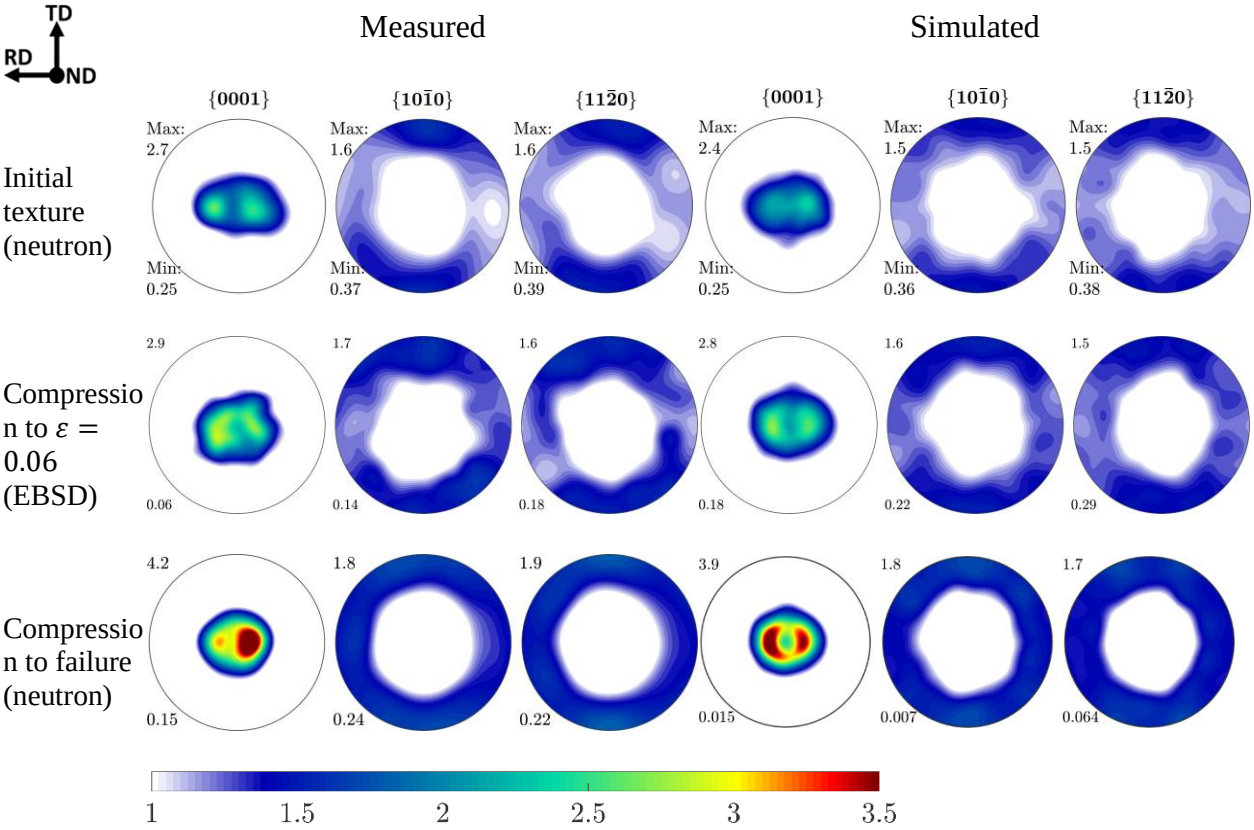

Fig. 9*. Stereographic pole figures showing comparison of the measured and predicted texture evolution of WE43 deformed in simple compression at room temperature along ND to strain levels indicated in the figure under* $\dot{\varepsilon} = 10^{-3}s^{-1}$ *strain rate.*

***Table 1**. Hardening law material parameters for the evolution of slip resistance. The Burgers vectors for basal, prismatic, and pyramidal slip modes are 3.21x10^{-10} m, 3.21x10^{-10} m, and 6.12x10^{-10} m, respectively. The shear modulus is 16,500 MPa (Meyers and Chawla, 1998).*

α – slip mode	Basal slip $\{0001\}\langle\bar{1}\bar{1}20\rangle$	Prismatic slip $\{\bar{1}100\}\langle\bar{1}\bar{1}20\rangle$	Pyramidal slip $\{10\bar{1}1\}\langle11\bar{2}\bar{3}\rangle$	Pyramidal slip $\{\bar{1}\bar{1}22\}\langle11\bar{2}3\rangle$
τ_0^{α} [MPa]	31	97	215	230
k_1^{α} [m^{-1}]	7.0E7	3.0E8	1.00E8	
g$^{\alpha}$	0.004	0.003	0.004	
D$^{\alpha}$ [MPa]	245	250	285	
q$^{\alpha}$	122	200	280	
H_1^{α}	0.1	0.03	0.05	
H_2^{α}	1.0	0.6	0.5	
H_3^{α}	1.0	0.6	0.5	

***Table 2**. Hardening law material parameters for the evolution of twin resistance. The Burgers vectors are 1.38x10^{-10} m, 1.38x10^{-10} m, and 9.24x10^{-11} m for extension 1, extension 2, and contraction twinning modes, respectively.*

β – twin mode	Extension twin I $\{10\bar{1}2\}\langle10\bar{1}\bar{1}\rangle$	Extension twin II $\{11\bar{2}1\}\langle11\bar{2}\bar{6}\rangle$	Contraction twin $\{10\bar{1}1\}\langle10\bar{1}\bar{2}\rangle$
τ_{crit}^{β} [MPa]	111	143	125
τ_{prop}^{β} [MPa]	96	131	100
H_0^{β} [MPa$\sqrt{\mu m}$]	30	40	60
$C^{\alpha\beta}, \alpha = 1$	$1.7E4 - 1.9E3 \ln(\dot{\varepsilon})$	$1.4E4 - 920 \ln(\dot{\varepsilon})$	$4.0E3 - 470 \ln(\dot{\varepsilon})$
$C^{\alpha\beta}, \alpha = 2$	$2.8E4 - 2.5E3 \ln(\dot{\varepsilon})$	$1.4E4 - 890 \ln(\dot{\varepsilon})$	$5.3E3 - 680 \ln(\dot{\varepsilon})$
$C^{\alpha\beta}, \alpha = 3$	$7.2E4 - 1.0E3 \ln(\dot{\varepsilon})$	$4.2E4 - 2.1E3 \ln(\dot{\varepsilon})$	$5.3E3 - 680 \ln(\dot{\varepsilon})$
$C^{\alpha\beta}, \alpha = 4$	$7.2E4 - 1.0E3 \ln(\dot{\varepsilon})$	$4.2E4 - 2.1E3 \ln(\dot{\varepsilon})$	$5.3E3 - 680 \ln(\dot{\varepsilon})$

As a final form of validation of the T-CPFE model for WE43, we compare predicted and experimentally measured geometry of deformed cylinders in Fig. 10. The cylinders for comparing geometrical changes were compressed to a strain of 0.16 along RD, TD, and ND. Initial diameter was 10 mm for the cylinders deformed along RD and TD and 8 mm for the cylinder deformed along ND, while the initial height was 10 mm for all. The symbols in Fig. 10 overlaid onto the photographs of the deformed cross sections denote the external nodal coordinates of the deformed FE models. The ratios between major and minor axis were 1.03, 1.05, and 1.02 for the cylinders compressed along RD, TD, and ND, respectively. The case study demonstrates that the T-CPFE model is able to capture the geometric changes originating from the texture-induced anisotropic material flow of the alloy.

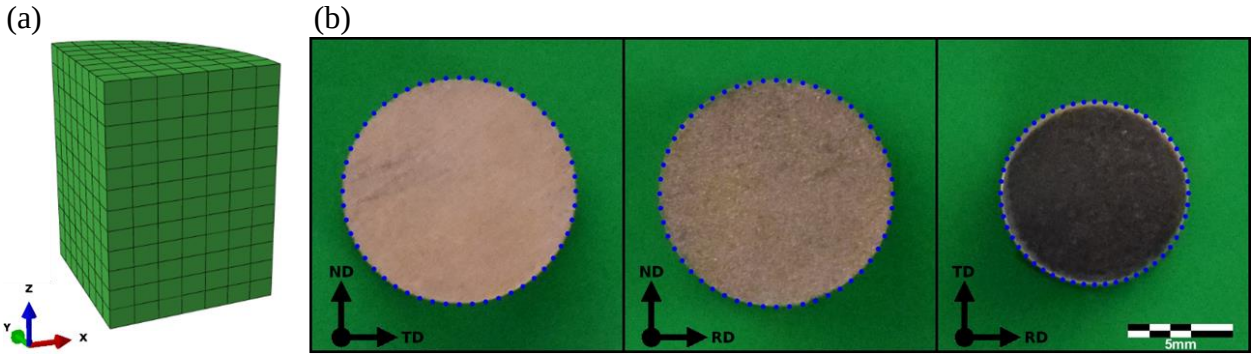

Fig. 10*. (a) A 1/8 of a cylindrical finite element model for the simple compression simulations consisted of 660 C3D8 elements. Every integration point initially embodies 80 crystal orientations totaling to 422,400. Every orientation is allowed to develop multiple twin variants and, therefore, the number of orientations at each integration point increases with strain very quickly. (b) Top view of the compression samples after 0.16 strain level compressed along the three directions indicated in the images. The external nodal coordinates of the deformed FE models are superimposed on the experimentally deformed samples of WE43.*

10. Discussion

In this work, a plate of alloy WE43 was tested in tension and compression and characterized as a function of strain rate. The material was found to exhibit a small level of anisotropy due to

texture and a small level of tension vs. compression asymmetry. Hardening rates were observed to be a strong function of strain rate. The behavior was modeled by the recently developed T-CPFE model. Good predictions of the flow stress response, texture, and twin volume fractions by the model is an indication that activities of deformation modes are correct. For a given deformation mode, α, the activity is calculated using

$$\text{Relative activity}^{\alpha} = \frac{\sum_{\alpha} \dot{\gamma}^{s}}{\sum_{s}^{N^{sl}} \dot{\gamma}^{s} + \sum_{t}^{N^{tw}} \dot{\gamma}^{t}}, \quad (19)$$

where the sum is over potential slip and twin systems. The value is calculated per grain, averaged over the cluster of grains embedded at every material point, and then finally averaged over all material points of the FE model. The activity plots pertain to the activity in the parent and the twinned domains. As is evident, the deformation in both domains is accommodated by slip and twinning. The model internally adjusts the relative amounts of active deformation modes based on the evolution of slip and twin resistances during the imposed loadings to predict the deformation characteristics.

The initial slip resistance of the deformation modes in WE43 embeds the strengthening contributions from lattice resistance, grain boundary barrier effect (i.e. the grain size Hall-Petch-like effect), solid solution, and precipitates shearing (Bhattacharyya et al., 2018). The hardening model used in the present work starts from the values of the calibrated initial slip/twin resistances without an explicit consideration of these strengthening effects. The grain boundary barrier effect could not be calibrated in the present work due to the need for flow stress data as a function of grain size. This mechanism, understood in terms of dislocation pile-ups at the grain boundary, is thus embedded in the initial resistances. Initial slip resistances can depend on strain rate and temperature (Ardeljan et al., 2016a; Knezevic et al., 2014b; Knezevic et al., 2013d). The

work presented for WE43 did not find any appreciable rate dependence, while its temperature dependence will be studied in future works. The ratio of the initial resistances at room temperature (i.e. no effect of evolution of dislocation densities, dislocation-dislocation, and dislocation-twin/grain boundaries interactions) for the basal, prismatic, pyramidal slip models and TTW 1, TTW 2, and CTW twinning modes are 1 : 3.1 : 6.9 : 3.6 : 4.6 : 4 (Tables 1 and 2). Comparing these ratios to basal, prismatic, pyramidal slip models and TTW mode for AZ31 of 1 : 4.1 : 14 : 1.2 (Ardeljan et al., 2016a) reveals that the ratios for WE43 are reduced and that the twinning is harder to activate in WE43 than in AZ31, which is known to deform by twinning profusely.

The slip/twin resistance values explicitly evolve as a function of the evolving microstructure (i.e. dislocation densities and barrier effects due to twinning). The hardening law used in this work intrinsically accounts for the effect of dynamic recovery being a function of strain rate on the rate of strain hardening. However, the effect is insufficient to model the hardening behavior of alloy WE43 as a function of strain rate. Thus, other microstructural features influence the hardening behavior of the ally, as elaborated next. To this end, deformation twinning is observed and quantified for the alloy as a function of strain rate. The Hall-Petch-like terms due to twin lamellae associated with particular deformation modes are considered by the model. These values are thus only for grains containing twins. The values are established for the first time here to predict the flow curves. The values associated with the CTW and DTW twins are found to be higher than for the TTW twins. This trend agrees with the finding that the contraction twins cause high barrier effects and hardening since these twins effectively cut the mean free path of mobile dislocations (Ardeljan et al., 2016a; Knezevic et al., 2010). In contrast, extension twins are known to cause a very small barrier effect because these twins grow quickly encompassing

grains and transmit dislocations (Molodov et al., 2017). Additionally, the Basinski effect cannot be significant due to the relatively small fraction of twins in WE43 compared to AZ31. TTW 1 plays a role in the texture evolution, especially under compression. The effect is larger in the TD than in the RD samples because more grains with their **c**-axis perpendicular to the loading direction exist in the TD than in the RD samples. As is evident from the samples deformed to a strain of 0.06 in compression, texture evolves slightly faster in the RD sample than in the TD sample because of a higher activity of basal slip in the RD than in the TD samples. However, the basal pole is more pronounced in the TD samples due to a slightly larger fraction of TTW 1 and pyramidal slip. While basal slip and TTW 1 explain the texture reorientation in compression, the cooperative action of prismatic and basal slip with small twinning activity does not cause substantial texture evolution in tension.

The initial texture is well oriented for the in-plane deformation by basal and prismatic slip. As is evident from the activity plots in Fig. 6, the most active slip mode initially is basal slip. The activity of prismatic slip increases rapidly with straining to cooperate with basal slip. In some cases, especially in tension, the activity of prismatic slip is higher than that of basal slip. The activity of twinning in tension is smaller than in compression. Such relative activities are the origin of the developed tension vs. compression asymmetry. Pyramidal slip activates within extension twin domains and is responsible for hardening in part because the pyramidal slip is harder than other slip modes. However, the activation of pyramidal slip within these twins causes moderate overall hardening due to a low fraction of TTW twins and pyramidal slip is not significantly harder in WE43 like in AZ31 due to solutes and precipitates, which harden more soft slip modes like basal slip and TTW. Moreover, the substantial activity of easy basal slip within twinned domains also suggests that the texture hardening due to twinning is moderate.

Thus, the contribution to hardening coming from texture (i.e. rotation of grains from softer to harder orientations) does not entirely explain the hardening behavior under high strain rates. Nevertheless, more activity of extension twinning under high strain rate deformation causes more hardening in such deformation conditions than in quasi-static conditions. Moreover, the CTW and DTW twins activate much more under high strain rate than quasi-static deformation. The barrier effect induced by boundaries of these twins is also hardening the alloy under high strain rate deformation. Thus, it is postulated here that the higher hardening rates under high strain rate deformation also arise from the reduction of the slip length of mobile dislocations.

11. Conclusions

In this paper, a multi-level crystal plasticity model, T-CPFE, is adapted to interpret the deformation behavior of the rare earth-containing Mg alloy, WE43, deforming by a combination of elasticity, slip, and twinning as a function of strain rate. Activation of slip and twinning deformation systems at the grain level is based on a dislocation-based hardening law. The model is initialized using the measured initial texture of the alloy and the evolution of texture during deformation due to multiple slip and twinning modes carrying out the plastic deformation is accounted for. Crystal lattice reorientation due to twinning is incorporated using the composite grain twinning model. The grain level response is homogenized using the Taylor-type crystal plasticity theory at the polycrystal meso-scale level at every FE material point and then using the FE approach over FE mesh at the polycrystal macro-scale level.

It is observed that the alloy shows monotonically falling strain hardening in tension and compression along both RD and TD testing direction. Anisotropy in strain hardening in tension vs. compression is small under quasi-static deformation and, thus, the tension vs. compression asymmetry is not pronounced. However, strain hardening rates are much higher under high strain

rate than quasi-static deformation conditions. The model is adjusted and validated on a comprehensive set of data collected for the alloy in tension and compression over a range of strain rates up to 2250 s^{-1}. Good agreement between the calculated and measured material response in terms of flow stress, strain hardening, anisotropy, and asymmetry is achieved as a function of strain rate using a single set of hardening parameters. Moreover, texture evolution and twin volume fractions are well predicted. The mechanical behavior and evolution of microstructure are governed by the relative amounts of active crystallographic deformation mechanisms. The basal slip and TTW 1 are strengthened by precipitates much more than prismatic and pyramidal slip modes in the alloy WE43 reducing the relative strength ratio in comparison to that in AZ31. The origin of small anisotropy and tension vs. compression asymmetry exhibited by the alloy during quasi-static deformation was found to be in less TTW 1 and more of the prismatic slip active during tension as opposed to more TTW 1 and more of the basal slip activity during compression. The relative activity of twinning and especially contraction and double twinning modes are found to explain the higher strain hardening rates under high strain rate deformation than under the quasi-static conditions. In this case, while texture hardening is moderate, the barrier effect contribution to hardening is significant. In closing, it is worth indicating that since the T-CPFE model operates within FE framework, it can be used to simulate geometrical changes during plastic deformation of WE43 as a function of strain rate. While geometrical changes during simple compression are presented here, more complicated simulations like Taylor impact tests will be studied in the future. Such simulations will test whether the model can extrapolate good predictive characteristics to even higher strain rate regimes.

Acknowledgements

This research was sponsored by the U.S. Army Research Laboratory and was accomplished under a Cooperative Agreement No. W911NF-15-2-0084. D.J.S. acknowledges support through a NSF Graduate Research Fellowship. N.G. and C.X. acknowledge a U.S. Army Research Laboratory Cooperative Agreement No. W911NF-11-2-0096.

Appendix A

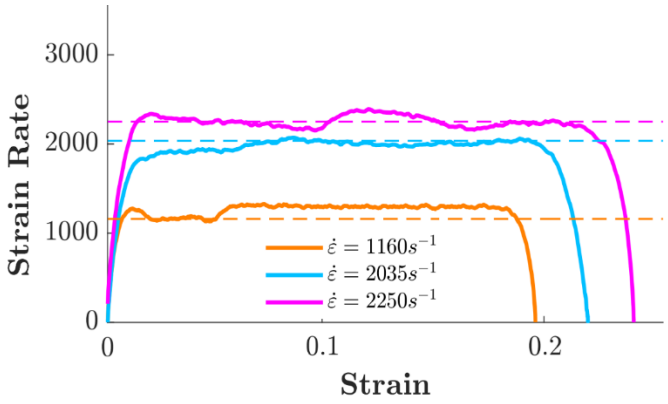

Fig. A1. *Strain rate vs. strain raw data showing the level of variation of strain rate per dynamic test.*

Figure A2 shows the image quality (IQ) maps of samples deformed to fracture (~0.18 strain) under quasi-static compression and 2250 s^{-1} in TD. A large fraction of the dark bands in the IQ map are believed to be contraction/double twins. For some of these bands, it was possible to confirm that the misorientation across the boundary was the expected misorientation for the double twin. Such observations were also made in other works (Al-Samman and Gottstein, 2008; Barnett, 2007b; Knezevic et al., 2010). It was also seen that these twins do not alter texture because the volume fraction occupied by these twins is very small, and therefore much of the plastic strain is most likely accommodated by the pyramidal slip. The confidence index on the orientation measurements inside these thin bands was low because the deformation structure inside these double twins is complex influencing indexable patterns. As is evident, there is less

of the double twin lamellae in (a) vs (b). The twin analysis suggests that double twinning is much more rate-sensitive than extension twinning. Figures A3 and A4 show twinning in compression along ND and tension along TD, respectively. As is evident, there is less twinning during material contraction along ND with more activity of contraction twins than along in-plane compression under quasi-static conditions.

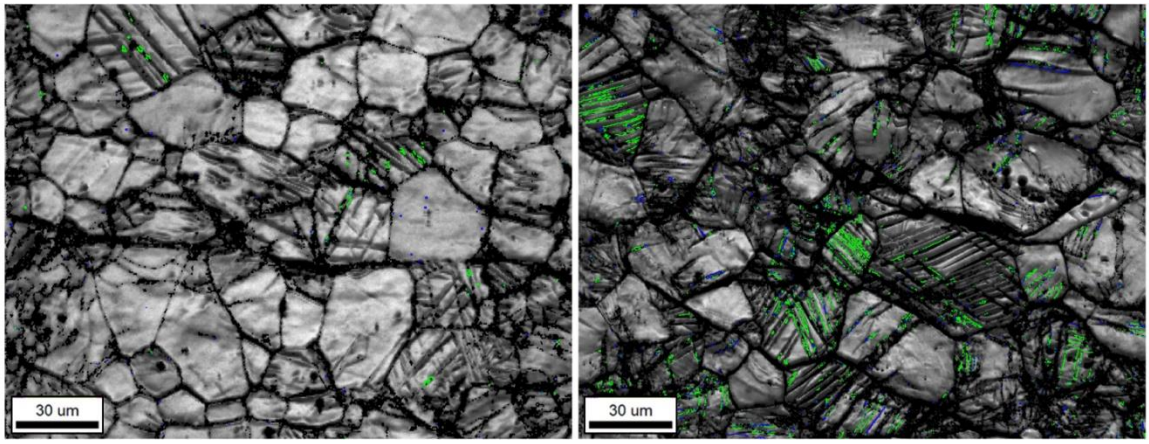

Fig. A2*. Image quality maps showing density of twin type features in compression to fracture (~0.18 strain) along TD at (a) 0.001* s^{-1}*, and (b) 2250* s^{-1} *strain rates. The highlighted boundaries are type 1 DTW = green and type 2 DTW=blue.*

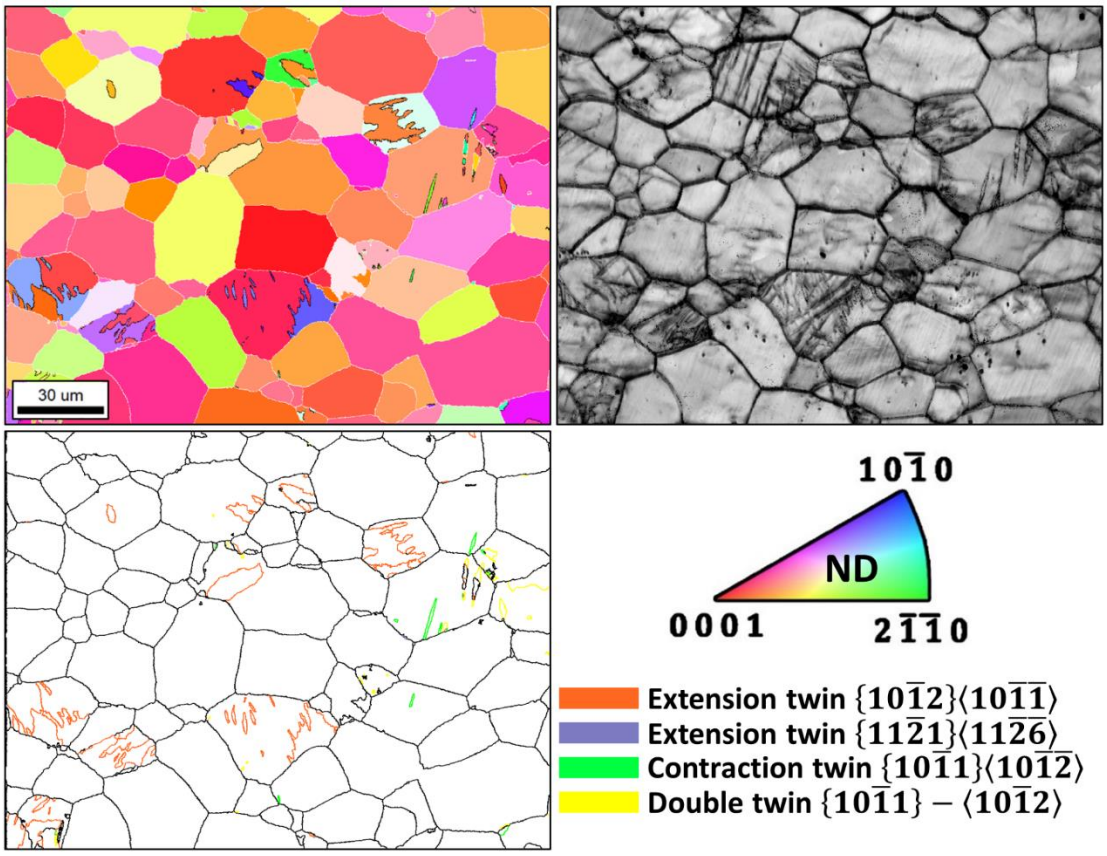

Fig. A3*. An EBSD inverse pole figure map and corresponding IQ and blank maps showing microstructure in the pre-strained sample in simple compression along ND under 0.001 s^{-1} strain rate at room temperature to a true strain level of 0.15. The compression direction is perpendicular to the map. The colors in the map represent the orientation of the compression axis with respect to the local crystal lattice frame according to the IPF triangle.*

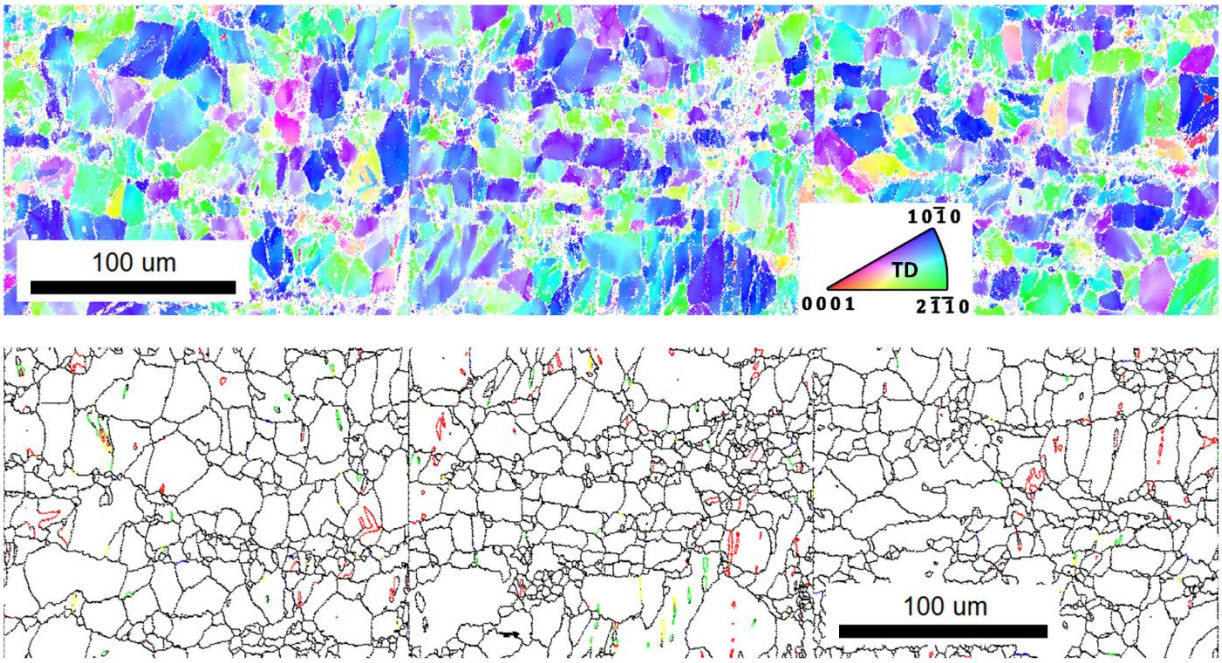

***Fig. A4**. EBSD inverse pole figure maps showing microstructure in a pre-strained sample that was loaded in simple tension along TD (top) and RD (bottom) to a true strain of 0.05. The tension experiments were performed at a strain rate of 0.001 s^{-1} and at room temperature. The tensile direction is perpendicular to the maps. The colors in the maps represent the orientation of the tensile axis with respect to the local crystal lattice frame according to the IPF triangle. The corresponding blank maps highlight twin boundaries with colors as in Fig. A3.*

References

2011. ASTM B951-11 Standard Practice for Codification of Unalloyed Magnesium and Magnesium-Alloys, Cast and Wrought, , West Conshohocken, PA, .

2015. ASTM E8/E8M-15a, Standard Test Methods for Tension Testing of Metallic Materials. ASTM International, West Conshohocken, PA.

Abdolvand, H., Majkut, M., Oddershede, J., Schmidt, S., Lienert, U., Diak, B.J., Withers, P.J., Daymond, M.R., 2015. On the deformation twinning of Mg AZ31B: A three-dimensional synchrotron X-ray diffraction experiment and crystal plasticity finite element model. Int. J. Plast. 70, 77-97.

Al-Samman, T., Gottstein, G., 2008. Room temperature formability of a magnesium AZ31 alloy: Examining the role of texture on the deformation mechanisms. Mater. Sci. Eng. A 488, 406-414.

Al-Samman, T., Li, X., 2011. Sheet texture modification in magnesium-based alloys by selective rare earth alloying. Materials Science and Engineering: A 528, 3809-3822.

Ardeljan, M., Beyerlein, I.J., Knezevic, M., 2017. Effect of dislocation density-twin interactions on twin growth in AZ31 as revealed by explicit crystal plasticity finite element modeling. Int. J. Plast. 99, 81-101.

Ardeljan, M., Beyerlein, I.J., McWilliams, B.A., Knezevic, M., 2016a. Strain rate and temperature sensitive multi-level crystal plasticity model for large plastic deformation behavior: Application to AZ31 magnesium alloy. Int. J. Plast. 83, 90-109.

Ardeljan, M., Knezevic, M., 2018. Explicit modeling of double twinning in AZ31 using crystal plasticity finite elements for predicting the mechanical fields for twin variant selection and fracture analyses. Acta. Mater. 157, 339-354.

Ardeljan, M., McCabe, R.J., Beyerlein, I.J., Knezevic, M., 2015. Explicit incorporation of deformation twins into crystal plasticity finite element models. Computer Methods in Applied Mechanics and Engineering 295, 396-413.

Ardeljan, M., Savage, D.J., Kumar, A., Beyerlein, I.J., Knezevic, M., 2016b. The plasticity of highly oriented nano-layered Zr/Nb composites. Acta. Mater. 115, 189-203.

Asaro, R.J., Needleman, A., 1985. Texture development and strain hardening in rate dependent polycrystals. Acta Metall. Mater. 33, 923-953.

Asgari, S., El-Danaf, E., Kalidindi, S.R., Doherty, R.D., 1997. Strain hardening regimes and microstructural evolution during large strain compression of low stacking fault energy fcc alloys that form deformation twins. Metall. Mater. Trans. A 28A, 1781-1795.

Avedesian, M.M., Baker, H., 1999. ASM speciality handbook: magnesium and magnesium alloys. New York: ASM International 27.

Barnett, M.R., 2007a. Twinning and the ductility of magnesium alloys: Part I: "Tension" twins. Mater. Sci. Eng. A 464, 1-7.

Barnett, M.R., 2007b. Twinning and the ductility of magnesium alloys: Part II. "Contraction" twins. Mater. Sci. Eng. A 464, 8-16.

Basinski, Z.S., Szczerba, M.S., Niewczas, M., Embury, J.D., Basinski, S.J., 1997. Transformation of slip dislocations during twinning of copper-aluminum alloy crystals. Revue de Metallurgie. Cahiers D'Informations Techniques 94, 1037-1044.

Beyerlein, I.J., Tomé, C.N., 2008. A dislocation-based constitutive law for pure Zr including temperature effects. Int. J. Plast. 24, 867-895.

Bhattacharyya, J.J., Wang, F., Stanford, N., Agnew, S.R., 2018. Slip mode dependency of dislocation shearing and looping of precipitates in Mg alloy WE43. Acta. Mater. 146, 55-62.

Bhattacharyya, J.J., Wang, F., Wu, P.D., Whittington, W.R., El Kadiri, H., Agnew, S.R., 2016. Demonstration of alloying, thermal activation, and latent hardening effects on quasi-static and dynamic polycrystal plasticity of Mg alloy, WE43-T5, plate. Int. J. Plast. 81, 123-151.

Bohlen, J., Nürnberg, M.R., Senn, J.W., Letzig, D., Agnew, S.R., 2007. The texture and anisotropy of magnesium–zinc–rare earth alloy sheets. Acta Materialia 55, 2101-2112.

Bouvier, S., Benmhenni, N., Tirry, W., Gregory, F., Nixon, M.E., Cazacu, O., Rabet, L., 2012. Hardening in relation with microstructure evolution of high purity α−titanium deformed under monotonic and cyclic simple shear loadings at room temperature. Mater. Sci. Eng. A 535, 12-21.

Carpenter, J.S., Nizolek, T., McCabe, R.J., Knezevic, M., Zheng, S.J., Eftink, B.P., Scott, J.E., Vogel, S.C., Pollock, T.M., Mara, N.A., Beyerlein, I.J., 2015. Bulk texture evolution of nanolamellar Zr–Nb composites processed via accumulative roll bonding. Acta. Mater. 92, 97-108.

Castellani, C., Lindtner, R.A., Hausbrandt, P., Tschegg, E., Stanzl-Tschegg, S.E., Zanoni, G., Beck, S., Weinberg, A.-M., 2011. Bone–implant interface strength and osseointegration: Biodegradable magnesium alloy versus standard titanium control. Acta Biomaterialia 7, 432-440.

Cheng, J., Shen, J., Mishra, R.K., Ghosh, S., 2018. Discrete twin evolution in Mg alloys using a novel crystal plasticity finite element model. Acta. Mater. 149, 142-153.

Cho, K., Sano, T., Doherty, K., Yen, C., Gazonas, G., Montgomery, J., Moy, P., Davis, B., DeLorme, R., 2009. Magnesium technology and manufacturing for ultra lightweight armored ground vehicles. DTIC Document.

Clausen, B., Tomé, C.N., Brown, D.W., Agnew, S.R., 2008. Reorientation and stress relaxation due to twinning: Modeling and experimental characterization for Mg. Acta. Mater. 56, 2456-2468.

Eckelmeyer, K.H., Hertzberg, R.W., 1970. Deformation in wrought Mg− 9Wt Pct Y. Metallurgical Transactions 1, 3411-3414.

Eghtesad, A., Barrett, T.J., Germaschewski, K., Lebensohn, R.A., McCabe, R.J., Knezevic, M., 2018. OpenMP and MPI implementations of an elasto-viscoplastic fast Fourier transform-based micromechanical solver for fast crystal plasticity modeling. Advances in Engineering Software 126, 46-60.

El Kadiri, H., Oppedal, A.L., 2010. A crystal plasticity theory for latent hardening by glide twinning through dislocation transmutation and twin accommodation effects. J. Mech. Phys. Solids 58, 613-624.

Essmann, U., Mughrabi, H., 1979. Annihilation of dislocations during tensile and cyclic deformation and limits of dislocation densities. Philosophical Magazine A 40, 731-756.

Fernández, A., Jérusalem, A., Gutiérrez-Urrutia, I., Pérez-Prado, M.T., 2013. Three-dimensional investigation of grain boundary–twin interactions in a Mg AZ31 alloy by electron backscatter diffraction and continuum modeling. Acta. Mater. 61, 7679-7692.

Gavras, S., Zhu, S.M., Nie, J.F., Gibson, M.A., Easton, M.A., 2016. On the microstructural factors affecting creep resistance of die-cast Mg–La-rare earth (Nd, Y or Gd) alloys. Materials Science and Engineering: A 675, 65-75.

Ghorbanpour, S., McWilliams, B.A., Knezevic, M., 2019a. Effect of hot working and aging heat treatments on monotonic, cyclic, and fatigue behavior of WE43 magnesium alloy. Mater. Sci. Eng. A 747, 27-41.

Ghorbanpour, S., McWilliams, B.A., Knezevic, M., 2019b. Effect of Hot Working on the High Cycle Fatigue Behavior of WE43 Rare Earth Magnesium Alloy. Springer International Publishing, Cham, pp. 219-225.

Gribbin, S., Bicknell, J., Jorgensen, L., Tsukrov, I., Knezevic, M., 2016. Low cycle fatigue behavior of direct metal laser sintered Inconel alloy 718. Int. J. Fatigue 93, Part 1, 156-167.

Gribbin, S., Ghorbanpour, S., Ferreri, N.C., Bicknell, J., Tsukrov, I., Knezevic, M., 2019. Role of grain structure, grain boundaries, crystallographic texture, precipitates, and porosity on fatigue behavior of Inconel 718 at room and elevated temperatures. Mater. Charact. 149, 184-197.

Hadorn, J.P., Hantzsche, K., Yi, S., Bohlen, J., Letzig, D., Wollmershauser, J.A., Agnew, S.R., 2012. Role of Solute in the Texture Modification During Hot Deformation of Mg-Rare Earth Alloys. Metall. Mater. Trans. A 43, 1347-1362.

Hantzsche, K., Bohlen, J., Wendt, J., Kainer, K.U., Yi, S.B., Letzig, D., 2010. Effect of rare earth additions on microstructure and texture development of magnesium alloy sheets. Scripta Materialia 63, 725-730.

Hidalgo-Manrique, P., Robson, J.D., Pérez-Prado, M.T., 2017. Precipitation strengthening and reversed yield stress asymmetry in Mg alloys containing rare-earth elements: A quantitative study. Acta Materialia 124, 456-467.

Hutchinson, J.W., 1976. Bounds and self-consistent estimates for creep of polycrystalline materials. Proceedings of the Royal Society of London. Series A, Mathematical and Physical Sciences 348, 101-126.

Imandoust, A., Barrett, C.D., Al-Samman, T., Inal, K.A., El Kadiri, H., 2017. A review on the effect of rare-earth elements on texture evolution during processing of magnesium alloys. J. Mater. Sci. 52, 1-29.

Jahedi, M., Ardeljan, M., Beyerlein, I.J., Paydar, M.H., Knezevic, M., 2015. Enhancement of orientation gradients during simple shear deformation by application of simple compression. J. Appl. Phys. 117, 214309.

Jahedi, M., McWilliams, B.A., Kellogg, F.R., Beyerlein, I.J., Knezevic, M., 2018a. Rate and temperature dependent deformation behavior of as-cast WE43 magnesium-rare earth alloy manufactured by direct-chill casting. Mater. Sci. Eng. A 712, 50-64.

Jahedi, M., McWilliams, B.A., Knezevic, M., 2018b. Deformation and fracture mechanisms in WE43 magnesium-rare earth alloy fabricated by direct-chill casting and rolling. Mater. Sci. Eng. A 726, 194-207.

Jahedi, M., McWilliams, B.A., Moy, P., Knezevic, M., 2017. Deformation twinning in rolled WE43-T5 rare earth magnesium alloy: Influence on strain hardening and texture evolution. Acta. Mater. 131, 221-232.

Jain, A., Agnew, S.R., 2007. Modeling the temperature dependent effect of twinning on the behavior of Mg alloy AZ31 sheet. Mater. Sci. Eng. A, 29-36.

Jiang, M.G., Xu, C., Nakata, T., Yan, H., Chen, R.S., Kamado, S., 2016. Rare earth texture and improved ductility in a Mg-Zn-Gd alloy after high-speed extrusion. Materials Science and Engineering: A 667, 233-239.

Kalidindi, S.R., 1998. Incorporation of deformation twinning in crystal plasticity models. J. Mech. Phys. Solids 46, 267-271.

Kaschner, G.C., Tomé, C.N., McCabe, R.J., Misra, A., Vogel, S.C., Brown, D.W., 2007. Exploring the dislocation/twin interactions in zirconium. Mater. Sci. Eng. A 463, 122-127.

Keshavarz, S., Ghosh, S., 2015. Hierarchical crystal plasticity FE model for nickel-based superalloys: Sub-grain microstructures to polycrystalline aggregates. International Journal of Solids and Structures 55, 17-31.

King, J.F., 2007. Magnesium: commodity or exotic? Materials Science and Technology 23, 1-14.

Knezevic, M., Al-Harbi, H.F., Kalidindi, S.R., 2009. Crystal plasticity simulations using discrete Fourier transforms. Acta. Mater. 57, 1777-1784.

Knezevic, M., Beyerlein, I.J., 2018. Multiscale Modeling of Microstructure-Property Relationships of Polycrystalline Metals during Thermo-Mechanical Deformation. Advanced Engineering Materials 20, 1700956.

Knezevic, M., Beyerlein, I.J., Brown, D.W., Sisneros, T.A., Tomé, C.N., 2013a. A polycrystal plasticity model for predicting mechanical response and texture evolution during strain-path changes: Application to beryllium. Int. J. Plast. 49, 185-198.

Knezevic, M., Beyerlein, I.J., Lovato, M.L., Tomé, C.N., Richards, A.W., McCabe, R.J., 2014a. A strain-rate and temperature dependent constitutive model for BCC metals incorporating non-Schmid effects: Application to tantalum–tungsten alloys. Int. J. Plast. 62, 93-104.

Knezevic, M., Capolungo, L., Tomé, C.N., Lebensohn, R.A., Alexander, D.J., Mihaila, B., McCabe, R.J., 2012. Anisotropic stress-strain response and microstructure evolution of textured α-uranium. Acta. Mater. 60, 702-715.

Knezevic, M., Carpenter, J.S., Lovato, M.L., McCabe, R.J., 2014b. Deformation behavior of the cobalt-based superalloy Haynes 25: Experimental characterization and crystal plasticity modeling. Acta. Mater. 63, 162-168.

Knezevic, M., Jahedi, M., Korkolis, Y.P., Beyerlein, I.J., 2014c. Material-based design of the extrusion of bimetallic tubes. Comput. Mater. Sci. 95, 63-73.

Knezevic, M., Kalidindi, S.R., Fullwood, D., 2008. Computationally efficient database and spectral interpolation for fully plastic Taylor-type crystal plasticity calculations of face-centered cubic polycrystals. Int. J. Plast. 24, 1264-1276.

Knezevic, M., Landry, N.W., 2015. Procedures for reducing large datasets of crystal orientations using generalized spherical harmonics. Mechanics of Materials 88, 73-86.

Knezevic, M., Lebensohn, R.A., Cazacu, O., Revil-Baudard, B., Proust, G., Vogel, S.C., Nixon, M.E., 2013b. Modeling bending of α-titanium with embedded polycrystal plasticity in implicit finite elements. Mater. Sci. Eng. A 564, 116-126.

Knezevic, M., Levinson, A., Harris, R., Mishra, R.K., Doherty, R.D., Kalidindi, S.R., 2010. Deformation twinning in AZ31: Influence on strain hardening and texture evolution. Acta. Mater. 58, 6230-6242.

Knezevic, M., McCabe, R.J., Lebensohn, R.A., Tomé, C.N., Liu, C., Lovato, M.L., Mihaila, B., 2013c. Integration of self-consistent polycrystal plasticity with dislocation density based hardening laws within an implicit finite element framework: Application to low-symmetry metals. J. Mech. Phys. Solids 61, 2034-2046.

Knezevic, M., McCabe, R.J., Tomé, C.N., Lebensohn, R.A., Chen, S.R., Cady, C.M., Gray Iii, G.T., Mihaila, B., 2013d. Modeling mechanical response and texture evolution of α-uranium as a function of strain rate and temperature using polycrystal plasticity. Int. J. Plast. 43, 70-84.

Knezevic, M., Zecevic, M., Beyerlein, I.J., Bingert, J.F., McCabe, R.J., 2015. Strain rate and temperature effects on the selection of primary and secondary slip and twinning systems in HCP Zr. Acta. Mater. 88, 55-73.

Knezevic, M., Zecevic, M., Beyerlein, I.J., Lebensohn, R.A., 2016. A numerical procedure enabling accurate descriptions of strain rate-sensitive flow of polycrystals within crystal visco-plasticity theory. Computer Methods in Applied Mechanics and Engineering 308, 468-482.

Kumar, A., Morrow, B.M., McCabe, R.J., Beyerlein, I.J., 2017. First-principles study of hc + ai dislocations in Mg. Materials Science and Engineering A (submitted).

Kumar, A.M., Kanjarla, A.K., Niezgoda, S.R., Lebensohn, R.A., Tomé, C.N., 2015. Numerical study of the stress state of a deformation twin in magnesium. Acta. Mater. 84, 349-358.

Lebensohn, R.A., Kanjarla, A.K., Eisenlohr, P., 2012. An elasto-viscoplastic formulation based on fast Fourier transforms for the prediction of micromechanical fields in polycrystalline materials. Int. J. Plast. 32–33, 59-69.

Lebensohn, R.A., Tomé, C.N., 1993. A self-consistent anisotropic approach for the simulation of plastic deformation and texture development of polycrystals: Application to zirconium alloys. Acta Metall. Mater. 41, 2611-2624.

Lentz, M., Klaus, M., Beyerlein, I.J., Zecevic, M., Reimers, W., Knezevic, M., 2015. In situ X-ray diffraction and crystal plasticity modeling of the deformation behavior of extruded Mg–Li–(Al) alloys: An uncommon tension–compression asymmetry. Acta. Mater. 86, 254-268.

Li, D., Dong, J., Zeng, X., Lu, C., Ding, W., 2007. Characterization of precipitate phases in a Mg–Dy–Gd–Nd alloy. Journal of alloys and compounds 439, 254-257.

Li, Q.a., Li, X., Zhang, Q., Chen, J., 2010. Effect of rare-earth element Sm on the corrosion behavior of Mg-6Al-1.2Y-0.9Nd alloy. Rare Metals 29, 557-560.

Lou, X.Y., Li, M., Boger, R.K., Agnew, S.R., Wagoner, R.H., 2007. Hardening evolution of AZ31B Mg sheet. Int. J. Plast. 23, 44-86.

Madec, R., Devincre, B., Kubin, L.P., 2002. From Dislocation Junctions to Forest Hardening. Physical Review Letters 89, 255508.

Marshall, P.E., Proust, G., Rogers, J.T., McCabe, R.J., 2010. Automatic twin statistics from electron backscattered diffraction data. Journal of Microscopy 238, 218-229.

Mecking, H., Kocks, U.F., 1981. Kinetics of flow and strain-hardening. Acta Metall. Mater. 29, 1865-1875.

Mengucci, P., Barucca, G., Riontino, G., Lussana, D., Massazza, M., Ferragut, R., Aly, E.H., 2008. Structure evolution of a WE43 Mg alloy submitted to different thermal treatments. Materials Science and Engineering: A 479, 37-44.

Meyers, M.A., Chawla, K.K., 1998. Mechanical Behavior of Materials. Prentice Hall, Upper Saddle River, New Jersey.

Molodov, K.D., Al-Samman, T., Molodov, D.A., 2017. Profuse slip transmission across twin boundaries in magnesium. Acta. Mater. 124, 397-409.

Nie, J.-F., 2012. Precipitation and Hardening in Magnesium Alloys. Metall. Mater. Trans. A 43, 3891-3939.

Nie, J.F., Muddle, B.C., 2000. Characterisation of strengthening precipitate phases in a Mg–Y–Nd alloy. Acta. Mater. 48, 1691-1703.

Nie, J.F., Xiao, X.L., Luo, C.P., Muddle, B.C., 2001. Characterisation of precipitate phases in magnesium alloys using electron microdiffraction. Micron 32, 857-863.

Proust, G., Tomé, C.N., Jain, A., Agnew, S.R., 2009. Modeling the effect of twinning and detwinning during strain path changes of Mg alloy AZ31. International Journal of Plasticity 25, 861-880.

Proust, G., Tomé, C.N., Kaschner, G.C., 2007. Modeling texture, twinning and hardening evolution during deformation of hexagonal materials. Acta. Mater. 55, 2137-2148.

Risse, M., Lentz, M., Fahrenson, C., Reimers, W., Knezevic, M., Beyerlein, I.J., 2017. Elevated Temperature Effects on the Plastic Anisotropy of an Extruded Mg-4 Wt Pct Li Alloy: Experiments and Polycrystal Modeling. Metall. Mater. Trans. A 48, 446-458.

Sandlöbes, S., Pei, Z., Friák, M., Zhu, L.F., Wang, F., Zaefferer, S., Raabe, D., Neugebauer, J., 2014. Ductility improvement of Mg alloys by solid solution: Ab initio modeling, synthesis and mechanical properties. Acta Materialia 70, 92-104.

Song, S.G., Gray, I., G. T., 1995. Structural interpretation of the nucleation and growth of deformation twins in Zr and Ti--II. Tem study of twin morphology and defect reactions during twinning. Acta Metall. Mater. 43, 2339-2350.

Stanford, N., 2008. Observation of {11 2 1} twinning in a Mg-based alloy. Philosophical magazine letters 88, 379-386.

Stanford, N., Barnett, M.R., 2008. The origin of "rare earth" texture development in extruded Mg-based alloys and its effect on tensile ductility. Materials Science and Engineering: A 496, 399-408.

Stanford, N., Marceau, R.K.W., Barnett, M.R., 2015. The effect of high yttrium solute concentration on the twinning behaviour of magnesium alloys. Acta. Mater. 82, 447-456.

Staroselsky, A., Anand, L., 2003. A constitutive model for hcp materials deforming by slip and twinning: application to magnesium alloy AZ31B. Int. J. Plast. 19, 1843-1864.

Taylor, G.I., 1938. Plastic strain in metals. Journal of the Institute of Metals 62, 307-324.

Tomé, C., Kaschner, G.C., 2005. Modeling Texture, Twinning and Hardening Evolution during Deformation of Hexagonal Materials. Materials Science Forum 495-497, 1001-1006.

Tomé, C.N., Lebensohn, R.A., Kocks, U.F., 1991. A model for texture development dominated by deformation twinning: Application to zirconium alloys. Acta Metall. Mater. 39, 2667-2680.

Tomé, C.N., Maudlin, P.J., Lebensohn, R.A., Kaschner, G.C., 2001. Mechanical response of zirconium: I. Derivation of a polycrystal constitutive law and finite element analysis. Acta. Mater. 49, 3085-3096.

Van Houtte, P., 1978. Simulation of the rolling and shear texture of brass by the Taylor theory adapted for mechanical twinning. Acta Metall. Mater. 26, 591-604.

Van Houtte, P., 1988. A Comprehensive Mathematical Formulation of an Extended Taylor-Bishop-Hill Model Featuring Relaxed Constraints, the Renouard-Wintenberger Theory and a Strain Rate Sensitivity Model. Textures and Microstructures 8-9, 313-350.

Vogel, S.C., Hartig, C., Lutterotti, L., Von Dreele, R.B., Wenk, H.R., Williams, D.J., 2004. Texture measurements using the new neutron diffractometer HIPPO and their analysis using the Rietveld method. Powder Diffraction 19, 65-68.

Wang, H., Raeisinia, B., Wu, P.D., Agnew, S.R., Tomé, C.N., 2010. Evaluation of self-consistent polycrystal plasticity models for magnesium alloy AZ31B sheet. International Journal of Solids and Structures 47, 2905-2917.

Wenk, H.R., Lutterotti, L., Vogel, S., 2003. Texture analysis with the new HIPPO TOF diffractometer. Nuclear Instruments & Methods in Physics Research Section a-Accelerators Spectrometers Detectors and Associated Equipment 515, 575-588.

Wu, X., Kalidindi, S.R., Necker, C., Salem, A.A., 2007. Prediction of crystallographic texture evolution and anisotropic stress-strain curves during large plastic strains in high purity α-titanium using a Taylor-type crystal plasticity model. Acta. Mater. 55, 423-432.

Xiang, C., Gupta, N., Coelho, P., Cho, K., 2018. Effect of microstructure on tensile and compressive behavior of WE43 alloy in as cast and heat treated conditions. Mater. Sci. Eng. A 710, 74-85.

Yoo, M.H., 1981. Slip, twinning, and fracture in hexagonal close-packed metals. Metall. Mater. Trans. A 12, 409–418.

Zecevic, M., Beyerlein, I.J., Knezevic, M., 2017a. Coupling elasto-plastic self-consistent crystal plasticity and implicit finite elements: Applications to compression, cyclic tension-compression, and bending to large strains. Int. J. Plast. 93, 187-211.

Zecevic, M., Beyerlein, I.J., Knezevic, M., 2018a. Activity of pyramidal I and II <c+a> slip in Mg alloys as revealed by texture development. J. Mech. Phys. Solids 111, 290-307.

Zecevic, M., Beyerlein, I.J., McCabe, R.J., McWilliams, B.A., Knezevic, M., 2016a. Transitioning rate sensitivities across multiple length scales: Microstructure-property relationships in the Taylor cylinder impact test on zirconium. Int. J. Plast. 84, 138-159.

Zecevic, M., Knezevic, M., 2018. Latent hardening within the elasto-plastic self-consistent polycrystal homogenization to enable the prediction of anisotropy of AA6022-T4 sheets. Int. J. Plast. 105, 141-163.

Zecevic, M., Knezevic, M., Beyerlein, I.J., McCabe, R.J., 2016b. Texture formation in orthorhombic alpha-uranium under simple compression and rolling to high strains. Journal of Nuclear Materials 473, 143-156.

Zecevic, M., Knezevic, M., Beyerlein, I.J., Tomé, C.N., 2015. An elasto-plastic self-consistent model with hardening based on dislocation density, twinning and de-twinning: Application to strain path changes in HCP metals. Mater. Sci. Eng. A 638, 262-274.

Zecevic, M., Korkolis, Y.P., Kuwabara, T., Knezevic, M., 2016c. Dual-phase steel sheets under cyclic tension–compression to large strains: Experiments and crystal plasticity modeling. J. Mech. Phys. Solids 96, 65-87.

Zecevic, M., Lebensohn, R.A., McCabe, R.J., Knezevic, M., 2018b. Modeling of intragranular misorientation and grain fragmentation in polycrystalline materials using the viscoplastic self-consistent formulation. Int. J. Plast. 109, 193-211.

Zecevic, M., Lebensohn, R.A., McCabe, R.J., Knezevic, M., 2019. Modelling recrystallization textures driven by intragranular fluctuations implemented in the viscoplastic self-consistent formulation. Acta. Mater. 164, 530-546.

Zecevic, M., Pantleon, W., Lebensohn, R.A., McCabe, R.J., Knezevic, M., 2017b. Predicting intragranular misorientation distributions in polycrystalline metals using the viscoplastic self-consistent formulation. Acta. Mater. 140, 398-410.

Chapter 3: A crystal plasticity finite element model embedding strain-rate sensitivities inherent to deformation mechanisms: Application to alloy AZ31

This chapter was submitted to the International Journal of Plasticity on October 4th 2020 and is currently under review.

My contribution to this work was to work with Dan Savage to implement the K-Mod improvements to the CPFE code along with modernizing the code and making it thread safe. After the code was modified, I preformed the refitting of the code for AZ31 Mg Alloy and accompanying analysis. As part of this refitting I created several automation scripts to run any number of simulations simultaneously and extract the data and create figures. I created all the figures and tables The text was written in a standard student-mentor relationship.

A crystal plasticity finite element model embedding strain-rate sensitivities inherent to deformation mechanisms: Application to alloy AZ31

William G. Feather [a], Daniel J. Savage [a,b], and Marko Knezevic [a,3]

[a] Department of Mechanical Engineering, University of New Hampshire, Durham, NH 03824, USA.

[b] Materials Science and Technology Division, Los Alamos National Laboratory, Los Alamos, NM, 87544, USA.

Abstract

The fundamental power-law relationship representing the flow rule in crystal visco-plasticity ensures uniqueness in the selection of slip systems accommodating imposed plastic strain-rates. The power-law relationship also introduces an artificially high strain-rate sensitivity in crystal plasticity simulations, unless a high value of the power-law exponent is used. However, the use of high values for the exponent is limited by numerical tractability. This paper presents a numerical method implemented in a crystal plasticity finite element (CPFE) model for embedding any value of the power-law exponent reflecting the true material strain-rate sensitivity. Importantly, the method does not increase computation time involved in the simulations. The enhanced CPFE model is used to interpret and predict a complex strain-rate

[3] Corresponding author at:
marko.knezevic@unh.edu (M. Knezevic).

sensitive response and microstructural evolution of AZ31 Mg alloy. Measured values of strain-rate sensitivity for slip and twinning modes are used in the simulations. Calculations show that the model successfully captures the phenomena pertaining to the effect of increasing the strain-rate on the mechanical response including flow stress and evolution of texture and twinning for a broad range of strain-rates ranging from 10^{-3} s^{-1} to 10^{3} s^{-1} and loading orientations in tension and compression. It is shown that such predictions are a consequence of not only relative amounts of slip and twinning activities driven by a set of accurately characterized hardening law parameters but also values of the strain-rate sensitivities inherent to individual deformation mechanisms. Besides, the model validates the measured strain-rate dependency of deformation mechanisms while accurately reproducing the mechanical data. Hence, the model can also be used to either infer or verify strain-rate sensitivity per deformation mechanism by reproducing experimental data.

Keywords: A. Microstructures; B. Elastic-viscoplastic material; B. Rate-dependent material; B. Crystal plasticity; C. Finite elements; T-CPFE UMAT

1. Introduction

The overall constitutive behavior of polycrystals stems from the collective deformation behavior of constituent crystals/grains having local crystal orientation, size, and shape (Kocks et al., 1998). The relationship between the local deformation behavior at the grain-level and that of the polycrystalline aggregate is established using homogenization schemes. To this end, the mean-field (e.g. the Taylor-type or self-consistent (SC)-type (Lebensohn and Tomé, 1993; Wu et al., 2007a)) and the full-field (e.g. the crystal plasticity finite element (CPFE)-type or Green's function fast Fourier transform (FFT)-type (Kalidindi et al., 1992; Lebensohn et al., 2012)) theories are used. The mean-field models are more computationally efficient, while the full-field models are more accurate because they account for local grain-to-grain interactions. An important advantage of the mean-field models is their ability to efficiently handle the crystal lattice reorientation associated with deformation twinning. Several approaches have been developed in the literature for the modeling of twinning within the mean-field models like the predominant twin reorientation model (Tomé et al., 1991; Van Houtte, 1978), total Lagrangian model (Fast et al., 2008; Kalidindi, 1998; Wu et al., 2007a; Wu et al., 2007b), and composite-grain (CG) model (Proust et al., 2007). In contrast, modeling twin lamellae as discrete domains in spatially resolved full-field models has been attempted only recently (Ardeljan and Knezevic, 2018; Ardeljan et al., 2015b; Kumar et al., 2015). However, such models have been primarily used for understanding of the mechanical fields associated with twin lamellae formation rather than for modeling of large plastic deformation of polycrystals (Knezevic et al., 2015).

In the CPFE-type models, a material point can embed a single crystal (Ardeljan et al., 2014; Ardeljan et al., 2015a; Diard et al., 2005; Fernández et al., 2013; Staroselsky and Anand, 2003) or a polycrystal whose response is obtained by a homogenization scheme. Formulations for the

latter approach generally embed either SC models (Segurado et al., 2012; Zecevic et al., 2017) or Taylor models (Ardeljan et al., 2016) at FE integration points. Accordingly, these multi-level models combine the two theories i.e. the FE full-field mechanics technique at a higher level and a mean-field technique at a lower level into a single approach, which takes advantage of both the computational speed of the mean field theories and the accuracy afforded by relaxing homogenization assumptions. In the present work, we adopt the modeling approach incorporating the Taylor-type model at each FE integration point developed in (Ardeljan et al., 2016) and later used in (Feather et al., 2019). The combined multi-level model is referred to as T-CPFE. Importantly, the modeling approach relaxes the iso-strain constraint assumption of the Taylor-type model formulation imposed over the entire polycrystal. Since the polycrystal is distributed over finite elements (i.e. FE integration points), the FE solver interrogates every sub-polycrystal as a separate Taylor-type model at every integration point with an imposed deformation gradient. As the deformation gradient varies spatially based on boundary conditions imposed over the FE mesh, the iso-strain constraint intrinsic to Taylor-type models is relaxed. While the iso-strain constraint assumptions is imposed over the sub-polycrystal embedded at an FE integration point, it is relaxed at the level of the entire polycrystal spanning over the entire FE mesh. The T-CPFE model at the grain-level incorporates the advanced CG twinning model while retaining the original Lagrangian numerical scheme. The twinning model allows multiple twin variants to form per grain. Finally, the model incorporates a dislocation density-based (DD) hardening law for the evolution of slip and twin resistances.

In this paper, the T-CPFE model is advanced to make deformation mechanism-level strain-rate sensitivities computationally feasible, thereby enabling the rate sensitivity behavior of alloy AZ31 to be modeled over a wide range of strain-rates. Since the alloy has a hexagonal closed

packed (HCP) crystal structure and activation stresses vary between deformation modes, its deformation behavior is highly anisotropic (Akhtar, 1973; Partridge, 1967; Yoo, 1981). The plasticity in the alloy is carried out by a combination of crystallographic slip (basal, prismatic, and pyramidal slip modes) and deformation twinning (extension and contraction twinning modes). Activation stresses for these modes depends on strain-rate and temperature (Akhtar, 1975; Akhtar and Teghtsoonian, 1969) and highly varies across the modes inducing strong plastic anisotropy with texture (Ishikawa et al., 2005; Khan et al., 2011; Watanabe and Ishikawa, 2009). Moreover, activity of deformation modes varies with loading paths. As a consequence of such variation, a sheet of AZ31 exhibits strong strain-rate sensitivity during in-plane tension and through-thickness compression, while approximately no strain-rate sensitivity during initial straining in-plane compression. The underlying reason is slip dominated deformation in the former cases and extension twin-dominated deformation in the latter case (Khan et al., 2011; Kurukuri et al., 2014). At higher strain levels, the strain-rate sensitivity for in-plane compression increases due to activation of the multiple slip modes. Such observations reveal that basic deformation mechanisms exhibit different strain-rate sensitivities.

Measurements for alloy AZ31 show that basal slip and twinning modes are approximately independent of strain-rate across a broad range of temperatures with strain-rate sensitivity coefficients of $m^{\alpha=1} = 1 \times 10^{-6}$ for the basal slip mode and $m^{\beta} = 1 \times 10^{-6}$ for the twinning modes (Korla and Chokshi, 2010; Watanabe and Ishikawa, 2009). In contrast, the strain-rate sensitivity coefficients for the prismatic and pyramidal slip modes were estimated to be $m^{\alpha=2} = 2.35 \times 10^{-2}$ and $m^{\alpha=3} = 7.42 \times 10^{-3}$, respectively (Ulacia et al., 2010; Watanabe and Ishikawa, 2009). Despite the fact that these individual values per mode are established, a single coefficient of strain-rate sensitivity for all modes is commonly used in modeling the strain-rate

dependent behaviors of Mg alloys using crystal plasticity. Therefore, current models disregard the distinction of strain-rate sensitivity among different deformation mechanisms. The model in the work of (Wang et al., 2018) utilized a variable strain-rate sensitivity over deformation modes and successfully predicted strain-rate sensitive response of AZ31 over a range of imposed strain-rates; however, the experimentally measured values per deformation mode were still not numerically achieved, limiting the range of imposed strain-rates that the model captured. The development of crystal plasticity models that work for a wide range of imposed strain-rates is very challenging for metals and alloys such as Mg, which have several deformation modes. Low values of strain-rate sensitivity coefficient increase the stiffness of nonlinearity in the governing equations leading to computational failure.

In this paper, numerical robustness of the T-CPFE model is enhanced to consider measured values of strain-rate sensitivity per deformation mode. The developments here are motivated primarily from the fact that many metals exhibit low strain-rate sensitivity and often as function of deformation mode, the case with Mg alloys (Chapuis and Liu, 2019). The motivation also comes from an observation made in (Savage et al., 2017) that void growth-rates in voided cell computations introduce a strain-rate effect in the observed pressure dependence of the material. Such effects should be removed when studying the pressure dependence and comparing to analytical criterion. As such, we seek to implement a robust numerical scheme in the T-CPFE model to eliminate the artificial scaling effect on stress with imposed strain-rate. The implementation relies on the visco-plastic power-law flow-rule, which relates the shearing-rate of a deformation system to the stress resolved on the system plane and in the glide direction (Hutchinson, 1976). The exponent n of the power-law relationship is the deformation system-level equivalent of the inverse of the strain-rate sensitivity coefficient m, which represents the

dependence of the activation stress on strain-rate for fixed τ_c^s. The strain-rate sensitivity of material response *m* is 1/*n* with *n* defined as the slope of the ln-ln flow stress-strain-rate curve (Follansbee and Kocks, 1988; Hosford, 2010), $n = \frac{\partial \ln \dot{\varepsilon}}{\partial \ln \sigma}\Big|_{\varepsilon}$. The value of *n* is a deformation mechanism property, which can be measured experimentally from flow stress curves recorded at different strain-rates for a static i.e. fixed/constant microstructural state. Note that if microstructure evolves then the strain-rate sensitive flow stress is a consequence of a combination of the exponent, n, and evolving $\tau_c^s(\dot{\varepsilon})$.

Grains deforming plastically accommodate strain using a subset of available slip/twin systems. As multiple slip and twinning systems are involved, a sound criterion for activating these systems must be adopted. This can be achieved through the visco-plastic power-law formulism, which introduces strain-rate sensitivity into the deformation physics. In addition to representing the inverse of strain-rate sensitivity, sufficiently high value of the visco-plastic power-law exponent *n* ensures uniqueness in the solution to active slip/twin systems accommodating imposed strains. The distribution of shearing among the systems is collectively referred to as slip/twin activity. Predicting such activity is fundamental to predicting the flow strength and reorientations of the crystals. Due to numerical issues, the exponent *n* used e.g. in visco-plastic SC model is typically 20, which corresponds to *m* = 0.05. The value of *n* = 20 ensures uniqueness in selected deformation systems but much higher values than *n* = 20 are needed to accurately model the actual material strain-rate sensitivity at a constant resistance to slip/twin τ_c^s i.e. constant/static microstructure.

It is important to recognize that the strain-rate sensitivity embedded in the exponent for constant τ_c^s in conjunction with the strain-rate sensitive evolution of slip resistances, τ_c^s, describe strain-

rate sensitive material behavior. The later contribution is described by the thermodynamic theory of slip, which states that dislocation glide is thermally activated in the strain-rate ranging approximately from 10^{-5} s^{-1} to 10^{5} s^{-1} (Kocks et al., 1975; Mecking and Kocks, 1981). Such strain-rate sensitive dislocation glide occurring in every plastically deforming grain in a polycrystal causes the macroscopic flow stress of the polycrystal to depend on strain-rate and temperature (Follansbee, 1986). Crystal plasticity modeling aims to relate the strain-rate sensitive glide of dislocations to the deformation of a grain or set of grains as well as to represent the constant structure strain-rate sensitivity under an imposed strain-rate and temperature conditions. Low values of *n* like 20 – 100 introduce an inaccurate decoupling between the strain-rate sensitive response of constant structure and strain-rate sensitive evolution of τ_c^s i.e. structure evolution. These issues are widely recognized (Kok et al., 2002; Wang et al., 2018; Zecevic et al., 2016) and this work offers a viable solution within T-CPFE.

In this article, a computationally efficient numerical procedure allowing for any value of the exponent governing material strain-rate sensitivity *m* is introduced into T-CPFE following the work involving a SC model presented in (Knezevic et al., 2016) on polycrystalline Cu, which deforms by a single slip mode. The numerical method is termed the *k*-modification (*k*-mod) method. Until this original work, the use of these measured values of strain-rate sensitivity coefficients in crystal plasticity models was limited by numerical tractability i.e. the models were not able to take these measured values of strain-rate sensitivity per deformation mechanism. Taking advantage of these numerical improvements and advances made in the present work, measured values of strain-rate sensitivity per deformation mechanisms are employed in T-CPFE to investigate the strain-rate dependent behaviors of alloy AZ31 at room temperature. It is shown that the strain-rate dependent behavior of the alloy from 10^{-3} s^{-1} to 10^{3} s^{-1} can be accurately

described by an accurate representation of strain-rate sensitivity associated with operative deformation mechanisms. The model accurately predicts flow stress and microstructure evolution for a broad range of strain-rates as a result of not only differing relative amounts of slip and twinning activity driven by a set of accurately characterized hardening law parameters but also deformation mechanism-level strain-rate sensitivities. Accordingly, the evolution of texture, anisotropy, asymmetry, and hardening behavior can be modeled across a wide range of applied strain-rates.

2. Modeling framework

The numerical scheme of the finite deformation crystal plasticity finite element (CPFE) model originally presented in (Kalidindi et al., 1992) is briefly summarized. In particular, the salient parts are outlined so that the proposed extension of CPFE and its implications to the numerical procedure have context. With this goal in mind, the kinematics and constitutive choices are focused on, while dislocation density-based hardening for slip and twinning (Ardeljan et al., 2016) is provided in appendix A. The particular version extended here is the T-CPFE (Ardeljan et al., 2016), which is a multi-level model linking the macro FE level at the highest scale and the Taylor-type polycrystalline model constitutive response at an integration point wherein the lowest level response of individual grains driven by slip/twinning is homogenized. The T-CPFE is implemented in finite element software ABAQUS as a user material subroutine (UMAT). The implicit finite element solver iteratively provides a best guess at time, τ (t+Δt), of the deformation gradient, **F**, for each gauss integration point in the finite elements based on the boundary conditions of the FE model. A set of state variables for each grain such as dislocation density for slip systems and twin volume fraction for each twin variant per grain is available from the previous increment, t. The UMAT updates the state variables, returns the volume

average Cauchy stress, $\bar{\boldsymbol{\sigma}}$, and returns the Jacobian (i.e. the mapping between change in Cauchy stress components with respect to each component of the logarithmic strain) at the integration point. If the principles of virtual work are satisfied (boundary conditions and stress equilibrium), the solver moves on to the next time increment, otherwise the state variables are reset to the last converged state, and the updated Jacobian is used to create a new guess for the deformation gradient. Note that the Jacobian changes rate of convergence and whether convergence is achieved, but does not affect the solution. The following notation is utilized: tensor quantities are bold; tensor components and scalars are italic and not bold; indices *s*, α, *t*, and β denote slip systems, slip modes, twin systems, and twin modes, respectively; $\cdot$ is a dot product; and $\otimes$ is a tensor product.

2.1 Overview of CPFEM

Since each FE integration point may be a polycrystal due either to twinning or including multiple grains (i.e. a Taylor polycrystalline aggregate), the Cauchy stress is taken as a volume average of crystal stresses at the integration point

$$\bar{\boldsymbol{\sigma}} = \langle \boldsymbol{\sigma} \rangle = \sum_{k=1}^{N_{grains}} v_k \boldsymbol{\sigma}_k \,, \tag{1}$$

where the sum of grain volume weights, v, is unity and $\langle\ \rangle$ denote the volume average.

The weighted grains embedded at an FE integration point undergo the same applied deformation gradient, **F**, which is the intrinsic assumption of the Taylor model. The multiplicative decomposition of **F** leads to its plastic and elastic portions as

$$\mathbf{F} = \mathbf{F}^e \mathbf{F}^p. \tag{2}$$

In this decomposition, the intermediate configuration is plastically deformed by $\mathbf{F}^p$ and is stress-free meaning that the crystal lattice remains aligned with that in the undeformed configuration. The lattice stretch and rotation is accounted by $\mathbf{F}^e$. The rate of change of $\mathbf{F}^p$ is

$$\dot{\mathbf{F}}^p = \mathbf{L}^p\mathbf{F}^p, \tag{3}$$

which after the integration from the time at the beginning of the strain increment, *t*, to the end of the increment, $\tau = t+\Delta t$, is

$$\mathbf{F}^p(\tau) = exp(\mathbf{L}^p\Delta t)\mathbf{F}^p(t). \tag{4}$$

The grain stress-strain relationship is

$$\mathbf{T} = \mathbf{C}\mathbf{E}^e, \text{ with } \mathbf{T} = \mathbf{F}^{e^{-1}}\boldsymbol{\tau}\mathbf{F}^{e^{-T}} = \mathbf{F}^{e^{-1}}\{(det\mathbf{F}^e)\boldsymbol{\sigma}\}\mathbf{F}^{e^{-T}} \text{ and } \mathbf{E}^e = \frac{1}{2}\left\{\mathbf{F}^{e^T}\mathbf{F}^e - \mathbf{I}\right\}, \tag{5}$$

where, $\mathbf{C}$ is the fourth-order elasticity tensor, $\mathbf{T}$ is the second Piola-Kirchhoff stress, which is the pull-back from current configuration of the contravariant Kirchoff stress $\boldsymbol{\tau}$ (also known as the weight Cauchy stress) , and $\mathbf{E}^e$ is the Lagrangian strain. The elasticity stiffness tensor per grain is calculated based on the single-crystal elastic constants for Mg: C_{11} = 59,500 MPa, C_{12} = 26,100 MPa, C_{13} = 21,800 MPa, C_{33} = 65,600 MPa, C_{44} = 16,300 MPa (Slutsky and Garland, 1957). In order to calculate the stress, $\mathbf{F}^e$ must be known from $\mathbf{F}^e = \mathbf{F}\mathbf{F}^{p^{-1}} = \mathbf{F}\mathbf{F}^{p^{-1}}(t)\{\mathbf{I} - \Delta t\mathbf{L}^p\}$. In order to evaluate $\mathbf{L}^p$, the applied velocity gradient tensor, $\mathbf{L}$, corresponding to $\mathbf{F}$, is additively decomposed to its elastic part, $\mathbf{L}^e$, and plastic part, $\mathbf{L}^p$. The plastic part accounts for plasticity due to slip and twinning. These kinematics equations are

$$\mathbf{L} = \mathbf{L}^e + \mathbf{L}^p = \mathbf{L}^e + \mathbf{L}^{sl} + \mathbf{L}^{tw} = \mathbf{L}^e + \sum_s^{N^{sl}}\dot{\gamma}^s\mathbf{S}_0^s + \sum_t^{N^{tw}}\dot{f}^t S^t\mathbf{S}_0^t, \tag{6}$$

where $\mathbf{S}_0^s = \mathbf{b}_0^s \otimes \mathbf{n}_0^s$ and $\mathbf{S}_0^t = \mathbf{b}_0^t \otimes \mathbf{n}_0^t$ are reference Schmid tensors for slip and twinning systems *s* and *t*, respectively, $\dot{\gamma}^s$ is the rate of shearing, S^t is the twin system shear strain, and

$\dot{f}^t = \frac{\dot{\gamma}^t}{S^t}$ is the rate of twin volume fraction evolution, which is the pseudo-slip model (Kalidindi, 1998; Van Houtte, 1978). The Schmid tensors are based on the geometry of slip/twin system vectors, $\mathbf{b}_0^s$ and $\mathbf{b}_0^t$ are Burgers vectors and $\mathbf{n}_0^s$, and $\mathbf{n}_0^t$ are plane normal vectors. These vectors are time independent i.e. are in the reference configuration, 0. N^{sl} and N^{tw} are total number of slip and twin systems.

The standard power-law relationship of crystal visco-plasticity can be used to calculate the shear strain-rates for slip and twinning, $\dot{\gamma}^s$ and $\dot{\gamma}^t$, (Asaro and Needleman, 1985; Hutchinson, 1976; Kalidindi, 1998). Since the equation is equivalent for slip and twinning, for slip systems *s*, it is

$$\dot{\gamma}^{s} = \dot{\gamma}_0 \left(\frac{|\tau^{s}|}{\tau_c^{s}(\dot{\varepsilon}, T)} \right)^{\frac{1}{m}} \mathrm{sign}(\tau^{s}), \tag{7}$$

where the resolved shear stress is calculated using $\tau^s = \mathbf{T} \cdot \mathbf{S}_0^s$, τ_c^s is the slip systems resistance, $\dot{\gamma}_0$ is the reference shearing rate used to scale the applied strain-rate ($\dot{\gamma}_0 = 0.001\ \mathrm{s}^{-1}$), and m is the strain-rate sensitivity. The power-law exponent, $\frac{1}{m} = n$, must be sufficiently high to ensure proper selection of slip/twin systems and, at the same time, should not introduce any extraneous *constant structure* (i.e. constant τ_c^s) strain-rate sensitivity. The latter is recognized as a significant issue when attempting to simulate high strain-rate deformation using crystal visco-plasticity models (Knezevic et al., 2016; Zecevic et al., 2016). The strain-rate sensitivity introduced by the power-law relation reduces as *n* increases. The strain-rate sensitivity embedded in the exponent should not be confused with the strain-rate sensitive evolution of slip resistances, τ_c^s, as described by the thermodynamics of slip (Follansbee and Kocks, 1988; Kocks et al., 1975). The evolution of slip/twin resistances, τ_c^s, originates from the *evolving structure*. The aim of the present work is both to relate the strain-rate sensitive glide of dislocations to the deformation of a

grain or set of grains (see the hardening law appendix A) and to represent the constant structure strain-rate sensitivity under an imposed strain-rate, as detail below.

2.2 Computationally efficient representation of strain-rate sensitivity per slip/twin mode using the k-modification (k-mod) method

The power-law visco-plasticity theory has proven effective in determining the single crystal yield surfaces of materials with many potential slip/twin systems. However, the power exponent also controls the strain-rate sensitivity of the response such that for $n \to \infty$, the shear-rates and stress become rate insensitive; however, increasing n above 100 is not computationally attractive since the simultaneous equations in $\boldsymbol{T}$ and τ_c^s becomes too stiff to solve numerically or take a prohibitive number of iterations (Knezevic et al., 2016). Conversely, if n is too small ($n < 20$), the selection of active slip systems is affected.

The symmetric part of $\mathbf{L}^p$ is the plastic rate of stretching tensor

$$\mathbf{D}^p = \frac{1}{2}\left(\mathbf{L}^p + \mathbf{L}^{pT}\right), \tag{8}$$

which is deviatoric, and an equivalent strain-rate to it is $\dot{\varepsilon} = \sqrt{\frac{2}{3}\mathbf{D}^p \cdot \mathbf{D}^p}$. The same rate of stretching is applied to every crystal, *c*, in a Taylor polycrystal, i.e.

$$\mathbf{D} = \left\langle \mathbf{D}^c \right\rangle = \mathbf{D}^c, \tag{9}$$

with

$$\mathbf{D}^{p,c} = \sum_s \dot{\gamma}^{s,c} \mathbf{P}^{s,c}, \tag{10}$$

where $\mathbf{P}_0^{s,c} = \frac{1}{2}\left(\mathbf{S}_0^{s,c} + \left(\mathbf{S}_0^{s,c}\right)^T\right)$ is the symmetric part of the Schmid tensor for crystal *c*. The superscript *c* will be omitted from writing in the crystal equations that follow. In case the applied rate of stretching is scaled by λ, Eq. (10) and Eq. (7) lead to

$$\lambda \mathbf{D}^p = \lambda \dot{\gamma}_0 \sum_s \mathbf{P}^s \left(\frac{\left| \mathbf{T} \cdot \mathbf{P}_0^s \right|}{\tau_c^{\ s}} \right)^n \operatorname{sgn}\left(\mathbf{T} \cdot \mathbf{P}_0^s \right) = \dot{\gamma}_0 \sum_s \mathbf{P}^s \left(\frac{\left| \lambda^{\frac{1}{n}} \mathbf{T} \cdot \mathbf{P}_0^s \right|}{\tau_c^{\ s}} \right)^n \operatorname{sgn}\left(\lambda^{\frac{1}{n}} \mathbf{T} \cdot \mathbf{P}_0^s \right). \tag{11}$$

For constant τ_c^s, the equation on the right governs a strain-rate sensitive response that scales inversely with *n*. Evidently, the stress is scaled as $\lambda^{\frac{1}{n}}\mathbf{T}$, and raising n has the effect of removing the strain-rate sensitivity, i.e. $\lim_{n\to\infty} \lambda^{\frac{1}{n}} = 1$. Fig. 1 shows the effect of the power-law exponent of *n* = 20 (strain-rate sensitivity of *m* = 0.05) on stress-strain response of the alloy AZ31 in simple tension as a function of imposed strain-rate, $\dot{\varepsilon}$ (i.e. the scaling of the applied rate of stretching like $\lambda \mathbf{D}^p$). The reference shearing rate was constant, $\dot{\gamma}_0 = 0.001\ \mathrm{s}^{-1}$. The same value of *n* is used for every deformation mode, α and β. As is evident, the standard power-law equation of the visco-plasticity theory requires a correction to remove the superfluous strain-rate sensitivity that is introduced with inaccurately low values of *n* (i.e. high values of *m*).

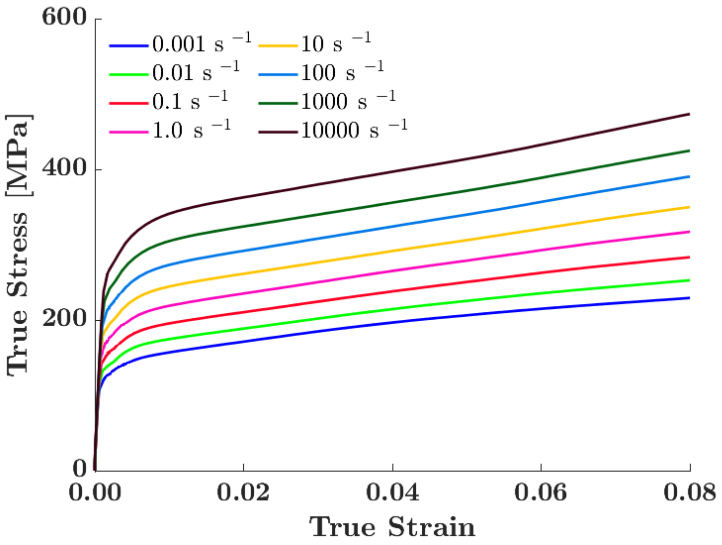

Figure 1. Effect of the power-law exponent of n = 20 on the alloy AZ31 response in simple tension as a function of imposed strain-rate as indicated in the legend. The same value of n is used for every deformation mode α and twin mode β.

The complexity for finding the solution of crystal stress given an imposed deformation scales with increasing value of the power-law exponent *n*. The value of *n* representative for strain-rate sensitive behavior of many metals is difficult to achieve numerically. Commonly used Newton-Raphson (NR) solution procedures converge for *n* in the range up to $n = 50$. Modified NR solution procedures are required to reach to about $n = 100$. As mentioned, for most metallic materials, such as stainless steel and Cu, the value of *n* needs to be significantly greater in order to capture their strain-rate sensitive response (Chen and Gray, 1996; Follansbee and Kocks, 1988; Hosford, 2010; Knezevic et al., 2013a; Knezevic et al., 2016). Modified NR procedures often encounter convergence problems for $n > 100$. As a result of $n > 100$, the non-linear equations turn out to be extremely stiff and prohibitively challenging to solve for stress. A way to achieve values of *n* representative of the strain-rate sensitivity of actual metallic materials numerically is adding an additional solution procedure loop to incrementally increase *n*. To this end, an obtained solution for a given *n* is used as a guess to calculate the next solution

corresponding to a higher *n*. Such a solution procedure is computationally prohibitive and unpractical.

Another approach consists of eliminating the strain-rate sensitive response by embedding the norm of an applied rate of stretching, $\left|\mathbf{D}^p\right|$, into the reference shear rate, $\dot{\gamma}_0$. The approach makes the model strain-rate insensitive. A change in the magnitude but not sense of the applied rate of stretching, $\lambda\mathbf{D}^p$, will not change stress provided that τ_c^s is constant with strain-rate because $\dot{\gamma}_0 = \left|\lambda\mathbf{D}^p\right|$. The typical value of *n* used in this approach is *n* = 20, which ensures the proper selection of slip/twin systems and is efficient. The approach was used in many prior studies (Feather et al., 2019; Knezevic et al., 2013d; Kok et al., 2002). However, in addition to not capturing strain-rate sensitive response of materials, this approach has another major issue when attempting to implement it into FEM (Knezevic et al., 2013b; Knezevic et al., 2013c; Segurado et al., 2012; Zecevic et al.; Zecevic et al., 2015). Since the stress is no longer a function of $\left|\mathbf{D}^p\right|$ but a function of four components of the normalized rate of stretching $\frac{\mathbf{D}^p}{\left|\mathbf{D}^p\right|}$, the solution for stress has dependent components. The Cauchy stress required by Abaqus will only have five (not six) independent components.

A solution to this problem allowing any value for the strain-rate sensitivity while being computationally efficient is a so-called the *k*-mod method (Knezevic et al., 2016), which is summarized in the remainder of this section. The method is implemented in the T-CPFE model per deformation mode to model the strain-rate sensitive behavior of alloy AZ31.

The key component of the *k*-mod method is an appropriate modification of the applied rate of stretching at every FE integration point before evaluating the constitutive function for stress at

the grain level. Specifically in place of any applied rate of plastic stretching denoted now by $\mathbf{D}^{p,app}$, we use a modified rate of stretching, $\mathbf{D}^{p}$, to solve for stress

$$\mathbf{D}^{p} = \frac{\mathbf{D}^{p,app}}{\left|\mathbf{D}^{p,app}\right|}\left|\mathbf{D}^{p,app}\right|^{\frac{1}{k+1}} . \tag{12}$$

As *k* increases, the norm of $\mathbf{D}^{p}$ approaches unity. The inverse relationship is $\mathbf{D}^{p,app} = \mathbf{D}^{p}\left|\mathbf{D}^{p,app}\right|^{\frac{k}{k+1}} = \mathbf{D}^{p}\left|\mathbf{D}^{p}\right|^{k}$. Thus, the norm of $\mathbf{D}^{p}$ is the $(k+1)^{\text{th}}$ root of $\mathbf{D}^{p,app}$. Note that powers and norms do not apply to the units but only to the values. Because $\mathbf{D}^{e}$ is small for a plasticized grain, whether we modify the plastic $\mathbf{D}^{p,app}$ or the total $\mathbf{D}^{app}$ in Eq. (12), results are not appreciably different. Since evaluating $\mathbf{D}^{p,app}$ requires an additional loop for the implicit integration, we elect to use $\mathbf{D}^{app}$ in order to avoid the computational cost associated with the third loop. The rate of deformation tensor $\mathbf{D}^{app}$ is provided as an Abaqus UMAT variable. As a result, the *k*-mod method introduces the following scaling to the stress while governing the amount of strain-rate sensitivity

$$\frac{\lambda\mathbf{D}^{app}}{\left|\lambda\mathbf{D}^{app}\right|}\left|\lambda\mathbf{D}^{app}\right|^{\frac{1}{k+1}} \approx \lambda^{\frac{1}{k+1}}\mathbf{D}^{p} = \dot{\gamma}_0 \sum_s \mathbf{P}_0^s \left(\frac{\left| \lambda^{\frac{1}{(k+1)n}} \mathbf{T}\cdot\mathbf{P}_0^s \right|}{\tau_c^{\,s}} \right)^n \operatorname{sgn}\left(\lambda^{\frac{1}{(k+1)n}} \mathbf{T}\cdot\mathbf{P}_0^s \right). \tag{13}$$

The equation states that if the applied rate of stretching is arbitrarily altered to $\lambda\mathbf{D}^{app}$, the *k*-mod method modifies the rate of stretching from $\mathbf{D}^{p}$ to $\lambda^{\frac{1}{k+1}}\mathbf{D}^{p}$. As a consequence, the grain stresses, $\mathbf{T}$ i.e. $\boldsymbol{\sigma}$ scales according to $\lambda^{\frac{1}{(k+1)n}}\boldsymbol{\sigma}$ and, as a result, the homogenized macroscopic stress scales

according to $\lambda^{\frac{1}{(k+1)n}}\bar{\boldsymbol{\sigma}}$. Note that, the scaling in Eqs. (11) and (13) has the same form, but in the former case the scaling is only by *n* ($\lambda^{\frac{1}{n}}\mathbf{T}$), while in the latter case by a combination of *n* and *k* ($\lambda^{\frac{1}{(k+1)n}}\mathbf{T}$). It should also be noted that the increase in *k* affects the scaling of the stretching and stress tensors but does not affect the relative contribution of active slip/twin systems. Selection of slip/twin systems and the strain-rate direction are defined only by *n*.

Grain stress solutions are different with *n* or with a combination of *n* and *k* as seen from Eqs. (11) and (13), respectively. To appreciate this scaling of the stress, consider the same scaling of the applied strain-rate (i.e. the rate of stretching $\lambda\mathbf{D}^p$) as in Fig. 1, while keeping the constant value for the reference shearing rate, $\dot{\gamma}_0 = 0.001\ \mathrm{s}^{-1}$. In the *k*-mod approach, any value of a strain-rate sensitivity as the material property can be realized by a combination of *n* and *k*. It is convenient to set *n* = 20 because it ensures proper selection of slip/twin systems and is computationally efficient, while only vary *k*. The scaling is demonstrated by rerunning the simulations from Fig. 1 after setting $k = 19$ and keeping $n = 20$ (i.e. (*k* + 1)*n* = 400). The curves from Fig. 1 converge to a strain-rate sensitive response of *m* = 0.0025 in Fig. 2. The sensitivity of 0.0025 is typical for Cu (Follansbee, 1986) and many steels (Poulin et al., 2019). It should be noted that the exponent of 400 can also be achieved either by *n* = 400 and *k* = 0 or another combination of *n* and *k* like *n* = 50 and *k* = 7. These would produce the same results but would not be as efficient as the combination of *n* = 20 and *k* = 19 because the computational time to solve for the stress given the rate of stretching increases with *n* to 50 or to 400 but remains the same with increase in *k*. Changing the value of *k* does not influence the time to solving the power-law with a given value of *n*. Importantly, different combinations of *n* and *k* can be used per slip/twin mode governing their individual strain-rate sensitivities.

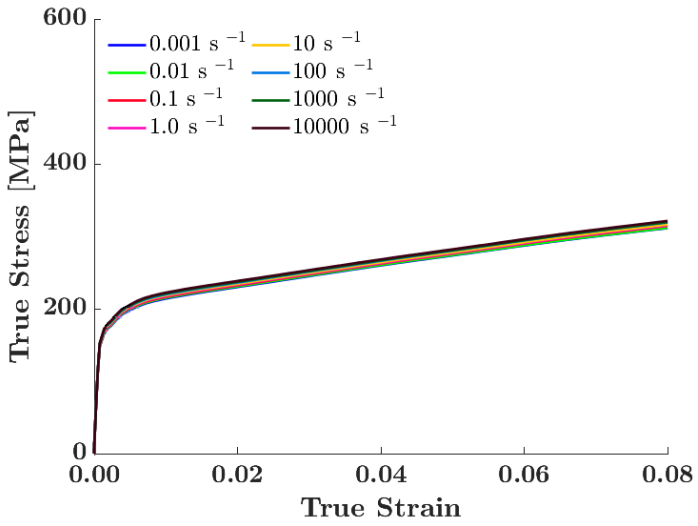

Figure 2. Effect of the power-law exponent of n = 20 and k = 19 on the alloy response in simple tension as a function of imposed strain-rate as indicated in the legend. The k-mod formulation of n(k + 1) = 400 acheves approximatelly a strain-rate insensitive response, which corresponds to the imposed strain-rate of 1.0. The same values of n and k are used for every deformation mode, α and β.

As the *k*-mod method alters the rate of plastic stretching accommodated by grains from $\mathbf{D}^{p,app}$ to $\mathbf{D}^{p}$, to ensure that the grains actually accommodate the applied rate of stretching, $\mathbf{D}^{p,app}$, the calculated shearing rates scale using

$$\mathbf{D}^{p,app} = \frac{\left|\mathbf{D}^{app}\right|}{\left|\mathbf{D}^{app}\right|^{\frac{1}{k+1}}} \sum_s \mathbf{P}_0^s \dot{\gamma}^s = \sum_s \mathbf{P}_0^s \dot{\gamma}_{k-\mathrm{mod}}^s \quad , \tag{14}$$

such that the shearing rates are normalized in CPFE as

$$\dot{\gamma}_{k-\mathrm{mod}}^s = \frac{\left|\mathbf{D}^{app}\right|}{\left|\mathbf{D}^{app}\right|^{\frac{1}{k+1}}} \dot{\gamma}_0 \left(\frac{\left|\mathbf{T}\cdot\mathbf{P}_0^s\right|}{\tau_c^{\,s}} \right)^n \mathrm{sgn}\left(\mathbf{T}\cdot\mathbf{P}_0^s\right). \tag{15}$$

Finally, as the Jacobian matrix plays a central role in the rate of convergence of the equilibrium governing equation in the FE framework (Bathe, 1996), a modification to the analytical CPFE

Jacobian matrix due to the *k*-mod implementation is implemented. The overall Jacobian matrix is defined as a derivative of the Cauchy stress tensor with respect to the logarithmic strain tensor provided by ABAQUS. The matrix revises the deformation field at each FE integration point in order to iteratively satisfy the principle of virtual work using the Newton-type implicit FE iterations (Anand, 2004; Delannay et al., 2003). To accommodate the *k*-mod, the modification pertains to the relationship between $\dot{\gamma}^s_{k-\text{mod}}$ and $\mathbf{T}$ i.e. $\frac{\partial \Delta\gamma^s_{k-\text{mod}}}{\partial T_M}$ as follows

$$\frac{\partial \Delta\gamma^s_{k-\text{mod}}}{\partial T_M} = \left|\mathbf{D}^{app}\right|^{\frac{k}{k+1}} \frac{\partial \Delta\gamma^s}{\partial T_M} \tag{16}$$

where $\frac{\partial \Delta\gamma^s}{\partial T_M}$ is computed as in the original model. If the plastic $\mathbf{D}^{p,app}$ were modified in Eq. (13) instead of the total $\mathbf{D}^{app}$, an analytical form for the derivative $\frac{\partial \mathbf{D}^{p,app}}{\partial \mathbf{T}}$ would be involved in Eq. (16) and would introduce a matrix inversion operation, which is computationally expensive. We have determined that the use of $\mathbf{D}^{app}$ has a negligible impact on accuracy, even in applications with rapid fluctuations of applied strain-rates such as in Taylor cylinder impact simulations.

In closing this section, we mention that while modifying the T-CPFE model for the inclusion of the *k*-mod method, we enabled the uses of threaded parallelization in the code, while still maintaining the option to uses MPI parallelization. Threaded parallelization is a shared memory parallelization method where all parallel workers or 'threads' have access to all the variables all of the time. As opposed to MPI parallelization where each parallel worker or 'process' has its own copy of all the variables that only it has access to. This does not have inherent performance improvements but in an application such as CPFE where there are several arrays that are of size

(# elements, # integration points, # of crystals per integration) this reduces the number of duplicates of these potentially very large arrays which is required for each MPI process. To quantify the benefit of this change a 64 element model with 6 grains embedded at each integration point was run with each version of the code, with 16 CPUs each. The memory usage of this simulation was 6.68 GB for the old MPI only version of the model, and 0.70 GB for the threaded parallelization version. This is about a 90% decrease in memory requirements, enabling the use of larger element count models. A computer workstations of Intel(R) Xeon(R) Gold 6130 CPU @ 2.10 GHz with 32 physical cores and 772 GB RAM was used to perform the simulations in this work.

3. Experimental data

Experimental data utilized in the present work are taken from (Kurukuri et al., 2014) for a rolled sheet of alloy AZ31B (3.0% Al, 1.1% Zn, 0.49% Mn) in the *annealed* condition (O-temper) with equiaxed grains and a 12 μm average diameter. Pole figures showing the initial texture in the sheet are shown in Fig. 3. The sheet exhibits a typical, strong basal texture with the majority of grains in the sheet being oriented with their crystallographic ***c***-axes along the sheet normal direction (ND). There is more spreading/tilting in the rolling direction (RD) compared to the transverse direction (TD). The sense of loading (tension, compression) and orientation of loading (RD, TD, ND) relative to the initial crystallographic texture govern the activity of deformation mechanisms accommodating the plasticity.

In the work of (Kurukuri et al., 2014), the alloy was tested under strain-rates ranging from 10^{-3} s^{-1} to 10^{3} s^{-1} at room temperature. To characterize the effect of sheet orientation and strain-rate on flow stress anisotropy and tension/compression asymmetry, the strain-rate sensitive flow stress was measured in tension along the RD, 45°, and TD and in compression along the RD,

45°, TD, and ND. Fig. 4a shows that the in-plane (RD) flow stress in compression is approximately strain-rate insensitive for the early portion of deformation. As the compressive deformation proceeds, the material starts to exhibit increasingly strain-rate sensitive behavior. The material is much stronger in compression along ND relative to the in-plane compressive loading. The ND compressive response exhibits some strain-rate sensitivity in terms of the initial yield strength. However, the rate of strain hardening increases for higher strain-rate loading. Under loading in tension, the alloy exhibits strong strain-rate sensitivity, which is approximately constant throughout the deformation. The alloy exhibits pronounced tension/compression asymmetry that increases with strain-rate.

The strain-rate sensitivity under tension and compression along three in-plane orientations (RD, 45°, and TD) is further illustrates in Fig. 4b, in which true stress vs. strain-rate from 10^{-3} s^{-1} to 10^{3} s^{-1} is plotted for the strain levels of 0.02 and 0.08. The figure first shows that the material exhibits mild in-plane anisotropy with the TD direction being the strongest. The RD is the least strong. Looking at the texture (Fig. 3), such behavior is expected since there is slightly more grains tilted with their **c**-axis towards RD than TD. The data further shows that there is a clear increase in strength with the strain-rate in all the three tested directions in tension. Interestingly, the trend lines for tension along the three direction show similar slope at both strain levels. The figure also reveals that the degree of tension/compression asymmetry increases with strain-rate, primarily at low strain levels. This is because the in-plane compressive response is approximately strain-rate insensitive at low strains (0.02). The low slope of the trend lines clearly indicates this. At higher strains (0.08), the compressive strain-rate sensitivity is strong. The trend lines indicate comparable or even higher slope than that in tension. Rapid hardening in compression makes the compressive strength exceed the tensile strength with plastic strain.

The complex behavior of the alloy with strain and strain-rate is attempted to be interpreted here using the enhanced T-CPFE model, which incorporates the true values of strain-rate sensitivity of individual deformation mechanisms that activate as a function of texture, loading sense. The measured values of strain-rate dependency of individual deformation mechanisms will be validated, while predicting the comprehensive mechanical data.

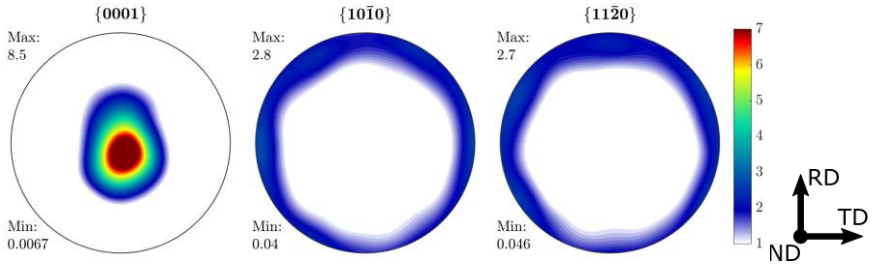

Figure 3. Pole figures showing the initial measured texture of the alloy. Measured texture using electron backscattered diffraction (EBSD) over a large area is compacted to 3,072 crystal orientations for simulations. Pole figures of the initial texture used in the simulations are indistinguishable from the measured ones depicted in the figure and are not shown.

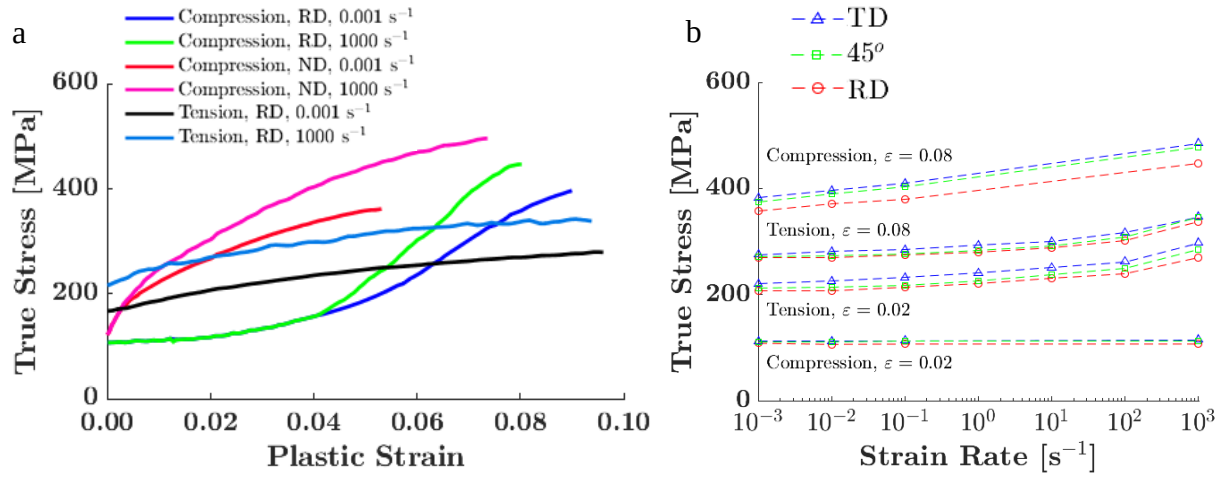

Figure 4. (a) True stress-plastic strain response of annealed alloy AZ31B-O Mg sheet in compression and tension along the rolling direction (RD) and in compression along the normal direction (ND) at room temperature as a function of strain-rate. (b) True stress versus strain-rate (logarithmic scale) trend lines at two strain levels (0.02 and 0.08) for the sheet deformed in simple compression and tension along the three in-plane direction (RD, 45°, and TD). The symbols are measuring points. The data is taken from (Kurukuri et al., 2014).

4. Results

Simulations were performed using a simple cubical cell consisted of 64 continuum three-dimensional eight-nodal (C3D8) elements. Simple tension/compression boundary conditions were prescribed by specifying displacements along the loading direction while ensuring the stress-free conditions on the lateral faces (Jahedi et al., 2015). The imposed strain-rate in each simulation was consistent with the experiment and the only change from test to test is the strain-rate and prescribed loading direction. The initial texture was represented using 3,072 equally weighted crystal orientations to initialize the model. A Taylor sub-polycrystal consisted of 6 grains was embedded at each integration point via a random assignment. Every orientation is allowed to develop multiple twin variants and, therefore, the number of orientations at each integration point can increase with plastic strain very quickly. Four stress-strain curves were used in fitting of the model parameters for AZ31 while calculating the stress-strain response. Two remaining curves as well as the evolution of texture and twinning can be regarded as predictions.

In the simulations, basal **a** $\{0001\}\langle\bar{1}\bar{1}20\rangle$, prismatic **a** $\{\bar{1}100\}\langle\bar{1}\bar{1}20\rangle$, and pyramidal **c**+**a** $\{10\bar{1}1\}\langle\bar{1}\bar{1}23\rangle$ or type I and $\{\bar{1}\bar{1}22\}\langle\bar{1}\bar{1}2\bar{3}\rangle$ or type II slip modes and **c**-axis extension $\{10\bar{1}2\}\langle\bar{1}011\rangle$ (TTW) and **c**-axis contraction $\{10\bar{1}1\}\langle10\bar{1}\bar{2}\rangle$ (CTW) twin modes were made available. In addition, secondary twinning facilitating a common double twinning sequence $\{10\bar{1}1\}-\{10\bar{1}2\}$ (DTW) was allowed to operate. The TTW accommodates a shearing strain of 0.1289, while reorienting the crystal orientation of the twinned domain for about 86^o about the $\langle11\bar{2}0\rangle$ direction. The CTW produces a shear of 0.1377, while reorienting the crystal orientation of the twinned domain for about 56^o about the $\langle11\bar{2}0\rangle$ direction (Yoo, 1981). While the TTW are fast growing and thick (Al-Samman and Gottstein, 2008; Barnett, 2007a), the CTW are thin (Al-Samman and Gottstein, 2008; Barnett, 2007b; Knezevic et al., 2010). The morphology of the

latter twins is due to the creation of an TTW within the primary CTW lamella hindering its growth. The hardening law parameters are adjusted so that the slip/twin resistances evolve to provide the appropriate ratios of active deformation modes for predictions of stress-strain, texture, and twinning.

Fig. 5 compares measured and simulated true stress–true strain responses for the alloy in compression and tension along the RD and in compression along the ND at room temperature under two strain-rates (10^{-3} s^{-1} and 10^{3} s^{-1}). The figure illustrates that the model successfully captures the phenomena pertaining to the effect of increase in the strain-rate on mechanical response using a single set of hardening parameters (Table 1). The hardening parameters were adjusted for the selected T-CPFE homogenization scheme, the CG twinning model, and the selected hardening law to reproduce the experimental data. Despite the relaxed Taylor assumptions afforded by the T-CPFE model, the Talor-type homogenization over 6 single crystals and their twins can still suffer from over or under activation of deformation mechanisms due to the geometric constraint. This effect primarily results in the case of this AZ31 alloy in a lower basal slip resistance and larger ratio between basal and other between slip modes when compared to other homogenization methods which better approximate the matrix constraint (Barnett, 2003; Tomé, 1999). The simulations are based on the measured values of strain-rate sensitivity per deformation mode (Table 2). In particular, approximately strain-rate independent response is predicted for the in-plane compression to strains less than ~0.04, whereas the increasing strain-rate sensitivity is predicted for strains greater than ~0.04. The higher strength in compression along ND relative to the in-plane compression and, in particular, the increase in the rate of strain hardening with strain-rate for the ND compression are predicted well. The strong and approximately constant strain-rate sensitivity with plastic strain is predicted well under

loading in tension. As a consequence of the different strain-rate sensitivity exhibited by the material in tension vs compression, the pronounced tension/compression asymmetry increases with strain-rate, which is also predicted well by the model.

Fig. 6 shows the predicted relative activities of deformation mechanisms accommodating plastic deformation of the alloy under the deformation conditions corresponding to Fig. 5. The activity plots include the activity in the parent and the twinned domains. The model adjusts deformation mechanisms accommodating the plastic strain based on the evolution of slip/twin resistances in order to predict the deformation behavior of the alloy. The typical sigmoidal upwards shape of the curves recorded under compression in RD is indication of profuse twinning in the first stages of deformation. Deformation by profuse extension twinning is followed by rapid strain-hardening owing to the subsequent activation of non-basal slip systems. The origin of such hardening is in the crystal lattice reorientation in the twinned domains. The twinned domains are harder than the parent orientation with respect to the loading direction (Asgari et al., 1997; Knezevic and Beyerlein, 2018; Knezevic et al., 2012). Hard pyramidal slip systems activate in the twinned domains (Clausen et al., 2008; Jain and Agnew, 2007; Lentz et al., 2015; Lou et al., 2007; Proust et al., 2009b; Risse et al., 2017). In addition, twins subdivide parent grains giving rise to the barrier Hall-Petch-like hardening effect (Asgari et al., 1997; Bouvier et al., 2012; Kaschner et al., 2007; Proust et al., 2007). The mechanism of barrier hardening is understood in terms of dislocations accumulating in the vicinity of the grain/twin interfaces. The alloy AZ31 is known to exhibit a variation in the Hall-Petch slope (Barnett et al., 2004; Yuan et al., 2011). This is an indication that the barrier effect should be associated with deformation systems, as is done in the present work. The values are fit for grains containing twins to reproduce the macroscopic true stress-true strain curves, while the grain size effect in embedded in the initial resistances. To

this end, extension twins cause small barrier as reflected by small values of H_1^{α} because they grow quickly and dislocations can easily be transmitted (Molodov et al., 2017). As a result, the initial plateau in the stress-strain response arises. In contrast, contraction twins create a large barrier effect hardening (Knezevic et al., 2010), as reflected by large values of H_2^{α}. These contraction twins are very thin as they often develop extension twins, which is a commonly observed double twinning sequence (DTW). This trend of the CTW and DTW having higher barrier term values that the TTW is in agreement with experimental observations that the CTW/DTW effectively restrict the mean free path of pyramidal dislocations (Ardeljan et al., 2016; Knezevic et al., 2010). Some hardening due to twinning could arise from the so called Basinski-mechanism, which has to do with the transmutations of stored dislocations from the parent grain to the twinned domain (Basinski et al., 1997). However, this mechanism is small in Mg alloys since twins develop early in the deformation when the level of dislocation density in grains is low (El Kadiri and Oppedal, 2010; Knezevic et al., 2010). The in-plane tensile response is a consequence of prismatic slip primarily, while the ND compression response is a consequence or pyramidal slip and contraction twinning. The decreasing hardening rates recorded in tension and ND compression indicate the slip dominated deformation. As already elaborated, the CTW causes significant barrier effect hardening to pyramidal slip.

TTW plays a significant role in texture evolution during in-plane compression. Fig. 7 and Fig. 8 show predicted twin volume fractions and texture evolution, respectively. These results are consistent with many measurements from the literature like (Chun and Davies, 2011; Knezevic et al., 2010; Proust et al., 2009a). TTW and basal slip explain the texture formation in compression. The activity of prismatic and pyramidal slip increases with plastic strain to cooperate with the basal slip activity. These slip modes activate within extension twin domains and are responsible

for hardening because the pyramidal slip is hard in particular. The cooperative action of prismatic and basal slip explain the texture formation in tension and pyramidal and basal slip explain the texture formation in ND compression. The activity of twinning in ND compression and in plane tension is small. In general, the activities at 10^{-3} s^{-1} and 10^{3} s^{-1} are similar but as such are still in the origin of the strain-rate sensitive deformation behavior of the alloy. The major difference is that there is a little more twinning at 10^{3} s^{-1} than at 10^{-3} s^{-1}. Therefore, there is more hardening due to twinning under such deformation conditions. In particular, the higher hardening rates under high strain-rate deformation arise from the reduction of the slip length of mobile dislocations due to more activity of CTW/DTW.

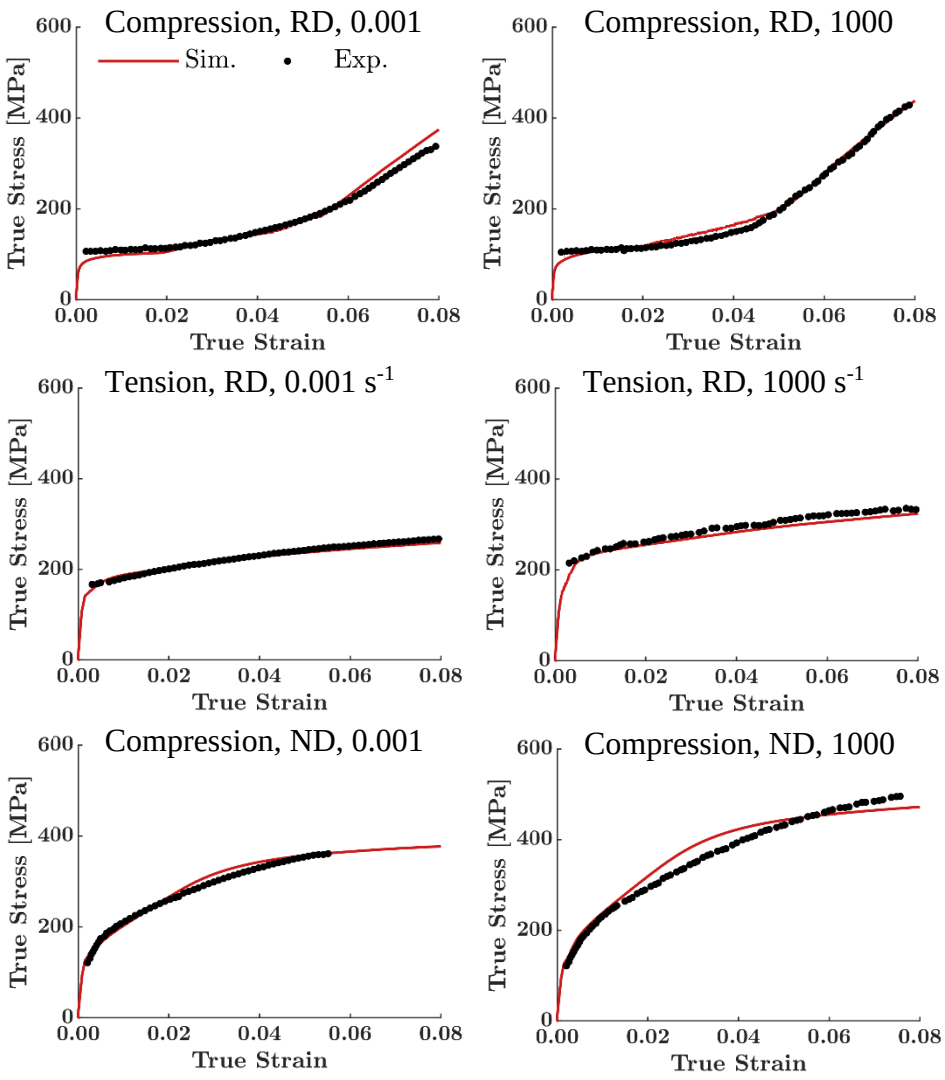

Figure 5. Comparison of measured and simulated true stress–true strain responses of the alloy in compression and tension along the rolling direction (RD) and in compression along the normal direction (ND) at room temperature under two strain-rates. The simulations are based on the measured values of strain-rate sensitivity per deformation mode.

Table 1a. Fitting parameters for the evolution of slip resistance per slip mode.

Parameter	Basal, $\alpha = 1$	Prismatic, $\alpha = 2$	Pyramidal, $\alpha = 3$
τ_0^α [MPa]	1.9	58	72
k_1^α [m^{-1}]	6E+6	1.8E+6	1.8E+8
g^α	1.4E-4	1.2E-4	6.2E-3
D^α [MPa]	100	150	225
q^α	130	250	720
H_1^α	0.007	0.014	0.13
H_2^α	0.1	0.20	3.53
H_3^α	0.13	0.20	2.12

Table 1b. Fitting parameters for the evolution of twin resistance per twin mode.

Parameter	Extension, $\beta = 1$	Contraction, $\beta = 2$
τ_{crit}^β [MPa]	15	90
τ_{prop}^β [MPa]	7	20
H_0^β [MPa]$\sqrt{\mathrm{m}}$	0.09	0.13
$C^{\alpha\beta}, \alpha = 1$	600	200
$C^{\alpha\beta}, \alpha = 2$	600	300
$C^{\alpha\beta}, \alpha = 3$	600	600

Table 2a. Measured values of strain-rate sensitivity per slip mode, m^α, achieved in the model by a combination of n^α and k^α.

Parameter	Basal, $\alpha = 1$	Prismatic, $\alpha = 2$	Pyramidal, $\alpha = 3$
n^α	20	20	20
k^α	49999	1.28	5.74
$n^\alpha\ (k^\alpha + 1)$	1000000	42.6	134.8
m^α	0.000001	0.0235	0.00742

Table 2b. Measured values of strain-rate sensitivity per twin mode, m^{β}, achieved in the model by a combination of n^{β} and k^{β}.

Parameter	Extension, $\beta = 1$	Contraction, $\beta = 2$
n^{β}	20	20
k^{β}	49999	49999
$n^{\beta}\ (k^{\beta} + 1)$	1000000	1000000
m^{β}	0.000001	0.000001

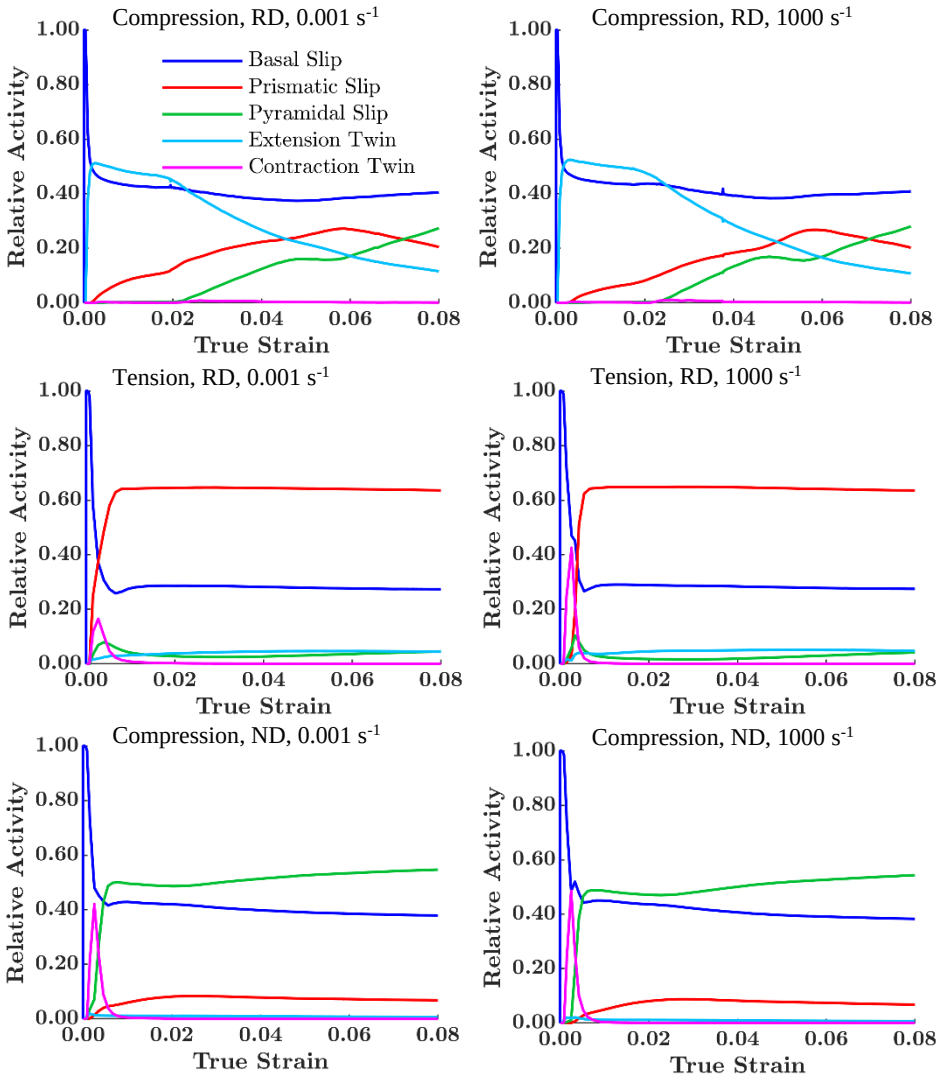

Figure 6. Predicted activities of deformation mechanisms accommodating plastic deformation of the alloy in the deformation conditions indicated in the figure. The plots include activities in both the parent grains and the twinned domains.

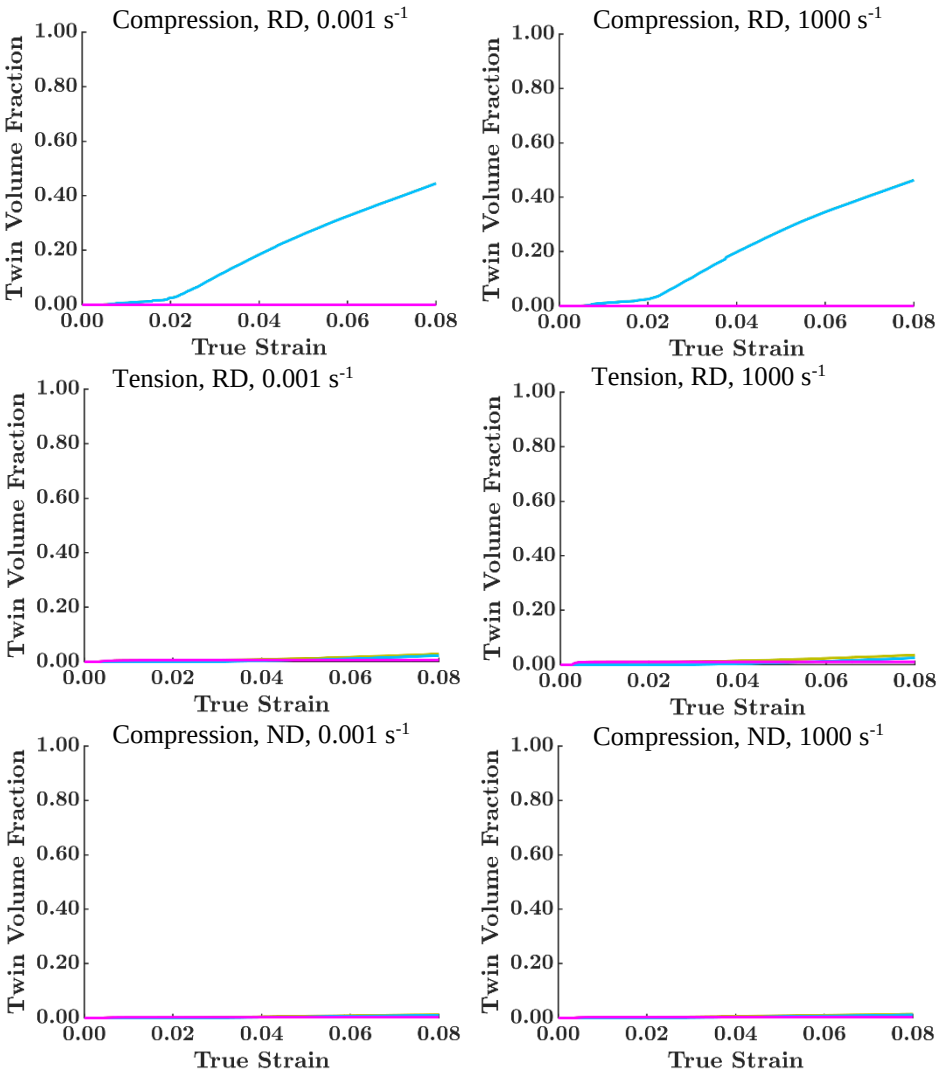

Figure 7. Predicted twin volume fraction evolution during the deformation conditions indicated in the figure.

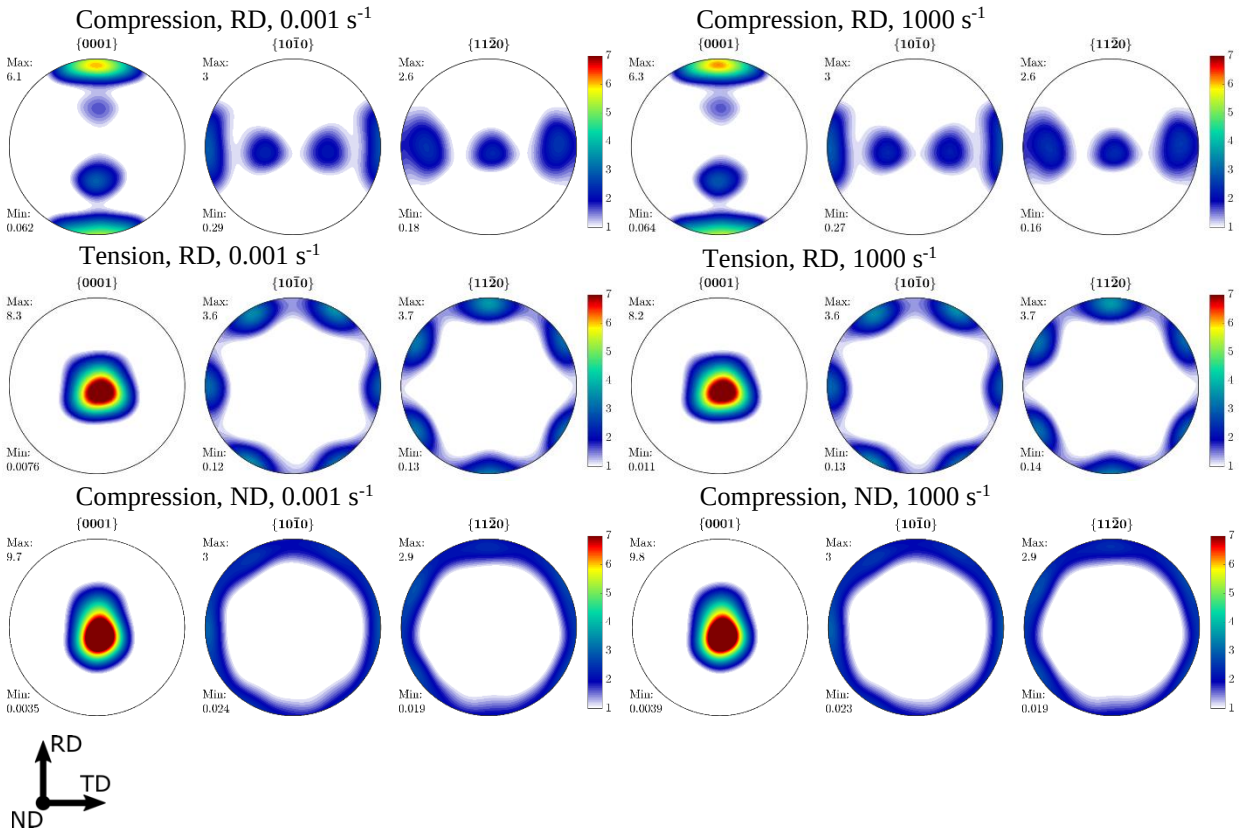

Figure 8. Pole figures showing predicted texture in the alloy after deformation under the conditions indicated in the figure to a strain of 0.08.

Fig. 9 shows predicted true stress versus strain-rate trend lines at two strain levels (0.02 and 0.08) superimposed over the trend lines from Fig. 3b. The model successfully predicts the trend that TD is the strongest and RD is the weakest direction. Moreover, the model predicts that the in-plane compressive response is strain-rate insensitive (the low slope) at the lower strain level (0.02) for all three tested direction, since basal slip and extension twinning-dominated the plasticity. The model also predicts that the compressive strain-rate sensitivity increases at the higher strain level (0.08) due to the activation of pyramidal and prismatic slip systems. The model predicts the increase in strength with the strain-rate in all the three tested directions in tension. Such behavior is attributed to the strain-rate dependency of deformation mechanisms

other than extension twinning and basal slip. Interestingly, the trend lines for tension along the three direction show similar slope at both strain levels. This is because there is no shift in deformation mechanisms during tensile deformation. Finally, it is not surprising that the model successfully predicts the increase in the degree of tension/compression asymmetry with increase in the strain-rate. These good predictions result from proper modeling of deformation mechanisms strain-rate sensitivity and the strain-rate sensitive evolution of slip/twin resistances.

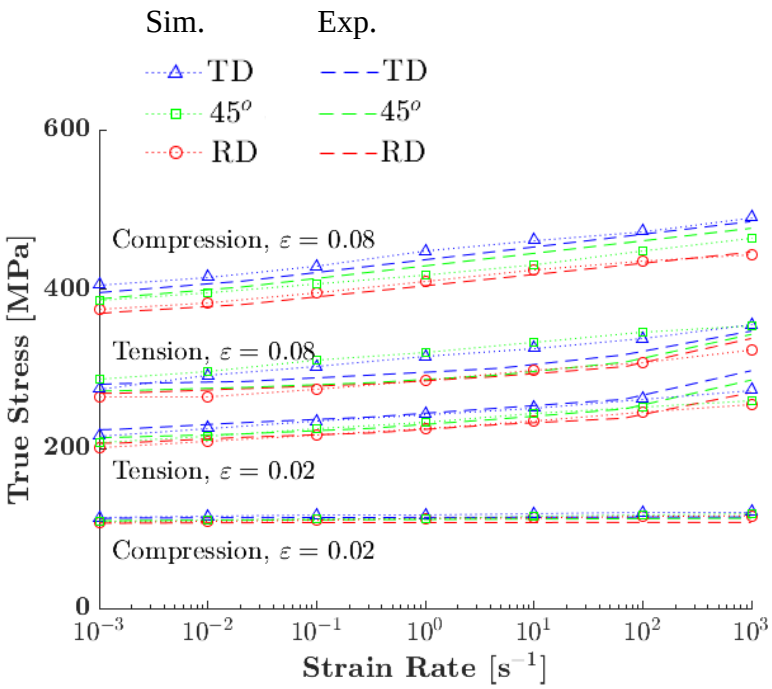

Figure 9. Predicted true stress versus strain-rate trend lines at two strain levels (0.02 and 0.08) superimposed over the trend lines from Fig. 3b for the sheet deformed in simple compression and tension along the three in-plane direction (RD, 45°, and TD). The symbols are predicted points.

5. Discussions

Strain-rate sensitivity is an essential material property governing the strain-rate dependent flow stress response and formability as a function of imposed strain-rate. Understanding and predicting such material behavior is of significant interest e.g. to support designs for crash or

impact. Mg alloys exhibit complex strain-rate sensitive behavior owing to underlying deformation mechanisms. This paper is a contribution towards predicting the true visco-plastic properties of polycrystalline alloy AZ31 using T-CPFE, a multi-level constitutive model linking the grain-level to polycrystalline aggregate-level to FE macro-level material response.

The numerical method incorporated at the deformation mechanism-level facilitates the use of strain-rate sensitivity exponents corresponding to any value of strain-rate sensitivity. As a result, the true values of strain-rate sensitivity of deformation mechanisms were utilized in the T-CPFE simulations of AZ31. The use of accurate values of the constant structure strain-rate sensitivities allowed for accurate characterization of the strain-rate sensitive evolution of slip resistances, τ_c^s, which are governed by the thermally activated hardening law.

To demonstrate the utility of the developed T-CPFE model, a comprehensive dataset of alloy AZ31 collected over a wide range of strain-rates from 10^{-3} s^{-1} to 10^{3} s^{-1} is used. Over this range, a comparison between measured and predicted flow stress corresponding to a fixed microstructural states at 0.02 and 0.08 strains under tension and compression is performed. The plots consisted of comparing macroscopic stress versus strain-rate. In terms of the model, this could be thought of holding distributions of slip/twin resistances corresponding to the two microstructural states constant, while applying strain-rates. As shown, the model achieves good agreement because the appropriate values of the power-law exponents per slip/twin mode were used.

Slip/twin resistances evolve with straining and are dependent on strain-rate. The hardening law for slip and twinning is calibrated using the flow stress and structure evolution data. The in-plane (RD) flow stress in compression is accurately predicted as approximately strain-rate insensitive for the early portion of deformation as a result of the deformation dominated by basal slip and extension twinning. These predictions verify measurements that these two deformation

mechanisms are strain-rate insensitive. As twins reorient texture in the material, pyramidal and prismatic slip mechanisms increasingly activate. As a result of strain-rate sensitivity of these slip mechanisms, the overall material exhibits increasingly strain-rate sensitive response. Under loading in tension, the alloy exhibits strong strain-rate sensitivity. Such behavior is a consequence of tensile deformation being accommodated primarily by slip and, in particular, prismatic slip. The increase in tension/compression asymmetry with strain-rate is also predicted well since it is a consequence of accurate modeling of strain-rate sensitivities intrinsic to the deformation mechanisms accommodating tension vs compression. The strain-rate sensitivity of the ND compression results primarily from pyramidal slip. As the compressive response in RD and ND are successfully predicted at strain-rates of 10^{-3} s^{-1} and 10^{3} s^{-1}, the model also captures the evolution of anisotropy with strain-rate. More importantly, the increase in the rate of strain hardening with strain-rate is accurately predicted to be governed primarily by the evolution of slip/twin resistance. Note that the response in ND compression under 10^{3} s^{-1} strain-rate is stronger than under 10^{-3} s^{-1} not only because of strain-rate sensitivity of pyramidal slip system but also because of the rapid rate of hardening. Contraction twins induce this hardening, which is modeled using the barrier effect. The thin contraction twins are known to cause such hardening since they cut the path of the pyramidal dislocations (Knezevic et al., 2010).

In closing, we show that the model can be used to infer strain-rate sensitivity per deformation mode by accurate fitting of the experimental data. The fits are slightly improved by refining the strain-rate sensitivities associated with the slip modes and, in particular, by making the pyramidal slip a bit more strain-rate sensitive than in measurements.

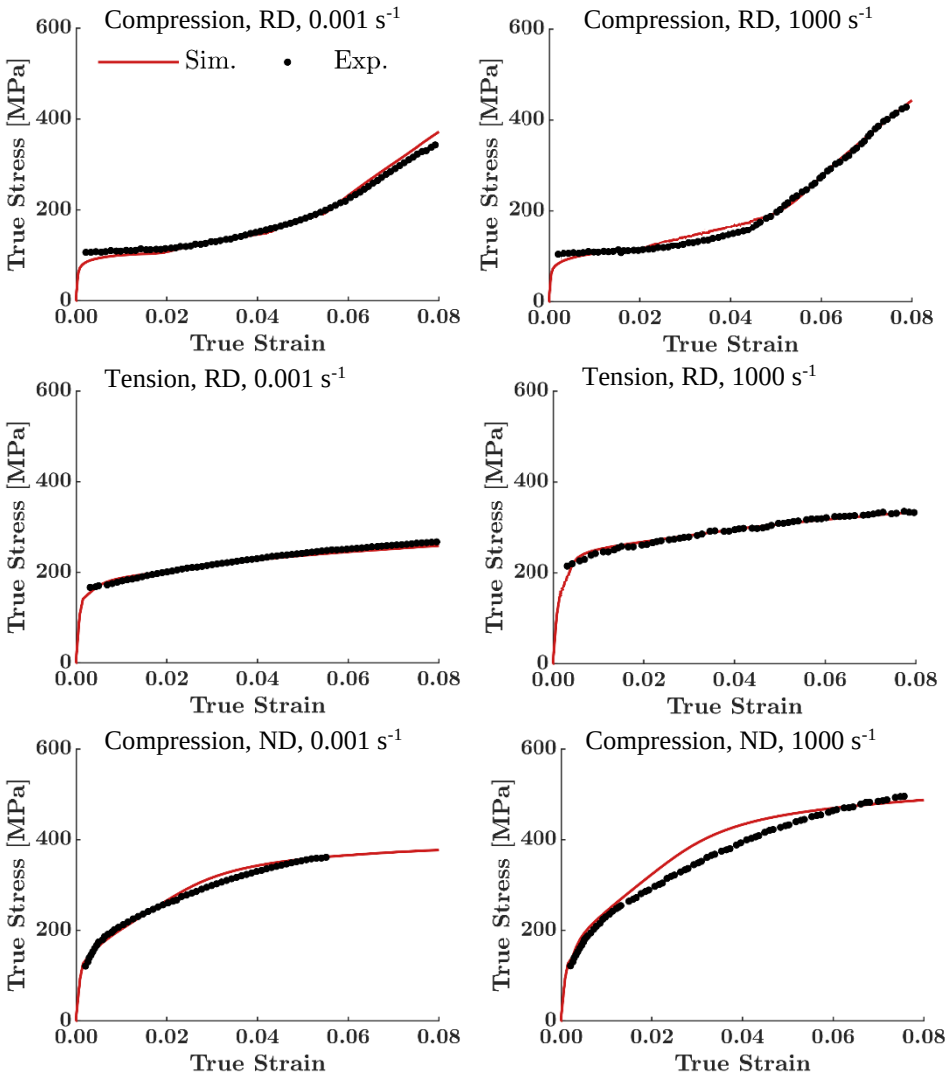

Figure 10. Comparison of measured and simulated true stress–true strain responses for the alloy corresponding to Fig. 5 with simulations performed using adjusted values of strain-rate sensitivity per deformation mode.

Table 3. Adjusted values of strain-rate sensitivity per slip mode, m^{α}.

Parameter	Basal, $\alpha = 1$	Prismatic, $\alpha = 2$	Pyramidal, $\alpha = 3$
n^{α}	20	20	20
k^{α}	49999	1	3
$n^{\alpha}\ (k^{\alpha} + 1)$	1000000	40	80
m^{α}	0.000001	0.025	0.0125

6. Conclusions

A numerical method enabling the use of true strain-rate sensitivity exponents for polycrystalline materials is implemented within a CPFE model. Importantly, the method does not increase computation time involved in simulations. The method facilitates separation of a strain-rate sensitivity embedded in the evolution of slip/twin resistances due to microstructural evolution and the constant structure strain-rate sensitivity driven by the exponent. The development presented in this paper marks the first time T-CPFE model implementation able to represent thermally activated dislocation glide per slip mode and twinning in a quantitative agreement with a wide range of strain-rate experimental conditions, without superfluous strain-rate effects entering numerically via the power-law exponent. The enhanced CPFE model is multi-level in nature, in which the grain-level to polycrystalline aggregate-level to FE macro-level modeling components, operate concurrently. In the model, resistances to slip/twin evolve as a function of strain-rate using a dislocation density-based hardening law. To demonstrate the utility of the enhanced CPFE, simulations are performed for alloy AZ31, which exhibits a variable strain-rate sensitivity of deformation mechanisms from relatively low, $m = 10^{-6}$ or equivalently the high exponent value of 10^6, to relatively high, $m = 0.025$ or equivalently the exponent value of 40. These simulations are the crystal visco-plasticity modeling of alloy AZ31 with the measured values of deformation mechanism strain-rate sensitivities governing the macro-level flow stress response to facilitate the quantitative verification over a wide range of experimental conditions. The model accurately predicts flow stress and evolution of texture and twinning for a broad range of strain-rates ranging from 10^{-3} s^{-1} to 10^3 s^{-1} and loading orientations in tension and compression as a result of not only differing relative amounts of slip and twinning activity driven by a single set of accurately characterized hardening law parameters but also deformation

mechanism-level strain-rate sensitivities. Calculations show that the model successfully captures the phenomena pertaining to the effect of increase in the strain-rate on the mechanical response including: (i) initially strain-rate independent followed by increasingly strain-rate dependent response with plastic strain for the in-plane compression, (ii) increasing rate of strain hardening with strain-rate for the through-thickness compression, (iii) constant strain-rate sensitivity under in-plane tension, and (iv) increasing tension/compression asymmetry with strain-rate. As the T-CPFE model successfully reproduces the mechanical data, it also validates the measured strain-rate dependency of deformation mechanisms. Hence, the model can also be used to verify or infer strain-rate sensitivity per deformation mechanism by reproducing experimental data.

Acknowledgements

This research was sponsored by the U.S. National Science Foundation and was accomplished under the CAREER grant no. CMMI-1650641. D.J.S. gratefully acknowledges discussions with Miroslav Zecevic about introducing the k-mod method into the T-CPFE framework and the Seaborg Institute for partial financial support under a post-doctoral fellowship through the Los Alamos National Laboratory LDRD program.

Appendix A

This appendix summarizes equations pertaining to a strain-rate and temperature sensitive hardening law used in the present work for the evolution of resistances to slip/twin. The law is from (Ardeljan et al., 2016). Only the strain-rate effects are varied here and the temperature T is taken to be 295 K. The law evolves resistance to slip using

$$\tau_{\mathrm{c}}^{\mathrm{s}}(\dot{\varepsilon},T)=\tau_0^{\alpha}+\tau_{\mathrm{HP}}^{\mathrm{s}}+\tau_{\mathrm{for}}^{\mathrm{s}}(\dot{\varepsilon},T)+\tau_{\mathrm{sub}}^{\alpha}(\dot{\varepsilon},T), \tag{A1}$$

where τ_0^{α} is the friction stress per slip mode α, τ_{HP}^{s} is the barrier (Hall-Petch (HP)-like) term evolving per slip system s due to twin lamellae since the grain size barrier effects is already embedded in τ_0^{α}, τ_{for}^{s} is a contribution to the evolution of slip resistance due to buildup of the forest dislocation density, and τ_{sub}^{α} is another evolving term due to the substructure/debris dislocation density.

The barrier term is

$$\tau_{HP}^{s}=\mu^{\alpha}H_i^{\alpha}\sqrt{\frac{b^{\alpha}}{d_{mfp}^{s}}}, \tag{A2}$$

where b^{α} is magnitude of the Burgers vector per mode α ($3.21\text{x}10^{-10}$ m for basal, $3.21\text{x}10^{-10}$ m for prismatic, and $6.12\text{x}10^{-10}$ m for pyramidal), μ^{α} is the shear modulus (16,000 MPa for AZ31 (Watanabe et al., 2004)), H_i^{α} are the fitting HP parameters per slip mode for systems in grains having lamellae of either TTW (i=1), or CTW (i=2), or DTW (i=3), and d_{mfp}^{s} is the mean-free-path for dislocations. The path is estimates as a distance between adjacent twin lamellae per grain using (Proust et al., 2007)

$$d_{mfp}^{s}=\frac{(1-f^{pts})d_c}{\sin(\theta)}, \tag{A3}$$

where f^{pts} is the predominant twinning system (PTS) volume fraction, θ is the angle spanning between the given slip system and twin system planes, and d_c is the spacing estimated as the ratio between the average grain size, $d_g = 12\ \mu m$ for the studied AZ31, and the observed number of lamellae per grain (taken as 3). The model allows formation of multiple twin variants per grain, however, the PTS variant is used to estimate d_{mfp}^{s}.

The terms governed by the evolution of dislocation density populations, $\rho_{for}^{s}(\dot{\varepsilon}, T)$ and $\rho_{sub}(\dot{\varepsilon}, T)$, are (Madec et al., 2002)

$$\tau_{for}^{s} = b^{\alpha}\mu^{\alpha}\sqrt{\chi^{ss'}\rho_{for}^{s'}},\ \tau_{sub}^{\alpha} = 0.086\mu^{\alpha}b^{\alpha}\sqrt{\rho_{sub}}log\left(\frac{1}{b^{\alpha}\sqrt{\rho_{sub}}}\right), \tag{A4}$$

in which $\chi^{ss'}$ is a matrix of dislocation interactions with the diagonal terms (s=s') set to 0.81 and the off-diagonal terms to zero (Lavrentev, 1980; Mecking and Kocks, 1981).

The first dislocation population evolves using (Essmann and Mughrabi, 1979; Mecking and Kocks, 1981)

$$\frac{\partial\rho_{for}^{s}}{\partial\gamma^{s'}} = \frac{\partial\rho_{gen,for}^{s}}{\partial\gamma^{s'}} - \frac{\partial\rho_{rem,for}^{s}}{\partial\gamma^{s'}} = k_1^{\alpha}\sqrt{\rho_{for}^{s}} - k_2^{s}(\dot{\varepsilon}, T)\rho_{for}^{s}, \quad \Delta\rho_{for}^{s} = \frac{\partial\rho_{for}^{s}}{\partial\gamma^{s'}}|\Delta\gamma^{s}|, \tag{A5}$$

where k_1^{α} is a fitting parameter for dislocation storage and $k_2^{\alpha}(\dot{\varepsilon}, T)$ is a dynamic recovery parameter calculated based on the following law (Beyerlein and Tomé, 2008)

$$\frac{k_1^{\alpha}}{k_2^{s}(\dot{\varepsilon},T)} = \frac{1}{\sqrt{\left(\chi^{s's}\right)^{-1}\left(\frac{\tau_{sat}^{\alpha}}{b^{\alpha}\mu^{\alpha}}\right)^{2}}},\ \tau_{sat}^{\alpha} = \frac{D^{\alpha}(b^{\alpha})^{3}g^{\alpha}\mu^{\alpha}}{\left(D^{\alpha}(b^{\alpha})^{3} - kTln\left(\frac{\dot{\varepsilon}}{\dot{\varepsilon}_0}\right)\right)}. \tag{A6}$$

Here, k, is the Boltzmann's constant, $\dot{\varepsilon}_0$ is a value of the reference value of strain-rate (10^7 s^{-1}), , g^α is the activation enthalpy, and D^α is the drag stress. The second dislocation population increments using

$$\Delta\rho_{sub} = \sum_s q^\alpha b^\alpha \sqrt{\rho_{sub}} \frac{\partial \rho^s_{rem,for}}{\partial \gamma^{s'}} \left|\Delta\gamma^{s'}\right|, \tag{A7}$$

In which q^α is a fitting parameter for the amount of debris forming from the recovered dislocations.

The law evolves the resistance to twin using

$$\tau^t_c(\dot{\varepsilon}, T) = \tau^\beta_0 + \tau^t_{HP} + \tau^\beta_{slip}(\dot{\varepsilon}, T). \tag{A8}$$

The friction term is

$$\tau^\beta_0 = \tau^\beta_{\text{prop}} + \left(\tau^\beta_{crit} - \tau^\beta_{\text{prop}}\right) exp\left(-\sum_s \frac{\rho^s_{for}}{\rho^s_{sat}}\right), \tag{A9}$$

with the nucleation stress τ^β_{crit} and propagation stress τ^β_{prop}. The latter term is weighted by the probability term, $\rho^s_{sat} = \left(\frac{k^\alpha_1}{k^s_2}\right)^2$, which favors τ^β_{prop} over τ^β_{crit} with strain (Beyerlein and Tomé, 2008). The HP barrier term is

$$\tau^t_{HP} = \frac{H^\beta_0}{\sqrt{d^t_{mfp}}}. \tag{A10}$$

Finally, the hardening term due to the slip and twin interactions is

$$\tau^\beta_{slip} = \mu^\beta \sum_s C^{\alpha\beta} b^\beta b^\alpha \rho^s_{for}. \tag{A11}$$

Here, $C^{\beta\alpha}$ is the interaction matrix and magnitudes of the Burgers vectors are 1.38×10^{-10} m for extension and 9.24×10^{-11} m for contraction twin modes. The crystal lattice reorientation associated with twinning is modeled using the composite grain (CG) model from (Proust et al., 2007) with the change that present model considers multiple twin variants as well as double twins per grain. Twin variants nucleate in grains when their fraction f^t reach a critical value, which is taken from a distribution centered at 5% for extension and 1% for contraction and double twins. Twin variants inherit parameters such as dislocation densities and slip/twin resistances from the parent grain upon nucleation. As a result of twin nucleation, the number of grains embedded at that FE integration points increases for the number of created twin variants. Growth/thickening of twins is facilitated by transfer of volume fraction from the parent grain to the variant with the shear strain accommodation.

References

Akhtar, A., 1973. Compression of zirconium single crystals parallel to the c-axis. Journal of Nuclear Materials 47, 79-86.

Akhtar, A., 1975. Prismatic slip in zirconium single crystals at elevated temperatures. MTA 6, 1217-1222.

Akhtar, A., Teghtsoonian, E., 1969. Solid solution strengthening of magnesium single crystals—I alloying behaviour in basal slip. Acta Metall. 17, 1339-1349.

Al-Samman, T., Gottstein, G., 2008. Room temperature formability of a magnesium AZ31 alloy: Examining the role of texture on the deformation mechanisms. Mater. Sci. Eng. A 488, 406-414.

Anand, L., 2004. Single-crystal elasto-viscoplasticity: application to texture evolution in polycrystalline metals at large strains. Computer Methods in Applied Mechanics and Engineering 193, 5359-5383.

Ardeljan, M., Beyerlein, I.J., Knezevic, M., 2014. A dislocation density based crystal plasticity finite element model: Application to a two-phase polycrystalline HCP/BCC composites. J. Mech. Phys. Solids 66, 16-31.

Ardeljan, M., Beyerlein, I.J., McWilliams, B.A., Knezevic, M., 2016. Strain rate and temperature sensitive multi-level crystal plasticity model for large plastic deformation behavior: Application to AZ31 magnesium alloy. Int. J. Plast. 83, 90-109.

Ardeljan, M., Knezevic, M., 2018. Explicit modeling of double twinning in AZ31 using crystal plasticity finite elements for predicting the mechanical fields for twin variant selection and fracture analyses. Acta. Mater. 157, 339-354.

Ardeljan, M., Knezevic, M., Nizolek, T., Beyerlein, I.J., Mara, N.A., Pollock, T.M., 2015a. A study of microstructure-driven strain localizations in two-phase polycrystalline HCP/BCC composites using a multi-scale model. Int. J. Plast. 74, 35-57.

Ardeljan, M., McCabe, R.J., Beyerlein, I.J., Knezevic, M., 2015b. Explicit incorporation of deformation twins into crystal plasticity finite element models. Computer Methods in Applied Mechanics and Engineering 295, 396-413.

Asaro, R.J., Needleman, A., 1985. Texture development and strain hardening in rate dependent polycrystals. Acta Metall. Mater. 33, 923-953.

Asgari, S., El-Danaf, E., Kalidindi, S.R., Doherty, R.D., 1997. Strain hardening regimes and microstructural evolution during large strain compression of low stacking fault energy fcc alloys that form deformation twins. Metall. Mater. Trans. A 28A, 1781-1795.

Barnett, M., 2003. A Taylor model based description of the proof stress of magnesium AZ31 during hot working. Metall. Mater. Trans. A 34, 1799-1806.

Barnett, M.R., 2007a. Twinning and the ductility of magnesium alloys: Part I: "Tension" twins. Mater. Sci. Eng. A 464, 1-7.

Barnett, M.R., 2007b. Twinning and the ductility of magnesium alloys: Part II. "Contraction" twins. Mater. Sci. Eng. A 464, 8-16.

Barnett, M.R., Keshavarz, Z., Beer, A.G., Atwell, D., 2004. Influence of grain size on the compressive deformation of wrought Mg–3Al–1Zn. Acta. Mater. 52, 5093-5103.

Basinski, Z.S., Szczerba, M.S., Niewczas, M., Embury, J.D., Basinski, S.J., 1997. Transformation of slip dislocations during twinning of copper-aluminum alloy crystals. Revue de Metallurgie. Cahiers D'Informations Techniques 94, 1037-1044.

Bathe, K.-J., 1996. Finite element procedures. Englewood Cliffs, N.J.: Prentice Hall.

Beyerlein, I.J., Tomé, C.N., 2008. A dislocation-based constitutive law for pure Zr including temperature effects. Int. J. Plast. 24, 867-895.

Bouvier, S., Benmhenni, N., Tirry, W., Gregory, F., Nixon, M.E., Cazacu, O., Rabet, L., 2012. Hardening in relation with microstructure evolution of high purity α–titanium deformed under monotonic and cyclic simple shear loadings at room temperature. Mater. Sci. Eng. A 535, 12-21.

Chapuis, A., Liu, Q., 2019. Modeling strain rate sensitivity and high temperature deformation of Mg-3Al-1Zn alloy. Journal of Magnesium and Alloys 7, 433-443.

Chen, S., Gray, G., 1996. Constitutive behavior of tantalum and tantalum-tungsten alloys. Metall. Mater. Trans. A 27, 2994-3006.

Chun, Y.B., Davies, C.H.J., 2011. Twinning-induced negative strain rate sensitivity in wrought Mg alloy AZ31. Mater. Sci. Eng. A 528, 5713-5722.

Clausen, B., Tomé, C.N., Brown, D.W., Agnew, S.R., 2008. Reorientation and stress relaxation due to twinning: Modeling and experimental characterization for Mg. Acta. Mater. 56, 2456-2468.

Delannay, L., Kalidindi, S.R., Van Houtte, P., 2003. Quantitative prediction of textures in aluminium cold rolled to moderate strains (vol 336, pg 233, 2002). Materials Science and Engineering a-Structural Materials Properties Microstructure and Processing 351, 358-359.

Diard, O., Leclercq, S., Rousselier, G., Cailletaud, G., 2005. Evaluation of finite element based analysis of 3D multicrystalline aggregates plasticity: Application to crystal plasticity model identification and the study of stress and strain fields near grain boundaries. Int. J. Plast. 21, 691-722.

El Kadiri, H., Oppedal, A.L., 2010. A crystal plasticity theory for latent hardening by glide twinning through dislocation transmutation and twin accommodation effects. J. Mech. Phys. Solids 58, 613-624.

Essmann, U., Mughrabi, H., 1979. Annihilation of dislocations during tensile and cyclic deformation and limits of dislocation densities. Philosophical Magazine A 40, 731-756.

Fast, T., Knezevic, M., Kalidindi, S.R., 2008. Application of microstructure sensitive design to structural components produced from hexagonal polycrystalline metals. Comput. Mater. Sci. 43, 374-383.

Feather, W.G., Ghorbanpour, S., Savage, D.J., Ardeljan, M., Jahedi, M., McWilliams, B.A., Gupta, N., Xiang, C., Vogel, S.C., Knezevic, M., 2019. Mechanical response, twinning, and texture evolution of WE43 magnesium-rare earth alloy as a function of strain rate: Experiments and multi-level crystal plasticity modeling. Int. J. Plast. 120, 180-204.

Fernández, A., Jérusalem, A., Gutiérrez-Urrutia, I., Pérez-Prado, M.T., 2013. Three-dimensional investigation of grain boundary–twin interactions in a Mg AZ31 alloy by electron backscatter diffraction and continuum modeling. Acta. Mater. 61, 7679-7692.

Follansbee, P., 1986. High-strain-rate deformation of FCC metals and alloys, Metallurgical applications of shock-wave and high-strain-rate phenomena. Marcel Dekker, INC., New York, pp. 451-479.

Follansbee, P., Kocks, U., 1988. A constitutive description of the deformation of copper based on the use of the mechanical threshold stress as an internal state variable. Acta Metall. 36, 81-93.

Hosford, W.F., 2010. Mechanical behavior of materials. Cambridge University Press, New York, NY, USA.

Hutchinson, J.W., 1976. Bounds and self-consistent estimates for creep of polycrystalline materials. Proceedings of the Royal Society of London. Series A, Mathematical and Physical Sciences 348, 101-126.

Ishikawa, K., Watanabe, H., Mukai, T., 2005. High strain rate deformation behavior of an AZ91 magnesium alloy at elevated temperatures. Materials Letters 59, 1511-1515.

Jahedi, M., Ardeljan, M., Beyerlein, I.J., Paydar, M.H., Knezevic, M., 2015. Enhancement of orientation gradients during simple shear deformation by application of simple compression. J. Appl. Phys. 117, 214309.

Jain, A., Agnew, S.R., 2007. Modeling the temperature dependent effect of twinning on the behavior of Mg alloy AZ31 sheet. Mater. Sci. Eng. A, 29-36.

Kalidindi, S.R., 1998. Incorporation of deformation twinning in crystal plasticity models. J. Mech. Phys. Solids 46, 267-271.

Kalidindi, S.R., Bronkhorst, C.A., Anand, L., 1992. Crystallographic texture evolution in bulk deformation processing of FCC metals. J. Mech. Phys. Solids 40, 537-569.

Kaschner, G.C., Tomé, C.N., McCabe, R.J., Misra, A., Vogel, S.C., Brown, D.W., 2007. Exploring the dislocation/twin interactions in zirconium. Mater. Sci. Eng. A 463, 122-127.

Khan, A.S., Pandey, A., Gnäupel-Herold, T., Mishra, R.K., 2011. Mechanical response and texture evolution of AZ31 alloy at large strains for different strain rates and temperatures. Int. J. Plast. 27, 688-706.

Knezevic, M., Beyerlein, I.J., 2018. Multiscale Modeling of Microstructure-Property Relationships of Polycrystalline Metals during Thermo-Mechanical Deformation. Advanced Engineering Materials 20, 1700956.

Knezevic, M., Beyerlein, I.J., Brown, D.W., Sisneros, T.A., Tomé, C.N., 2013a. A polycrystal plasticity model for predicting mechanical response and texture evolution during strain-path changes: Application to beryllium. Int. J. Plast. 49, 185-198.

Knezevic, M., Capolungo, L., Tomé, C.N., Lebensohn, R.A., Alexander, D.J., Mihaila, B., McCabe, R.J., 2012. Anisotropic stress-strain response and microstructure evolution of textured α-uranium. Acta. Mater. 60, 702-715.

Knezevic, M., Daymond, M.R., Beyerlein, I.J., 2015. Modeling discrete twin lamellae in a microstructural framework. Scripta Materialia (under review).

Knezevic, M., Lebensohn, R.A., Cazacu, O., Revil-Baudard, B., Proust, G., Vogel, S.C., Nixon, M.E., 2013b. Modeling bending of α-titanium with embedded polycrystal plasticity in implicit finite elements. Mater. Sci. Eng. A 564, 116-126.

Knezevic, M., Levinson, A., Harris, R., Mishra, R.K., Doherty, R.D., Kalidindi, S.R., 2010. Deformation twinning in AZ31: Influence on strain hardening and texture evolution. Acta. Mater. 58, 6230-6242.

Knezevic, M., McCabe, R.J., Lebensohn, R.A., Tomé, C.N., Liu, C., Lovato, M.L., Mihaila, B., 2013c. Integration of self-consistent polycrystal plasticity with dislocation density based hardening laws within an implicit finite element framework: Application to low-symmetry metals. J. Mech. Phys. Solids 61, 2034-2046.

Knezevic, M., McCabe, R.J., Tomé, C.N., Lebensohn, R.A., Chen, S.R., Cady, C.M., Gray Iii, G.T., Mihaila, B., 2013d. Modeling mechanical response and texture evolution of α-uranium as a function of strain rate and temperature using polycrystal plasticity. Int. J. Plast. 43, 70-84.

Knezevic, M., Zecevic, M., Beyerlein, I.J., Lebensohn, R.A., 2016. A numerical procedure enabling accurate descriptions of strain rate-sensitive flow of polycrystals within crystal visco-plasticity theory. Computer Methods in Applied Mechanics and Engineering 308, 468-482.

Kocks, U., Argon, A., Ashby, M., 1975. Thermodynamics and Kinetics of Slip. Prog. Mater. Sci. 19, 110-170.

Kocks, U.F., Tomé, C.N., Wenk, H.-R., 1998. Texture and Anisotropy. Cambridge University Press, Cambridge, UK.

Kok, S., Beaudoin, A.J., Tortorelli, D.A., 2002. A polycrystal plasticity model based on the mechanical threshold. Int. J. Plast. 18, 715-741.

Korla, R., Chokshi, A.H., 2010. Strain-rate sensitivity and microstructural evolution in a Mg–Al–Zn alloy. Scr. Mater. 63, 913-916.

Kumar, A.M., Kanjarla, A.K., Niezgoda, S.R., Lebensohn, R.A., Tomé, C.N., 2015. Numerical study of the stress state of a deformation twin in magnesium. Acta. Mater. 84, 349-358.

Kurukuri, S., Worswick, M.J., Ghaffari Tari, D., Mishra, R.K., Carter, J.T., 2014. Rate sensitivity and tension–compression asymmetry in AZ31B magnesium alloy sheet. Philosophical Transactions of the Royal Society A: Mathematical, Physical and Engineering Sciences 372, 20130216.

Lavrentev, F.F., 1980. The type of dislocation interaction as the factor determining work hardening. Materials Science and Engineering 46, 191-208.

Lebensohn, R.A., Kanjarla, A.K., Eisenlohr, P., 2012. An elasto-viscoplastic formulation based on fast Fourier transforms for the prediction of micromechanical fields in polycrystalline materials. Int. J. Plast. 32-33, 59-69.

Lebensohn, R.A., Tomé, C.N., 1993. A self-consistent anisotropic approach for the simulation of plastic deformation and texture development of polycrystals: Application to zirconium alloys. Acta Metall. Mater. 41, 2611-2624.

Lentz, M., Klaus, M., Beyerlein, I.J., Zecevic, M., Reimers, W., Knezevic, M., 2015. In situ X-ray diffraction and crystal plasticity modeling of the deformation behavior of extruded Mg–Li–(Al) alloys: An uncommon tension–compression asymmetry. Acta. Mater. 86, 254-268.

Lou, X.Y., Li, M., Boger, R.K., Agnew, S.R., Wagoner, R.H., 2007. Hardening evolution of AZ31B Mg sheet. Int. J. Plast. 23, 44-86.

Madec, R., Devincre, B., Kubin, L.P., 2002. From Dislocation Junctions to Forest Hardening. Physical Review Letters 89, 255508.

Mecking, H., Kocks, U.F., 1981. Kinetics of flow and strain-hardening. Acta Metall. Mater. 29, 1865-1875.

Molodov, K.D., Al-Samman, T., Molodov, D.A., 2017. Profuse slip transmission across twin boundaries in magnesium. Acta. Mater. 124, 397-409.

Partridge, P.G., 1967. The crystallography and deformation modes of hexagonal close-packed metals. Metallurgia Revised 12, 169.

Poulin, C.M., Korkolis, Y.P., Kinsey, B.L., Knezevic, M., 2019. Over five-times improved elongation-to-fracture of dual-phase 1180 steel by continuous-bending-under-tension. Mater. Des. 161, 95-105.

Proust, G., Tomé, C.N., Jain, A., Agnew, S.R., 2009a. Modeling the effect of twinning and detwinning during strain-path changes of magnesium alloy AZ31. Int. J. Plast. 25, 861-880.

Proust, G., Tomé, C.N., Jain, A., Agnew, S.R., 2009b. Modeling the effect of twinning and detwinning during strain path changes of Mg alloy AZ31. International Journal of Plasticity 25, 861-880.

Proust, G., Tomé, C.N., Kaschner, G.C., 2007. Modeling texture, twinning and hardening evolution during deformation of hexagonal materials. Acta. Mater. 55, 2137-2148.

Risse, M., Lentz, M., Fahrenson, C., Reimers, W., Knezevic, M., Beyerlein, I.J., 2017. Elevated Temperature Effects on the Plastic Anisotropy of an Extruded Mg-4 Wt Pct Li Alloy: Experiments and Polycrystal Modeling. Metall. Mater. Trans. A 48, 446-458.

Savage, D.J., Cazacu, O., Knezevic, M., 2017. Dilational Response of Voided Polycrystals. JOM 69, 942-947.

Segurado, J., Lebensohn, R.A., Llorca, J., Tomé, C.N., 2012. Multiscale modeling of plasticity based on embedding the viscoplastic self-consistent formulation in implicit finite elements. Int. J. Plast. 28, 124-140.

Slutsky, L.J., Garland, C.W., 1957. Elastic Constants of Magnesium from 4.2 K to 300 K. Physical Review 107, 972-976.

Staroselsky, A., Anand, L., 2003. A constitutive model for hcp materials deforming by slip and twinning: application to magnesium alloy AZ31B. Int. J. Plast. 19, 1843-1864.

Tomé, C.N., 1999. Self-consistent polycrystal models: A directional compliance criterion to describe grain interactions. Modelling and Simulation in Materials Science and Engineering 7, 723-738.

Tomé, C.N., Lebensohn, R.A., Kocks, U.F., 1991. A model for texture development dominated by deformation twinning: Application to zirconium alloys. Acta Metall. Mater. 39, 2667-2680.

Ulacia, I., Dudamell, N.V., Gálvez, F., Yi, S., Pérez-Prado, M.T., Hurtado, I., 2010. Mechanical behavior and microstructural evolution of a Mg AZ31 sheet at dynamic strain rates. Acta. Mater. 58, 2988-2998.

Van Houtte, P., 1978. Simulation of the rolling and shear texture of brass by the Taylor theory adapted for mechanical twinning. Acta Metall. Mater. 26, 591-604.

Wang, H., Wu, P., Kurukuri, S., Worswick, M.J., Peng, Y., Tang, D., Li, D., 2018. Strain rate sensitivities of deformation mechanisms in magnesium alloys. Int. J. Plast. 107, 207-222.

Watanabe, H., Ishikawa, K., 2009. Effect of texture on high temperature deformation behavior at high strain rates in a Mg–3Al–1Zn alloy. Mater. Sci. Eng. A 523, 304-311.

Watanabe, H., Mukai, T., Sugioka, M., Ishikawa, K., 2004. Elastic and damping properties from room temperature to 673 K in an AZ31 magnesium alloy. Scr. Mater. 51, 291-295.

Wu, X., Kalidindi, S.R., Necker, C., Salem, A.A., 2007a. Prediction of crystallographic texture evolution and anisotropic stress-strain curves during large plastic strains in high purity α-titanium using a Taylor-type crystal plasticity model. Acta. Mater. 55, 423-432.

Wu, X., Proust, G., Knezevic, M., Kalidindi, S.R., 2007b. Elastic-plastic property closures for hexagonal close-packed polycrystalline metals using first-order bounding theories. Acta. Mater. 55, 2729-2737.

Yoo, M.H., 1981. Slip, twinning, and fracture in hexagonal close-packed metals. Metall. Mater. Trans. A 12, 409–418.

Yuan, W., Panigrahi, S.K., Su, J.Q., Mishra, R.S., 2011. Influence of grain size and texture on Hall–Petch relationship for a magnesium alloy. Scr. Mater. 65, 994-997.

Zecevic, M., Beyerlein, I.J., Knezevic, M., 2017. Coupling elasto-plastic self-consistent crystal plasticity and implicit finite elements: Applications to compression, cyclic tension-compression, and bending to large strains. Int. J. Plast. 93, 187-211.

Zecevic, M., Beyerlein, I.J., McCabe, R.J., McWilliams, B.A., Knezevic, M., Transitioning rate sensitivities across multiple length scales: Microstructure-property relationships in the Taylor

cylinder impact test on zirconium. International Journal of Plasticity, doi:10.1016/j.ijplas.2016.05.005.

Zecevic, M., Beyerlein, I.J., McCabe, R.J., McWilliams, B.A., Knezevic, M., 2016. Transitioning rate sensitivities across multiple length scales: Microstructure-property relationships in the Taylor cylinder impact test on zirconium. Int. J. Plast. 84, 138-159.

Zecevic, M., McCabe, R.J., Knezevic, M., 2015. Spectral database solutions to elasto-viscoplasticity within finite elements: Application to a cobalt-based FCC superalloy. Int. J. Plast. 70, 151-165.

Conclusions and Future Work

This work presented the use of a Taylor Type Crystal Plasticity Model (CPFE) for investigating the mechanical behavior and microstructural evolution of hexagonal metals under quasi-static and high strain rate deformation. In this work it was found that the dramatic hardening of the magnesium alloy, WE43 under high rate deformation was due to the activation of compression twins and double twinning. This behavior and the corresponding microstructural evolution was found to be accurately predicted by the CPFE code developed under this work. Work under this thesis also found that explicit grain simulations using crystal plasticity models benefit from the use of quadratic tetrahedral elements or linear hexahedral elements. In a study comparing the accuracy of these elements along with linear tetrahedral and quadratic hexahedral elements found those to be most accurate, with the quadratic Tet being best suited due to the ease at which it can be used to mesh these complex geometries. The final work reported in this thesis presents a numerical method to allows realistic rate sensitivity power-law exponents to be used while still being computationally efficient. The method developed is referred to as the k-Mod method, which scales the stress in the power-law equation to enable it to be computationally feasible to use large exponents. This improvement was demonstrated by accurately predicting the response of rolled AZ31 Mg using measured rate sensitivity exponents. While making this addition to the CPFE code, general improvements were made to modernize the code, improve the user inputs and make the code thread safe. Most important of these is the thread safe addition, this enable the use of threaded parallelization, which due to its fundamental difference in variable storage leads to up to a 90% reduction in memory use with little to no performance impact. This dramatic memory improvement will facilitate the use of much larger CPFE simulations.

The work presented here will be continued and improved upon through future work. The effects of voids and damage are currently under investigation by Iftekhar Riyad, Nemanja Kljestan, and Daniel Savage. This study uses cells of voided microstructures with variable fractions and distributions of voids to investigate the effects on yielding of AZ31 and WE43 Mg alloys and pure Ti. A full-field dilatational visco-plastic Fast Fourier Transform (VPFFT) model and the latest CPFE model are used to generate gauge surfaces for comparison.

Another study expanding on the work presented is in the process by Shubhrodev Bhowmik, where confined layer slip (CLS) has been embedded into the dislocation density hardening law used by CPFE. This CLS addition is being used to investigate the mechanical behavior of explicitly modeled Al-TiN and Cu-TiN nano-composites.

A final study that is underway is an expansion of the element study presented. Jacob Weiss is undertaking this investigation and will be looking into reduced integration and hybrid formulation elements and their accuracy when used with CPFE for explicit grain simulations.